Thermal cutting of steel plates – modelling, simulation and optimal control of preheating strategies

vorgelegt von
M. Sc.
Manuel Jesús Arenas Jaén
ORCID: 0000-0002-1372-1881

an der Fakultät II - Mathematik und Naturwissenschaften
der Technischen Universität Berlin
zur Erlangung des akademischen Grades

Doktor der Naturwissenschaften
Dr. rer. nat.

genehmigte Dissertation

Promotionsausschuss:

Vorsitzender:	Prof. Dr. Thorsten Koch
Gutachter:	Prof. Dr. Dietmar Hömberg
Gutachterin:	Prof. Dr. María Dolores Gómez Pedreira
Gutachter:	Prof. Dr. Alfred Schmidt

Tag der wissenschaftlichen Aussprache: 26.02.2021

Berlin 2021

Abstract

Steel is commonly delivered as coils, sheets or plates at the final stages of production. The plates have to be cut to the right dimensions and this is usually done by means of thermal cutting. Flame cutting is a common and versatile method to produce steel plates but it can cause undesired side effects.

Till date, the flame cutting process has not been thoroughly studied using mathematical modelling and numerical simulations. The present work describes a 3D quasi-stationary state (QSS) model to understand the distribution of the heat in a steel plate including solid-solid and solid-liquid transitions during the flame cutting process. Simulations are carried out employing the finite element method. They are able to predict the size of the kerf and the heat affected zone.

Recent experimental research has proved that slower speed and adding a preheating stage helps reducing the side effects of flame cutting. The current practice of preheating consists in globally preheating the plates uniformly.

We study an alternative preheating method wherein, local induction is applied just before flame cutting. The method involves using an induction coil on top of the cutting line to preheat the area of the plate to be affected by the flame. In induction, heating is done by electromagnetic fields. Due to the ferromagnetic nature of steel, induced eddy currents are generated directly in the workpiece which then cause heating by the Joule effect.

We use a 3D eddy currents model in the harmonic regime coupled with the QSS heat equation. The simulations showcase that the heating is concentrated in the surface due to the *skin effect*. This heat is transported by conduction to the bottom and some time after the position of the coil, uniform temperature is achieved in the cutting line. The setting described has been replicated in a laboratory for experimental validation and the measurements show similar trends to the numerical simulation results.

The induction preheating concept is influenced by many parameters which makes finding the optimal setting an unfeasible task. To overcome this, the flame cutting system was decoupled from the electromagnetic problem. The electromagnetic joule heat source was substituted by a parametric heat source and was optimised by an optimal control approach. Analysis of this system has been done to prove the existence, uniqueness and regularity of the solutions of the partial differential equation system. A difficulty of the system is that it includes a quasilinear elliptic heat equation coupled to QSS phase fraction equations. First order optimality conditions are derived for the nonlinear elliptic system. A steepest descent algorithm is implemented to solve the optimal control problem. The algorithm provides promising results to match the cutting speed and thicknesses that require different levels of preheating. Moreover, the control is forced to have a similar distribution as the dissipated power that can be obtained by induction heating.

The results of the thesis show that the employment of induction preheating in a real industrial process is indeed feasible. This could lead to the integration of this novel method of preheating in the manufacturing chain, influencing positively on the production rate and energy efficiency of the steel plates production.

Zusammenfassung

Stahl wird üblicherweise in der Endphase der Produktion als Spulen, Bleche oder Platten geliefert. Die Platten müssen auf die richtigen Abmessungen zugeschnitten werden, und dies erfolgt normalerweise durch thermisches Schneiden. Das Flammenschneiden ist eine übliche und vielseitige Methode zur Herstellung von Stahlplatten, kann jedoch unerwünschte Nebenwirkungen verursachen.

Bis heute wurde der Flammenschneidprozess mit mathematischen Modellen und numerischen Simulationen nicht gründlich untersucht. Die vorliegende Arbeit beschreibt ein 3D-Modell des quasi-stationären Zustands (QSS), um die Verteilung der Wärme in einer Stahlplatte einschließlich Fest-Fest- und Fest-Flüssig-Übergängen während des Flammenschneidprozesses zu verstehen. Simulationen werden nach der Finite-Elemente-Methode durchgeführt. Sie können die Größe der Schnittfuge und die Wärmeeinflusszone vorhersagen.

Jüngste experimentelle Untersuchungen haben gezeigt, dass eine langsamere Geschwindigkeit und das Hinzufügen einer Vorheizstufe dazu beitragen, die Nebenwirkungen des Flammenschneidens zu verringern. Die derzeitige Praxis des Vorheizens besteht darin, die Platten global gleichmäßig vorzuwärmen. Wir untersuchen ein alternatives Vorheizverfahren, bei dem die lokale Induktion unmittelbar vor dem Flammenschneiden angewendet wird. Das Verfahren beinhaltet die Verwendung einer Induktionsspule über der Schneidlinie, um den Bereich der Platte, der von der Flamme betroffen sein soll, vorzuwärmen. Bei der Induktion erfolgt die Erwärmung durch elektromagnetische Felder. Aufgrund der ferromagnetischen Natur von Stahl werden direkt im Werkstück induzierte Wirbelströme erzeugt, die dann durch den Joule-Effekt eine Erwärmung verursachen.

Wir verwenden ein 3D-Wirbelstrommodell im harmonischen Bereich in Verbindung mit der QSS-Wärmegleichung. Die Simulationen zeigen, dass sich die Erwärmung aufgrund des *Skin-Effekts* in der Oberfläche konzentriert. Diese Wärme wird durch Wärmeleitung nach unten transportiert und einige Zeit nach der Position der Spule wird eine gleichmäßige Temperatur in der Schneidlinie erreicht. Die beschriebene Einstellung wurde zur experimentellen Validierung in einem Labor repliziert und die Messungen zeigen ähnliche Trends wie die numerischen Simulationsergebnisse.

Das Induktionsvorwärmkonzept wird von vielen Parametern beeinflusst, was es unmöglich macht, die optimale Einstellung zu finden. Um dies zu überwinden, wurde das Flammenschneidsystem vom elektromagnetischen Problem entkoppelt. Die elektromagnetische Joule-Wärmequelle wurde durch eine parametrische Wärmequelle ersetzt und durch einen optimalen Steuerungsansatz optimiert. Die Analyse dieses Systems wurde durchgeführt, um die Existenz, Eindeutigkeit und Regelmäßigkeit der Lösungen des partiellen Differentialgleichungssystems zu beweisen. Eine Schwierigkeit des Systems besteht darin, dass es eine quasilineare elliptische Wärmegleichung enthält, die an QSS-Phasenfraktionsgleichungen gekoppelt ist. Optimalitätsbedingungen erster Ordnung werden für das nichtlineare elliptische System abgeleitet. Ein Algorithmus für den steilsten Abstieg wird implementiert, um das Problem der optimalen Steuerung zu lösen. Der Algorithmus liefert vielversprechende Ergebnisse, um die Schnittgeschwindigkeit und -dicken anzupassen, die unterschiedliche Vorheizstufen erfordern. Darüber hinaus ist die Steuerung gezwungen, eine ähnliche Verteilung wie die Verlustleistung zu haben, die durch Induktionserwärmung erhalten werden kann.

Die Ergebnisse der Arbeit zeigen, dass der Einsatz von Induktionsvorwärmung in einem realen industriellen Prozess tatsächlich machbar ist. Dies könnte zur Integration dieser neuartigen Vorheizmethode in die Fertigungskette führen und sich positiv auf die Produktionsrate und Energieeffizienz der Stahlblechproduktion auswirken.

Acknowledgements

This thesis is the result of my work at the Weierstrass Institute of Applied Analysis and Stochastics (WIAS) within the European Industrial Doctorate (EID) called MIMESIS. The full name of MIMESIS is Mathematics and Materials Science for Steel Production and Manufacturing. The project is part of the Marie Skłodowska Curie Actions within the European Union's funding programme for research and innovation Horizon 2020.

My thanks go to the five institutions that made MIMESIS a reality: EFD Induction in Norway; SSAB, Outokumpu, and the University of Oulu, in Finland; and WIAS in Germany.

At personal level I want to thank first Prof. Dr. Dietmar Hömberg for choosing me to be one of the three students under his supervision in MIMESIS. His motivation, trust and wisdom were a light during this whole journey. The end of this journey was joined later on by Prof. Dr. María Dolores Gómez Pedreira and Prof. Dr. Alfred Schmidt. I want to express my gratitude to them for the review of the thesis.

Furthermore, I would like to thank the members of the Research Group 4 "Nonlinear Optimization and Inverse Problems". Specially Dr. Thomas Petzold, Anke Giese, Dr. Robert Lasarzik and Moritz Ebeling-Rump.

Pertti Mikkonnen and Jarmo Tarkka from SSAB as well as for being open to discussion and my questions. I would also like to thank Agne Bogdanoff, and Seppo Ollila for all their help and arrangements during my industrial secondment in SSAB, Raahe, Finland.

During my one-month stay in EFD, Norway, I was fortunate to spend more time with John Inge Asperheim, Dmitry G. Ivanov and Bjørnar Grande outside of the annual MIMESIS meetings. My thanks to them for their warm welcome and their enthusiasm.

I had the privilege of attending a Material Science Course in Oulu University. I want to thank all the professors and organizers, specially Prof. Dr. David Porter.

Special thanks go to my fellow colleagues from MIMESIS: Prerana Das, Luigino Capone, Vahid Javaheri, Satish K. Kolli, Eshwar K. Ramasetti, Najib Alia and Shashank Ramesh Babu. Specially Shashank for the uncountable, interesting and almost endless conversations and many laughs.

Last but not least, my thanks belong to my family. First, to my mother María del Carmen who even not understanding what I am working on since many years back, still trusts me blindly on achieving success. Second, to my wife Sasha who joined my life a few months into the PhD. Since then, no matter the distance, she has filled my days with joy and energy even in the darkest and lonely days in Finland.

Table of Contents

List of Figures

List of Tables

1

Introduction

Steel is one of the most widely used metallic materials in the world. Steel is an alloy of iron and a small volume of carbon and other elements. Its thermodynamic and physical properties can be manipulated by the inclusion of alloying elements and different heat treatment cycles. This leads to relatively inexpensive manufacturing in large quantities and to its use in applications with very precise specifications.

At the final stage of the steel production, it is commonly delivered in coil, sheet or plate shape. The plates have to be cut to the right dimensions and this is usually done by means of thermal cutting. In comparison to laser or plasma cutting, flame cutting (also known as oxy-fuel cutting (OFC)) shines by its dexterity to cut a big range of thicknesses and the lesser cost per unit cut.

However, in some cases, flame cutting can provoke undesired side effects on the steel plates, such as cracks. The occurrence of these anomalies depends on the material properties, cutting parameters and thickness of the plate. Thermal cutting removes around two millimetres of material from the cutting line creating the mentioned cutting edge. Near the cutting edge, a heat affected zone (HAZ) is originated due to the rapid heating and cooling. The big difference of temperature between the area close to the cutting edge and the rest causes thermal stresses. Moreover, the high temperatures within the HAZ provoke solid phase changes which, after cooling, create a non-homogeneous microstructure in the steel and, as a consequence, disrupt the already established properties of the plate. The solid-solid phases changes imply volume changes which add further stress. The microstructure and stress level combined with hydrogen content in the HAZ induce cold cracking. Cold cracks are usually formed when the HAZ cools down to about 150 °C or below, hence the term “cold crack”.Previous research [1, 2] shows that slowing down the cutting speed or preheating helps reduce the aforementioned side effects. Although slower speed leads to longer production time. Furthermore, the current preheating method consists of global preheating. This entails putting on hold the plates in industrial ovens for approximately 5 to 10 min until a uniform temperature between 25 and 200 °C is achieved.

In this thesis, three topics are investigated: flame cutting, induction preheating and optimal control of the preheating of steel plates.

The study of the flame cutting process is useful to accomplish a better understanding of the temperature map in the plate during the process. It has to be noticed that it is not possible to register the precise temperature values in the area to be cut or its surroundings. The rapid change in temperature is too fast for thermocouples to register, assuming that these do not melt during the thermal measurement.

There are very few publications studying flame cutting from a modelling and numerical simulation point of view in comparison to welding, laser or plasma cutting, which are similar physical processes. The main sources used are Lindgren et al. [1], Thiébaud et al. [3] and Jokiaho et al. [2]. The authors from [1] and [2] employ 2D-models to study the temperature evolution in a section transverse to the direction of flame cutting. On the other hand, a 3D-model is used by Thiébaud et al. [3] to study the quasi-stationary state (QSS) of the temperature in the plate.

The main contributions to flame cutting modelling and simulation from the present work have been published in Arenas et al. [4]. The work from [3] has been used to expand a QSS heat transfer model to couple it with solid-solid and also solid-liquid (melting) phase changes. The QSS character of the model is able to include the movement of the plate. The main novelty is the introduction of QSS phase equations which allow faster simulations than the standard time dependent rate laws. Results obtained include the liquid phase (molten region), which is used to identify the gap created by flame cutting (kerf), and the austenite phase to identify the heat affected zone and temperature in the remaining plate. This model allows to estimate the kerf unlike the previously cited sources that pre-define it. Moreover, the heat source model changes with the cutting speed. This feature based on the phenomenology of the cutting process is not included in previous models and enables its use for a range of cutting speeds instead of a single one. Temperature dependant steel properties are considered in the model which originate nonlinearities in the system.

The second topic we study is a new concept for preheating of steel plates for flame cutting. We examine the feasibility of changing from global to local preheating. Induction heating of steel is a very fast and energy efficient process since the heat is generated directly in the workpiece. The goal of the local preheating is to localize the heat in the immediate area to be affected by thermal cutting. One direct benefit is that the necessary energy would be lesser than with the aforementioned global preheating. Moreover, induction heating is easy to control and automatize, allowing to integrate it directly into the manufacturing chain.

The model employed to study the feasibility of induction preheating consists of the classic eddy currents model. It is mainly based on Hömberg et al. [5] where a 3D eddy currents model is coupled with the time-dependant heat equation to study the induction hardening of steel gears. The time-dependence of the heat equation is substituted by considering the same QSS aspect of the flame cutting model. On the other hand, the time-harmonic regime is considered instead of using the time scale of the frequency. Nonlinearities from temperature dependant properties are considered along with the magnetic permeability of the steel varying with temperature and magnetic field intensity. The goal is to achieve a uniform temperature from top to bottom only using an inductor on top of the plate as the setting studied does not

allow one on the bottom. Numerical simulations were used to obtain results from the model under different operating conditions. Results show, for example, that the heat from the top is spread to the bottom by conduction. Also, due to the *skin effect*, the heat arrives easier to the bottom when the frequency is as low as possible. Unfortunately, many more parameters have revealed to play a role when a specific preheating value wants to be achieved, e.g., thickness, distance from coil to flame and electric current intensity. In addition, experimental validation was carried out in collaboration with the University of Oulu to test the model.

Searching for the optimal parameters to achieve a specific preheating under different cutting settings is a very complicated multifield problem. Our approach to tackle this feature is to decouple the system. In this spirit we explore an optimal control problem where the preheating heat acts as control variable. This way, the heat source necessary to achieve a uniform temperature value in a specific region can be found easier. Moreover, a projection factor is added in the optimal control problem to ensure that the optimal source resembles the distribution of the heat power generated by an induction coil on top of the plate.

This optimal control problem is preceded by a thorough analysis to study the existence, uniqueness and regularity of the solutions of the system of flame cutting with preheating. This analysis was done in collaboration with Dr. Robert Lasarzik. The main novelty in this direction is that first order optimality conditions are derived for the involved nonlinear elliptic system. In comparison to previous works treating quasilinear systems ([6],[7],[8]), the system at hand deals with a quasilinear elliptic heat equation coupled to QSS phase fraction equations. The biggest difficulty however is hidden in the lower order terms, since these are non-monotone, which is essentially new up to our knowledge. The non-monotone terms can be handled due to their special structure, which allows to prove a comparison principle for the considered system. This comparison principle adapts the proof in Casas and Tröltzsch [6], which originates from Křížek and Liu [9] to the considered system. We have implemented a steepest descent algorithm based on the derived optimality conditions. The algorithm provides promising results to match the cutting speed and thicknesses that require different levels of preheating.

All this work has been done within the context of a European Industrial Doctorate (EID) called MIMESIS. The full name of MIMESIS is Mathematics and Materials Science for Steel Production and Manufacturing. Five institutions were part of the project which allowed for collaboration between them: EFD Induction in Norway; SSAB, Outokumpu, and the University of Oulu, in Finland; and Weierstrass Institute for Applied Analysis and Stochastics (WIAS) in Germany.

Modelling work was mainly done at WIAS while supported by material science experts from the University of Oulu and the experience of the industrial partner SSAB. Simulations were carried out by using the finite element package *pdelib2* [10] developed and maintained at WIAS. The results obtained were analysed and post-processed with MATLAB® and ParaView. Moreover, SSAB and the University of Oulu provided material data and experimental data necessary for the experimental validation.

The thesis is organized as follows. In the next chapter, Chapter 2, we introduce the flame cutting process within the context of thermal cutting and its phenomenology. We describe

the different phases in steel and derive the QSS phase equations. Results from the full flame cutting model are presented.

In Chapter 3, induction heating of steel is presented as an alternative to global preheating of steel plates. The eddy currents model coupled with the QSS heat equation is used to test the setting recommended by the industrial partner. Moreover, experimental data is compared with simulation results. The experience developed is used to describe a simple model for the distribution of dissipated power generated by the induction preheating device proposed.

Chapter 4 is devoted to the definition of an optimal control problem for the preheating of steel plates just before flame cutting. First, the existence, uniqueness and regularity of the solutions of the full system of flame cutting with preheating (state equations) are investigated. Optimality conditions are derived and then the optimal control problem is presented. The optimal control and respective temperature field obtained with the projected gradient method for a particular case are analysed to show the capabilities of the algorithm.

A summary of conclusions from the thesis and an outlook for further developments is given in Chapter 5.

2

Flame cutting of steel modelling and simulation

The goal of this work is to describe in detail a quasi-stationary state model which can be used to deeply understand the distribution of the heat in a steel plate and the changes in the solid phases of the steel and into liquid phase during the flame cutting process. We use a 3D-model similar to previous works from Thiébaud et al. [3] and expand it to consider phases changes, in particular, austenite formation and melting of material. Experimental data is used to validate the model and study its capabilities. Parameters defining the shape of the volumetric heat source and the power density are calibrated to achieve good agreement with temperature measurements. Similarities and differences with other models from literature are discussed. The main part of this chapter has been published in [4].

Outline. First, in Section 2.1, the concept and phenomenology of thermal cutting is introduced to contextualize flame cutting. It includes a review of literature around the state-of-art of modelling and simulation of flame cutting. In Section 2.2, we describe a mathematical model for flame cutting of steel plates, consisting of a quasi-stationary heat equation coupled with a set of equations describing the phase transitions in steel. The considerations for numerical approximation and material data are presented in Section 2.3. Section 2.4 is devoted to the presentation of the results and comparison with experimental data used for validation followed by some concluding remarks in Section 2.5.

2.1 Flame cutting of steel

2.1.1 Physical process

The content of this Subsection is a compilation of knowledge from [11–15].

Flame cutting context. Thermal cutting processes are applied in different mechanical and process engineering applications to produce components and for the preparation of welding

edges. The thermal cutting processes according to DIN 2310 can be classified into the following categories:

(i) Physics of the cutting process.

(ii) Degree of mechanisation.

(iii) Type of energy source.

(iv) Arrangement of water bath.

The physics of cutting processes can be further sub-classified as:

(i) Flame cutting: The material is mainly oxidised and the products are blown out by an oxygen jet.

(ii) Fusion cutting: The material is mainly fused and blown out by a high-speed gas jet.

(iii) Sublimation cutting: The material is mainly evaporated. It is transported out of the cutting groove by the created expansion or by additional gas.

The gas jet and/or evaporation implemented in all these processes is responsible for the ejection of molten material or the emerging reaction products such as slag.

According to ISO 13600, an energy carrier is either a substance or a phenomenon that can be used to produce mechanical work or heat or to operate chemical or physical processes. In thermal cutting, the energy carriers that produce heat are:

(i) Gas.

(ii) Electrical gas discharge: sparks, arc or plasma.

(iii) Beams: laser beam (light), electron beam or ion beam.

Different methods of thermal cutting have been developed that use gas as the main energy carrier. The classification is the following according to DIN 8580:

(i) Flame cutting.

(ii) Metal powder flame cutting.

(iii) Metal powder fusion cutting.

(iv) Flame planing.

(v) Oxygen-lance cutting.

(vi) Flame gouging or scarfing.

(vii) Flame cleaning.

Real-world implementations of flame cutting and oxygen lance being can be seen in Figure 2.1. It is a clear example that for different settings, in this case thickness, one method is more suitable than another.

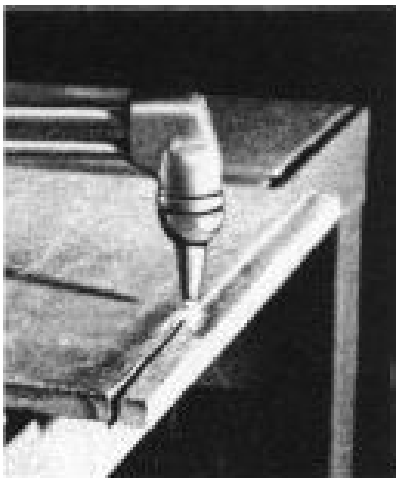

(a) Flame cutting of thin plate.

(b) Oxygen lance used in conjunction with cutting torch to remove 7 t riser from 9 t steel casting.

Figure 2.1: Two methods of thermal cutting with gas [16].

Flame cutting phenomenology. Flame cutting is based on the chemical relationship between oxygen and iron metals when the latter are brought to ignition temperature (760 to 871 °C). The ignition temperature of a substance is the least temperature at which the substance starts combustion. This temperature is achieved by means of a flame created by the combustion of a fuel gas and a oxygen stream. The metal after ignition has a great affinity for oxygen and immediately combines with it to form various oxides within the oxygen stream. As combustion is an exothermic reaction, this causes the metal to be disintegrated and burned with great rapidity. Only the metal within the direct path of the oxygen jet and at ignition temperature is affected. During the process, the ignition temperature is maintained on the top surface of the plate by the heating flame and below the surface by thermal conduction and convection. In cutting, a gap is formed which is called kerf or groove. This is a narrow incision which is uniformly smooth and has parallel walls if cut properly. A general scheme of flame cutting is depicted in Figure 2.2.

The simplest flame cutting equipment consists of two cylinders: one for oxygen and one for the fuel gas. This is why flame cutting is also known as oxy-fuel gas cutting, oxy-fuel cutting, oxy-flame cutting or by its abbreviation OFC. The cutting device also requires gas flow regulators and gages, gas supply hoses, and a cutting torch with a set of exchangeable cutting tips. Figure 2.3 shows a commercial torch and a nozzle. The selection of torch and nozzle is important as it influences on the maximum cutting thickness, the cutting quality, and the geometry of the cutting edge. Figure 2.4 is a schematic of the flame cutting process with common terminologies labelled in the same.

This process is suited for automation and it is also easy to apply on site. Cutting machines, employing one or several cutting torches guided by solid template pantographs, optical line tracers, numerical controls, or computers, improve production rates and provide superior cut quality.

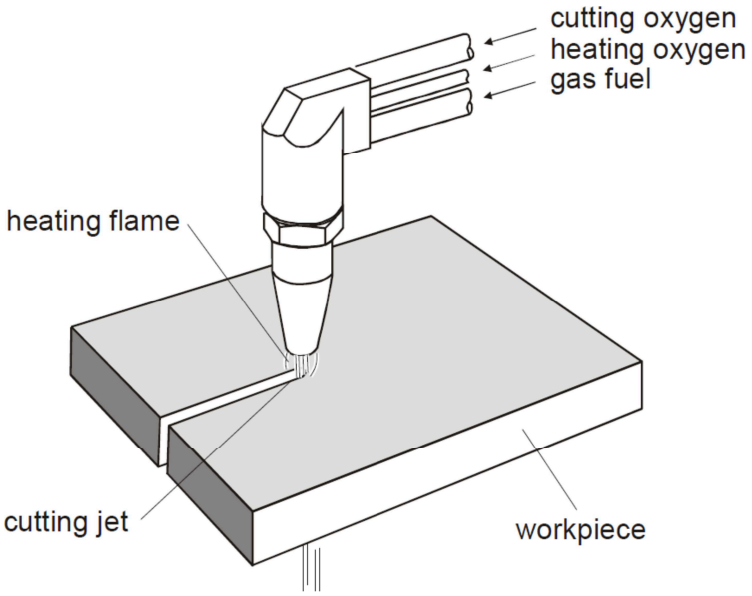

Figure 2.2: General scheme of flame cutting [11].

Cuttable metals. In flame cutting, the thermal conductivity of the material must be low enough to constantly maintain the ignition temperature. Moreover, the material has to fulfil the following requirements:

(i) The ignition temperature must be lower than the melting temperature.

(ii) The melting temperature of the oxides must be lower than the melting temperature of the material itself.

In accordance, only steel or titanium materials fulfil the conditions for flame cutting. On the contrary, stainless steel, cast iron and non-ferrous metals form oxides whose melting points are higher than the material (refractory oxides). However, the method known as metal powder flame cutting allows to surpass this impediment. A chemical flux or metal powder is injected into the flame to form a low melting point slag, which allows to cut the material successfully. High-carbon steels may be cut successfully if preheated to a temperature depending on the carbon content. The higher the carbon content, the greater the degree of preheating required.

Plate thickness. The rate of heat transfer in the workpiece influences the heat balance for cutting. As the thickness of the metal to be cut increases, more heat is needed to keep the metal at its ignition temperature. Increasing the preheat gas flow and reducing the cutting speed maintains the necessary heat balance. Oxygen flow must also increase as the thickness of the metal to be cut increases. The jet of cutting oxygen must have sufficient volume and velocity to penetrate the depth of the cut and still maintain its shape and effective oxygen content.

Cutting parameters. Flame cutting operations combine more than 20 variables. Suppliers of cutting equipment provide tables that give approximate gas pressures for various sizes and styles of cutting torches and tips and recommended cutting speeds; these variables are operator controlled. Where dimensional accuracy and squareness of the cutting edge are important, the

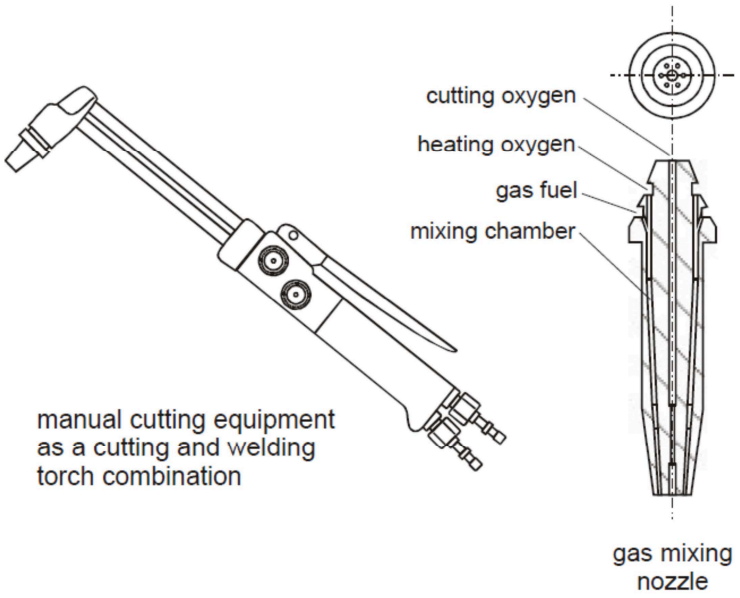

Figure 2.3: Cutting torch and nozzle shape [11].

operator must adjust the process to minimize the kerf, the width of metal removed by cutting, and to increase smoothness of the cutting edge. Careful balancing of all cutting variables helps attain a narrow kerf and smooth edge. The thicker the work material, the greater the oxygen volume required and therefore, the wider the cutting nozzle and kerf.

Oxygen and gas fuels. The cutting speed and cutting edge quality are influenced by the purity of the oxygen stream. Thus, nozzle design plays a significant role in protecting the oxygen stream from air entrainment. The purity of oxygen should be at least 99.5 %. A decrease in purity of 1 % will typically reduce the cutting speed by 25 % and increase the fuel gas consumption by 25 %.

The five most commonly used fuel gases are acetylene, propane, MAPP (methylacetylene-propadiene), propylene and natural gas. The properties of the gases are given in Table 2.1. The relative performance of the fuel gases in terms of pierce time, cutting speed and cutting edge quality, is determined by the flame temperature and heat distribution within the inner and out flame cones. Heat distribution in the flame is a good indicator of the potential performance of a particular gas. For example, natural gas, that releases most of its heat in the outer flame is well suited to heating and heavy cutting.

Table 2.1: Fuel gas characteristics [17].

Fuel gas	Maximum flame temperature [°C]	Oxygen to fuel gas ratio [vol]	Heat distribution [kJ/m^3]	
			Primary	Secondary
Acetylene	3160	1.2:1	18190	35882
Propane	2828	4.1:1	10433	85325
MAPP	2976	3.3:1	15445	56431
Propylene	2896	3.7:1	16000	72000
Hydrogen	2856	0.42:1	-	-
Natural gas	2770	1.8:1	1490	35770

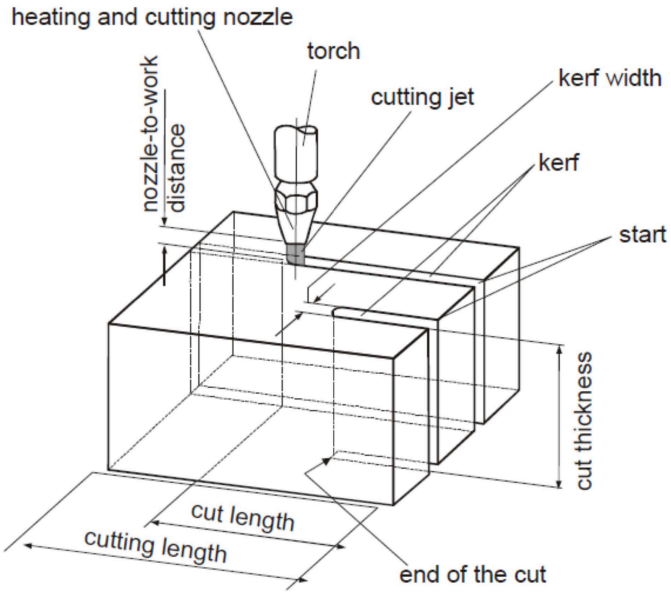

Figure 2.4: Flame cutting terms [11].

Drag. If the flow of oxygen is large and well collimated (accurately parallel), the rate of cutting through the depth of the cut is approximately constant. If oxygen flow is insufficient, or cutting speed too high, the lower portions of the cut react more slowly, and the cutting face curves behind the torch. The horizontal distance between point of entry and exit is called drag. Increasing cutting speed or reducing oxygen flow makes less oxygen available at the bottom of the cut, causing the bottom of the cut to "drag" behind the top of the cut. Drag is a rough measure of cut quality. The key to quality cuts is control of heat input. Excessive drag may lead to incomplete cutting. In very thin plates, drag has little significance, while in very thick plates the goal is to avoid excessive drag. Figure 2.5 shows cut qualities obtained with different cutting parameters.

Carbonisation. In flame cutting, carbonisation (increase in carbon content) may occur at the cutting edge. This results in hardening of the flame cut surface. Carbonisation occurs due to the selective oxidation of the steel. The iron oxide layer that forms on the cut surface prevents the formation of carbon monoxide, thereby increasing the carbon content in the molten layer. In structural steels, the depth of this carbonised layer is less than 0.1 mm. The width of the heat affected zone (HAZ) in flame cutting is generally less than 5 mm. With increase in carbon content, hardenability of the cutting edge also increases. The cooling rate during and after thermal cutting depends on plate thickness. It increases with plate thickness and this leads to increase in grain size. This along with carbonisation of the cut surface results in increased hardness of the flame cut surface.

Global preheating. Therefore to prevent higher cooling rate in thicker plates, preheating is done. Preheating decreases the hardness of the flame cutting edge and improves its formability. It also makes the machining of the plate edge easier and speeds up the flame cutting procedure. The need for preheating depends on the plate thickness, its chemical composition as well as cutting process (gas) and cutting speed. Because an increased carbon content demands more heat, preheating is carried out for high carbon steel. Carbon accumulates at the cutting

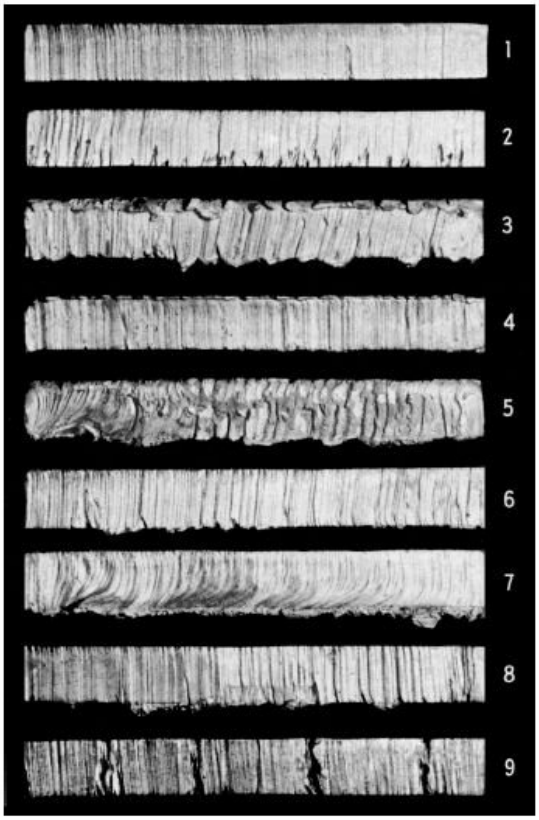

Figure 2.5: Comparison of edge quality. One good cut and eight poor-quality cuts. All cuts were made in 25.4 mm steel plates [14].

surface, so a very high degree of hardness is to be expected. Should the carbon content exceed 0.45 % and should the material not have been subject to prior heat treatment, hardening cracks on the cutting surface are regarded as likely [11]. Preheat improves cutting speed significantly, allowing faster torch travel for greater productivity and reduced consumption of fuel gas. Moreover, global preheat smooths the temperature gradient between the base metal and the cutting edge, possibly reducing thermal stress and minimizing hardening effects in some steels.

According to [15] (1993), preheating to 260 to 315 °C is sufficient for high-carbon steels; alloy steels may require preheating as high as 540 °C. Preheat temperature should be maintained during cutting. Thick preheated sections should be cut as soon as possible after the piece has been withdrawn from the furnace. The preheating temperature θ (°C) for different plate thicknesses h (mm), according to Ruukki Metals Oy [18] (2011), can be calculated as follows:

$$\theta = 500\sqrt{\mathrm{C_{eq}} - 0.45}, \text{ for plate thickness } h = 5 \text{ to } 100\,\mathrm{mm}. \tag{2.1}$$

$$\theta = 500\sqrt{\mathrm{C_{eq}}(1 + 0.0002h) - 0.45}, \text{ for plate thickness } h > 100\,\mathrm{mm}. \tag{2.2}$$

$$\mathrm{C_{eq}} = \mathrm{C} + 0.155(\mathrm{Cr} + \mathrm{Mo}) + 0.14(\mathrm{Mn} + \mathrm{V}) + 0.115\mathrm{Si} + 0.045(\mathrm{Ni} + \mathrm{Cu}). \tag{2.3}$$

Equation (2.3) is a carbon equivalent ($\mathrm{C_{eq}}$) formula. Carbon equivalent formulae were originally developed to give a numerical value for a steel composition which would give an indication of a carbon content which would contribute to an equivalent level of hardenability for that steel. These formulae were later extended to represent the contribution of the composition to the

hydrogen cracking susceptibility of steel. They are also used as compositional characterising parameters for other properties that may be linked to hardness, such as toughness and strength [19]. A compilation of carbon equivalent formulae available in literature can be found in [20].

Specific values of preheating for different steel grades and plate thickness manufactured by SSAB AB extracted from [21] (2020) can be seen in Figure 2.6. As mentioned before, the higher the C-content and thickness, the greater the degree of preheating required. The values ranging from 20 to 175 °C are consistent with this fact. The three steel types considered are Raex® 400, 450 and 500 which have 0.26 %, 0.28 % and 0.30 % carbon content respectively. The preheating value of 20 °C for some thicknesses could be considered that preheating is not required if the ambient temperature is high enough. These temperature preheating values are assumed to be obtained with a different formula from Equations (2.1)-(2.3). According to the previous formulae, the preheating temp should not depend on temp if thickness is below 100 mm.

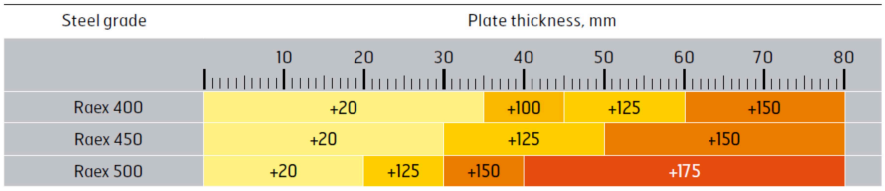

Figure 2.6: Recommended working temperature (°C) for flame cutting [21].

Local preheating. Instead of preheating the whole plate, a localized preheating around the cutting line could be considered. Local preheating heats the volume of the workpiece enclosing the HAZ of the cut. If the volume of material to be heated is small, the flame of a cutting torch can be used for preheating. When the workpiece is thick and broad, a special heating torch may be necessary. Workpieces must be heated uniformly through the section to be cut, without excessive temperature gradient.

Buckling. In cuts made from large plates, the cutting thermal cycle changes the shape of narrow sections and leaves residual stress in the large section (see Figs. 2.7-2.8). The temperature gradient near the cut is steep, ranging from melting point at the cut to room temperature a short distance from it. The plate does not return to its original shape unless the entire plate is uniformly heated and cooled. The flame cutting operation may lead to heat induced shrinkage of the cutting edges causing alignment problems in structural fabrication. Also the thermal stresses may cause buckling of the edges.

Figure 2.7: Edge buckling due to oxy-acetylene cutting [12].

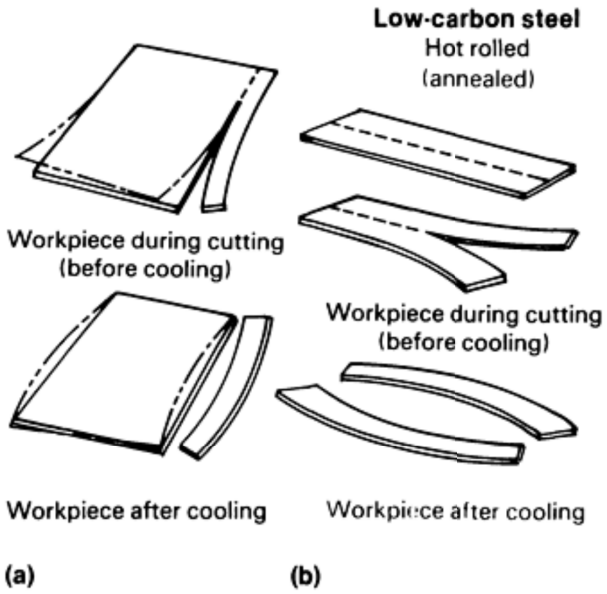

Figure 2.8: Effects of flame cutting thermal cycle on shape of sections. (a) plate with large restraint on one side of kerf, little restraint on the other side. Phantom lines indicate direction of residual stress that would cause deformation except for restraint. (b) plate with little restraint on either side [15].

Preheating the workpiece can reduce distortion by reducing differential expansion, thereby decreasing stress gradients. Careful planning of the cutting sequence helps. For example, when trimming opposite sides of a plate, both sides should be cut in the same direction at the same time. In general, the larger portion of material should be used to retain a shape for as long as possible; the cutting sequence should be balanced to maintain even heat input and resultant residual stresses about the neutral axis of plate or part.

Thermal cutting comparison. Figure 2.9 shows a comparison of the different plate thicknesses which were cut using different processes. For plate thickness up to 12 mm (steel plate), laser beam cutting is the preferred precision cutting process. Plasma cutting of plates thicker than 3 mm allows higher cutting speeds, in comparison to laser beam cutting, the cutting quality, however, is significantly lower. Flame cutting is used for cutting plates thicker than 3 mm. The flame cutting process, which is also referred to as burning or flame cutting, can cut carbon and low-alloy plate of virtually any thickness. Castings more than 760 mm thick commonly are cut by flame cutting processes. Regarding the cutting speed, Figure 2.10 shows the cutting speed required for a particular thickness using three different devices: oxygen cutting (OFC), CO_2-laser and plasma cutting. The cutting speeds for low thickness are significantly higher for CO_2-laser and plasma cutting. However, with an increasing plate thickness the difference in the cutting speed is reduced. Plates with a thickness of more than 40 mm may be cut faster using the flame cutting process.

Figure 2.11 shows the cost per metre of cut of the three thermal cutting processes. In this case, flame cutting is the lowest for thicknesses over 10 mm. The cost in all cases increases with thickness. A deeper review of these three cutting processes can be found in [22].

As a summary, metals can be cut faster by flame cutting. Setup is generally simpler and faster than for machining and about equal to that of mechanical severing. Manual flame

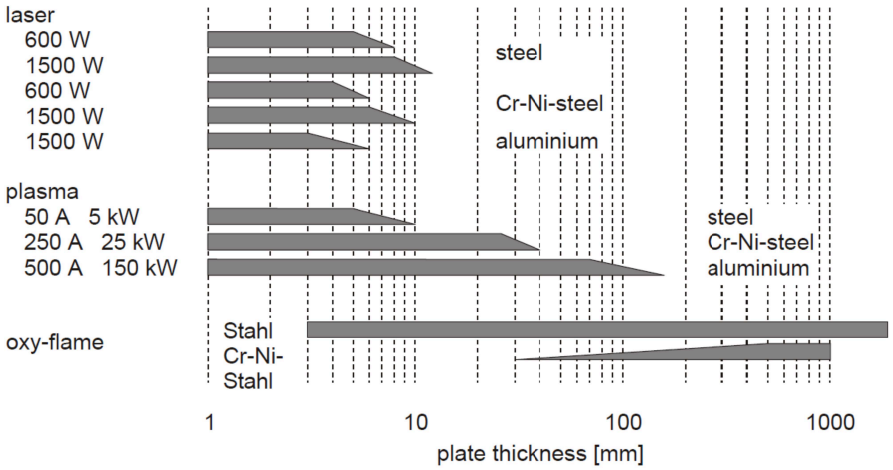

Figure 2.9: Fields of application of cutting processes [11].

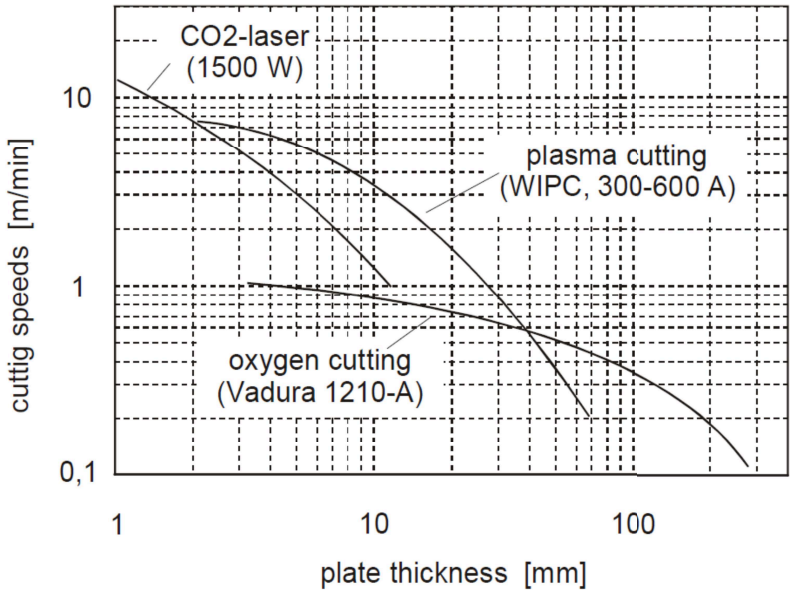

Figure 2.10: Cutting speeds of thermal cutting processes [11].

cutting equipment costs are low compared to machine tools. On the other hand, because flame cutting relies on oxidation of iron, it is limited to cutting steels and cast iron. Heat generated by flame cutting can degrade the metallurgical properties of the work material adjacent to the cutting edges. Hardenable steels may require preheat and/or postheat to control microstructure and mechanical properties.

2.1.2 Literature review

In contrast to welding, which is a similar physical process to flame cutting, there are very few publications studying flame cutting from a modelling and numerical simulation point of view.

In Lindgren et al. [1] the authors use a 2D-model to study the temperature evolution in the section transverse to the direction of the flame cutting. The heat input is adjusted with experimental measurements of two isothermal lines. The paper reveals the decrease in residual stress with a preheating stage of the plate prior to cutting using a model for mechanical analysis. Jokiaho et al. [2] employ the commercial finite element software ABAQUS to model the flame

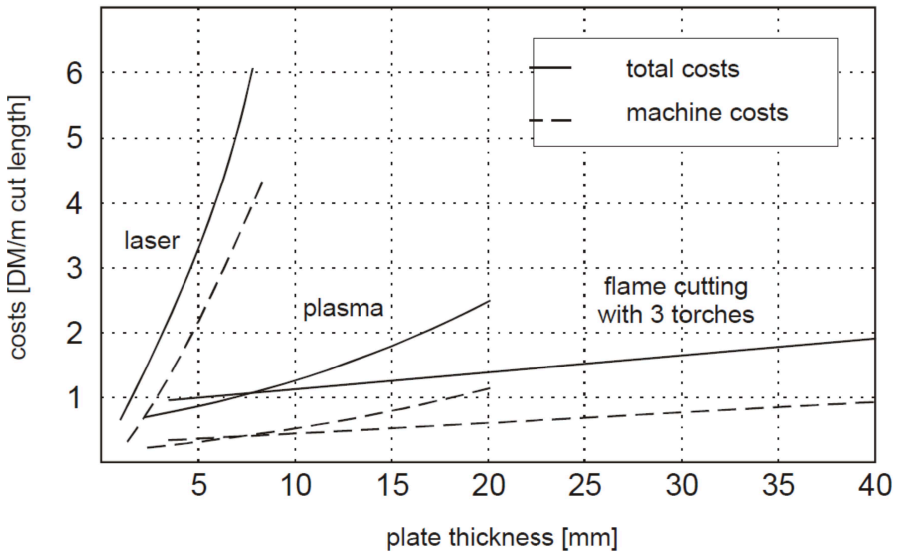

Figure 2.11: Thermal cutting costs [11].

cutting of thick plates. Again, a 2D-model is used to register the nodal temperature history in the transverse plane. Different values for the heat input are used for different cutting speeds. The aforementioned values are calibrated such that the temperatures in the middle plane of the plate (half the thickness) do not reach the melting point. The study focuses on the stress analysis under different operating conditions: thickness, speed, preheating stage. Bae et al. [23] work with ABAQUS for a 2D-model. The authors adopt a more complex definition of the heat flux. It is divided in three parts: upper surface due to the reaction between ethylene and oxygen, cutting line due to the reaction between oxygen and iron, and bottom of cutting line due to the heat conducted by the molten droplets. The model predicts the shape of the HAZ for diverse plate thicknesses, cutting speeds and flow rates of oxygen/ethylene. Thiébaud et al. [3] study the quasi-steady state of the temperature distribution during flame cutting with a 3D-model. The heat input is modelled as a volumetric heat source with a cylindrical-like shape. The simulation domain contains a gap related to an assumed kerf width. Two parameters are used to match the temperature profiles measured by several thermocouples on the top and bottom of the plate. These parameters are the heat density within the flame and the heat transfer coefficient in the aforementioned gap. Good matching with the experimental data is achieved.

In Gross [24], a sophisticated multi-physics 3D-model is considered including gas dynamics and the melting of steel. However, the author concludes that the computational effort for such a complex model is too costly for current hardware.

The present study is based on a quasi-stationary state 3D-model similar to the one used by Thiébaud et al. [3]. Using experimental data, the heat input power of the flame is adjusted to fit the data in the best possible way. The main novelty is the introduction of a quasi-stationary state (QSS) model comprising an energy balance coupled with two transport equations to model the occurring solid-liquid and solid-solid phase transitions. This approach allows for a more precise estimation of kerf and the heat affected zone.

2.2 Model

2.2.1 Domain

Flame cutting of steel plates consists of removing a small amount of material from the plate along a straight cutting line dividing it in two pieces and leaving them with a very regular edge. For symmetry reasons, only one half of the plate will be considered, denoted by $\widetilde{\Omega}$. Due to the big size of the steel plate in comparison to the flame and the straight cutting trajectory, later on we will describe the cutting process by a quasi-stationary state (QSS) model. The plate moves with velocity $\boldsymbol{v}$ relative to the stationary torch. We define a cut-out Ω around the torch, which is is represented by the subdomain Λ in Figure 2.12. The symmetry plane is $\{y = 0\}$.

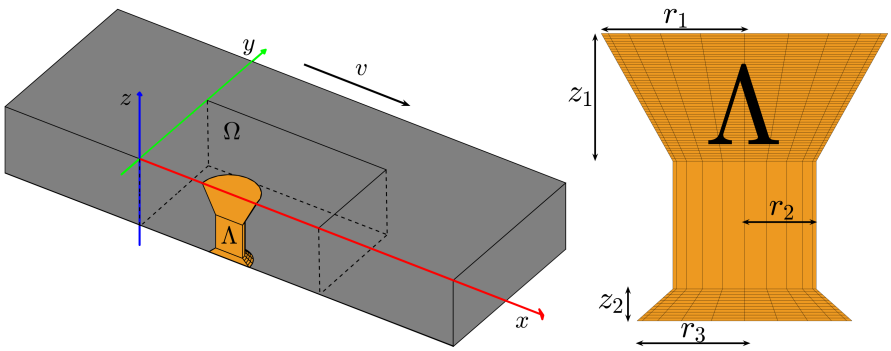

Figure 2.12: Half of steel plate and flame representation.

2.2.2 Heat Source

The burning and removal of material is a complex process that can be described in three steps:

(i) A torch located on top of the plate raises the steel to its ignition temperature ($\sim 960\,°C$ [25]). For this, the torch creates a flame using a mixture of oxygen and a fuel gas, commonly acetylene, butane or propane.

(ii) The iron in the steel reacts with the highly concentrated oxygen from the torch in an exothermic oxidation reaction adding more heat to the plate.

(iii) The steel below the torch reaches melting temperature ($\sim$1537 °C). By heat conduction the melting temperature reaches the bottom of the plate. Immediately, the molten steel is flushed away by the high pressure oxygen stream.

These steps occur within a matter of seconds and additionally, the plate is moving in a fixed direction, thus separating the workpiece in two. The resultant edges of each new half of the steel are called cutting edges and the gap created is named kerf or groove. The process is ruled by two main factors: the cutting speed $\boldsymbol{v}$ and the flame. Depending on the steel properties and the thickness of the plate, a suitable speed must be chosen by the operators in the factory. The shape of the flame is determined by the torch used while the power depends on the combustion gas selected and the pressure of the oxygen and fuel gas stream.

Mathematically, the heat source $Q(\boldsymbol{v})$ can be characterized in terms of the shape of the flame created by the torch. It is defined as a constant power density [W/m^3] within a particular

volume Λ and assumed to be zero outside of it. More precisely, the power density is determined by a constant value for power P [W] divided by the volume of Λ. The heat source is uniformly distributed within the volume Λ, which is similar to a cylinder whose radius changes with height, specifically Λ can be identified as a cylinder with a truncated cone on the top and at the bottom (see Figure 2.12). The variation of shape, and therefore heat, depending on height is based on physical reasons. While on the cutting plane most of the heat comes from the oxidation of iron and concentrates in a thin cylindrical volume below the torch, extra heat input exists close to the top and bottom surfaces of the plate: at the bottom by the presence of droplets of molten metal and on the top surface by the reaction between oxygen and fuel gas [1, 3, 23, 2].

In Figure 2.13 two sets of isothermal curves in cross sections parallel and with growing distance to the cutting surface are depicted. The sets correspond to a speed of 135 and 270 mm/min, respectively, during the flame cutting process. The isothermal lines were estimated using the temperature records from thermocouples (attached to holes drilled in the plate), microstructure study and literature. Both sets start in the cutting edge of the remaining half after flame cutting. The cutting edge is almost aligned with the 1537 °C curves. Its shape can be regarded as an experimental evidence for the assumed shape of the volume Λ. Moreover, higher temperatures are reached further within the plate in the slower case as the heat source has more influence and due to more time for heat conduction. This fact can also be seen in Jokiaho et al. [26] (2018), where a conclusion of the flame cutting experiments is that the heat affected zone width depends on cutting speed.

Furthermore, it is important to mention that the kerf (removed area) in both cases is different, being smaller in the faster case. In Duan et al. [27], it is stated that the kerf width is generally assumed to be constant in most mathematical models of flame cutting. However, a large error may be produced if this variation in width with respect to thickness and cutting speed is neglected. Hence, we assume that the kerf size decreases with increasing speed and model this effect by changing the radius of Λ as a function of velocity $\boldsymbol{v}$.

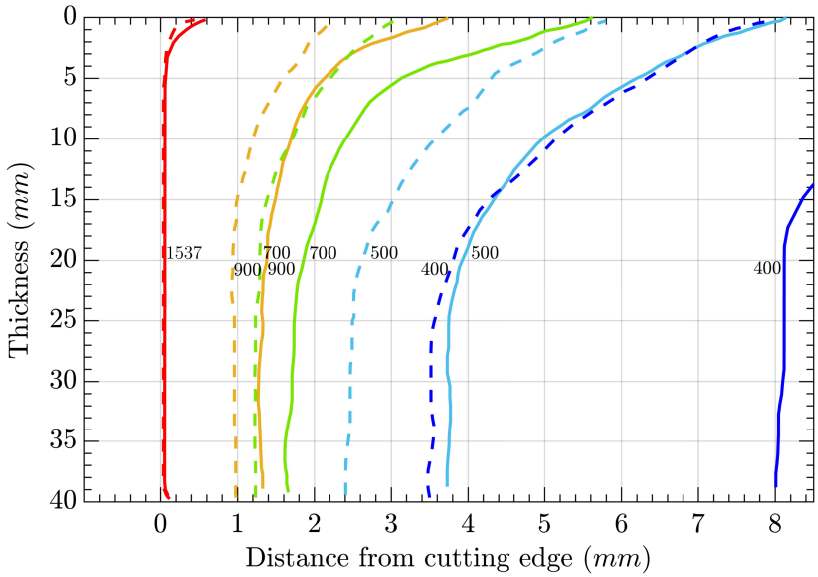

Figure 2.13: Isothermal lines in the plane transversal to the cutting direction. Case 135 mm/min (solid) and case 270 mm/min (dashed).

In view of all these considerations, we define Λ as

$$\Lambda(\boldsymbol{v}) = \left\{ \boldsymbol{x} \in \widetilde{\Omega} \mid (x - x_\Lambda)^2 + (y - y_\Lambda)^2 \leq R(z, \boldsymbol{v})^2, -h \leq z \leq 0 \right\}. \tag{2.4}$$

Here, (x_Λ, y_Λ) are the coordinates of the symmetry axis of Λ. The simplest way to model a source with the above mentioned phenomena is with only five parameters that define the shape of the heat source along the complete thickness h of the plate: r_1, r_2, and r_3 are the upper, medium and lower radii, respectively, and z_1 and z_2 the heights of the top and bottom truncated cones, respectively (see Figure 2.12).

We define the function $R(z, \boldsymbol{v})$ from Equation 2.4 reflecting the radial change of Λ according to height and speed in a separable way as a product of two functions, i.e.,

$$R(z, \boldsymbol{v}) = C(\boldsymbol{v})\bar{R}(z), \tag{2.5}$$

$$\text{with } \bar{R}(z) = \begin{cases} \frac{r_2 - r_1}{\bar{z}_1} z + r_1, & z > -\bar{z}_1 \\ r_2, & -\bar{z}_1 \geq z \geq -h + \bar{z}_2 \\ \frac{r_2 - r_3}{\bar{z}_2} (z + h - \bar{z}_2) + r_2, & z < -h + \bar{z}_2 \end{cases} \tag{2.6}$$

The definition of $\bar{R}(z)$ evidences the difference in radii with height and can be seen in Figure 2.14. On the other hand, $C(\boldsymbol{v})$ takes into account that the faster the plate moves the smaller the area of influence of the flame gets. Thus, for convenience, $C(\boldsymbol{v})$ is assumed to be a linear, monotonically decreasing function that causes the radii of Λ to be scaled with velocity.

All in all, the heat source $Q(\boldsymbol{v})$ is then defined as

$$Q(\boldsymbol{v}) = \frac{P}{|\Lambda(\boldsymbol{v})|} \chi_{\Lambda(\boldsymbol{v})} \tag{2.7}$$

with $\chi_{\Lambda(\boldsymbol{v})}$ the characteristic function of the volume $\Lambda(\boldsymbol{v})$, i.e., it takes value 1 within $\Lambda(\boldsymbol{v})$ and 0 outside.

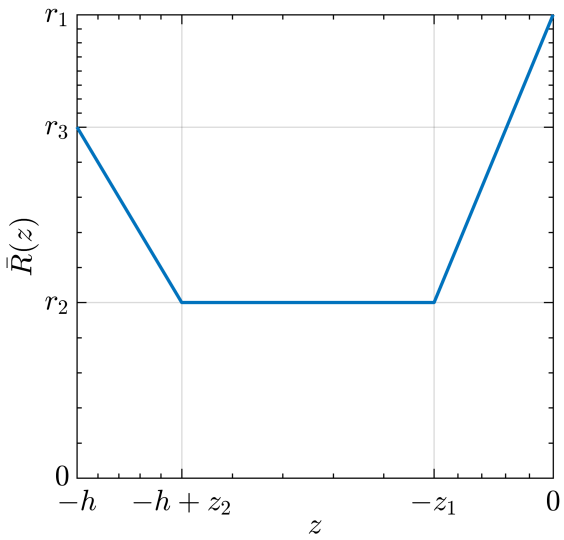

Figure 2.14: Definition of the function $\bar{R}(z)$ for the heat source.

2.2.3 Phase Transitions

During a heating process, steel undergoes microstructural changes affecting its physical properties. At room temperature, combinations of four different phases can be distinguished in the steel: ferrite, pearlite, bainite and martensite. The presence and the proportion of each phase depends on the type of steel and its chemical composition, and on the heat treatment that the material has been subjected to. If the steel temperature grows sufficiently high, the previous solid phases are transformed into a new high temperature phase called austenite. This process is called austenitization. During a cooling cycle, this austenite is dissolved into the previous phases. The volume fraction of the remaining phases is determined by the local cooling rate. For more detailed information we refer to [28].

During flame cutting, around the cutting plane, a portion of steel is molten and removed while in the neighbourhood of this kerf a Heat Affected Zone (HAZ) is formed. This HAZ is generated at the cutting edge of the steel plate due to large thermal gradients [26]. Phase transitions occur in the HAZ as the austenitization temperature is reached. The HAZ is an important region to study as it is the area where cracks have been found to appear, eventually leading to quality losses and customer complaints.

For modelling the flame cutting process it is important to account for the melting of steel and thus to estimate the size of the kerf. To this end, we add the relative fraction of molten steel as an extra phase to our phase transition model. In Hömberg and Weiss [29], a transient model based on the Leblond-Devaux model is proposed that reproduces the relative volume fractions of the different solid phases of steel during a heating and cooling cycle.

We define the HAZ as the area where austenitization has happened. Thus, to predict its size, which will provide information about the possible occurrence of cracks, it is sufficient to keep track of the formation of austenite. With this in consideration, we propose a reduced model, based on [29], consisting of a rate law for austenite a and liquid phase (molten steel) l with θ being the temperature. The corresponding system of equations for these two phases is the following:

$$\dot{l} = \frac{1}{\tau_l}[l_{eq}(\theta) - l]_+, \tag{2.8a}$$

$$\dot{a} = \frac{1}{\tau_a}[a_{eq}(\theta) - a - l]_+ - \dot{l}, \tag{2.8b}$$

$$l(0) = a(0) = 0. \tag{2.8c}$$

Here, l_{eq} and a_{eq} represent the equilibrium volume fraction of liquid and austenite phase, respectively, at temperature θ. The equilibrium volume fraction of the liquid phase $l_{eq}(\theta)$ should have the maximum value 1, when the temperature exceeds 1537 °C (melting point). Tacitly neglecting a mushy zone we define $l_{eq}(\theta) = H(\theta - 1537)$, where H is the Heaviside function. In addition, we define the positive part function as $[x]_+ = xH(x)$.

For the austenite phase a, equation (2.8b) reflects the fact that no austenite should form at the expense of liquid during heating but austenite can be transformed to liquid phase. Here, $a_{eq}(\theta)$ is the austenite equilibrium volume fraction and can be derived from a non-isothermal austenitization diagram. It has value 0 below austenitization temperature A_s and then is assumed to increase linearly until the maximum value 1 is reached at A_f temperature, both

depending on the chemical composition of the steel grade under consideration. There are two time constants τ_l and τ_a in equations (2.8a) and (2.8b) to adjust the transformation kinetics. The necessary initial conditions for liquid and austenite are stated in (2.8c).

Figure (2.15) shows the evolution of phase volume fractions obtained after solving (2.8a)-(2.8c) with a temperature history $\theta(t)$ from flame cutting. In a small fraction of time t, the rapid rise in temperature takes the steel to austenitization temperature and immediately into melting.

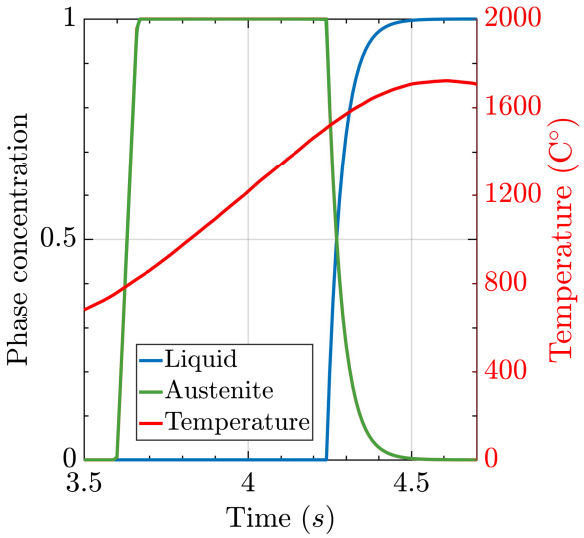

Figure 2.15: Evolution of volume fractions as solutions to (2.8a)-(2.8c) during flame cutting.

This model can be summed up as a system of rate laws (ODEs) determined by temperature θ and the already present phase fractions,

$$\dot{\boldsymbol{\zeta}}(t) = \boldsymbol{f}(\theta, \boldsymbol{\zeta}), \tag{2.9}$$

where $\boldsymbol{\zeta}$ is the vector of phase fractions. For the liquid and austenite model we have

$$\boldsymbol{\zeta} = (l, a)^T \quad \text{and} \quad \boldsymbol{f} = (f_l(\theta, l), f_a(\theta, a, l))^T. \tag{2.10}$$

Due to the big size of the steel plate in comparison to the flame and the straight cutting trajectory, we now switch to a quasi-stationary state (QSS) setting to model the flame cutting heating process, allowing for more efficient simulation. The requirement for a valid QSS approach is that an observer located on the heat source, i.e., the flame, will notice no change in the temperature distribution around it, while the plate moves with constant velocity under the torch. To obtain the QSS equation for the phase evolution system, first we consider the equation to be defined in the whole spatial domain $\widetilde{\Omega}$,

$$\dot{\boldsymbol{\zeta}}(\boldsymbol{x}, t) = \boldsymbol{f}(\theta, \boldsymbol{\zeta}) \quad \forall \boldsymbol{x} \in \widetilde{\Omega}. \tag{2.11}$$

We describe the moving plate relative to the stationary heat source [30]. To this end, we replace $\boldsymbol{x}$ by a new coordinate $\boldsymbol{\xi}$ subject to a given constant cutting speed $\boldsymbol{v}$, i.e., we define

$$\boldsymbol{\xi} = \boldsymbol{x} - \boldsymbol{v}t \tag{2.12}$$

such that the phase fractions ζ_i are stationary, i.e., we assume

$$0 = \frac{d}{dt}\zeta_i(\boldsymbol{x} - \boldsymbol{v}t, t) = -\boldsymbol{v} \cdot \nabla\zeta_i + \frac{\partial \zeta_i}{\partial t}.$$

Then, each component of Equation 2.11 can be rewritten as

$$\boldsymbol{v} \cdot \nabla\zeta_i = f_i(\theta, \boldsymbol{\zeta}), \quad \forall \boldsymbol{\xi} \in \Omega. \tag{2.13}$$

The domain Ω is stationary and has to be chosen sufficiently big.

Equation (2.13) is also known as transport equation. Altogether, the time-dependent evolution model of liquid and austenite phase (2.8a)-(2.8c) can be rewritten as the following quasi-stationary system of transport equations,

$$\boldsymbol{v} \cdot \nabla l = \frac{1}{\tau_l}[l_{eq}(\theta) - l]_+ \qquad \text{in } \Omega, \tag{2.14a}$$

$$\boldsymbol{v} \cdot \nabla a = \frac{1}{\tau_a}[a_{eq}(\theta) - a - l]_+ - \boldsymbol{v} \cdot \nabla l \qquad \text{in } \Omega, \tag{2.14b}$$

$$l = a = 0 \qquad \text{on } \{x = 0\}, \tag{2.14c}$$

$$\frac{\partial l}{\partial \boldsymbol{n}} = \frac{\partial a}{\partial \boldsymbol{n}} = 0 \qquad \text{on } \partial\Omega\backslash\{x = 0\}. \tag{2.14d}$$

The system of equations (2.14) reflects the development of the liquid and austenite phase during a heating process while taking into account the movement of the domain Ω with respect to the heat source Λ. From now on, for notation purposes, we will denote the variable $\boldsymbol{\xi}$ as $\boldsymbol{x}$ and drop the t dependency. It has to be noticed that the previous initial conditions from (2.8c) are substituted by boundary conditions. Equation (2.14c) is a Dirichlet condition indicating that there is no volume fraction of liquid or austenite in the in-flow plane, far from the heat source. Otherwise, the homogeneous Neumann condition (2.14d) reflects that stationarity has been achieved on the outflow boundary.

2.2.4 Complete System

The goal of the model is to determine the heat distribution in a moving steel plate during flame cutting with the subsequent HAZ and the trail of molten steel. The big dimensions of a steel plate (400 mm long) in comparison to the heat affected zone caused by the flame (5 mm) allow to consider that a quasi-stationary state (QSS) is reached in the workpiece. Accordingly, for the temperature θ in the plate, we can employ the quasi-stationary state (QSS) heat equation [30],

$$\rho(\theta)\, C_p(\theta)\, (\boldsymbol{v} \cdot \nabla\theta) - \nabla \cdot (\kappa(\theta, l)\, \nabla\theta) = q \quad \text{in } \Omega. \tag{2.15}$$

Different material parameters are required for this equation: density ρ, specific heat capacity C_p and thermal conductivity κ. One important aspect is that these properties are temperature dependent, adding nonlinearities to equation (2.15).

As mentioned earlier, the molten steel is flushed away during the cutting process. This has to be taken into account, otherwise, the liquid layer would act as an additional heat source (see [3]) increasing the HAZ artificially. To incorporate this effect into our model we propose a

mixture ansatz for the thermal conductivity, i.e.,

$$\kappa(\theta, l) = \kappa_0(\theta)(1 - l) + \delta\kappa_0(\theta)l. \tag{2.16}$$

Here, κ_0 is the thermal conductivity of steel and $\delta > 0$ is a small parameter chosen such that on the one hand heat diffusion through the kerf is negligible and on the other hand numerical instabilities caused by a degenerating diffusion coefficient are avoided.

The term q on the right-hand side of (2.15) is related to the heat source and therefore, to the flame and the iron burning exothermic reaction. Furthermore, this term should also include the heat absorbed and released during phase transitions, known as latent heat. For simplicity, we will restrain the model to consider only liquid and austenite phases (2.14a)-(2.14d), then we can write the heat source as

$$q = Q(\boldsymbol{v}) - \rho(\theta) L_l f_l(\theta, l) - \rho(\theta) L_a f_a(\theta, a, l). \tag{2.17}$$

The definition of q includes the term $Q(\boldsymbol{v})$ described already in subsection (2.2.2). The velocity $\boldsymbol{v}$ is a vector which, in this case, has only x as non-zero component as the trajectory of the plate is a straight line along the x axis: $\boldsymbol{v} = (v, 0, 0)^T$. The heat absorbed by the phase transformations is determined by the steel density $\rho(\theta)$ and the latent heat L_i and function f_i of each phase. The functions f_i are specified in equations (2.14a) and (2.14b).

Following Subsection 2.2.3, we add the QSS phase equations for austenite and liquid as they are coupled with the heat equation due to being temperature dependant. These equations with adequate boundary conditions comprise the system of equations (2.18a)-(2.18k). Considering θ_a as the ambient temperature, Newton's cooling law is imposed on the top and bottom of the plate (2.18d)-(2.18e) to describe the exchange of heat with surrounding air with the convection factors h_1 and h_2. The vector $\boldsymbol{n}$ is an outward normal unit vector to the corresponding surface. The temperature of the plate before the process is θ_a and far enough from the torch, the temperature suffers no change. Therefore, a Dirichlet condition is enforced on the plane $\{y = y_{max}\}$ and on the inflow plane $\{x = 0\}$, see equations (2.18f)-(2.18h). Finally, on the symmetry plane $\{y = 0\}$ and on the outflow boundary $\{x = x_{max}\}$, a homogeneous Neumann condition is imposed implicating that there is no heat flux in the normal direction. The values of x_{max} and y_{max} must be chosen sufficiently big, such the influence on the temperature and phase fractions from the artificial boundary conditions is negligible. The boundary conditions

for the phase fractions have already been explained above.

$$\rho(\theta)\, C_p(\theta)\, (\boldsymbol{v}\cdot\nabla\theta) - \nabla\cdot(\kappa(\theta,l)\,\nabla\theta) = q \qquad \text{in } \Omega, \tag{2.18a}$$

$$\boldsymbol{v}\cdot\nabla l = f_l(\theta,l) \qquad \text{in } \Omega, \tag{2.18b}$$

$$\boldsymbol{v}\cdot\nabla a = f_a(\theta,a,l) \qquad \text{in } \Omega, \tag{2.18c}$$

$$-\kappa(\theta,l)\frac{\partial\theta}{\partial\boldsymbol{n}} = h_1(\theta-\theta_a) \quad \text{on } \{z=0\}, \tag{2.18d}$$

$$-\kappa(\theta,l)\frac{\partial\theta}{\partial\boldsymbol{n}} = h_2(\theta-\theta_a) \quad \text{on } \{z=z_{max}\}, \tag{2.18e}$$

$$\theta = \theta_a, \qquad \text{on } \{x=0\} \tag{2.18f}$$

$$\frac{\partial\theta}{\partial\boldsymbol{n}} = 0 \qquad \text{on } \{x=x_{max}\}, \tag{2.18g}$$

$$\theta = \theta_a \qquad \text{on } \{y=y_{max}\}, \tag{2.18h}$$

$$\frac{\partial\theta}{\partial\boldsymbol{n}} = 0 \qquad \text{on } \{y=0\}, \tag{2.18i}$$

$$l = a = 0 \qquad \text{on } \{x=0\} \tag{2.18j}$$

$$\frac{\partial l}{\partial\boldsymbol{n}} = \frac{\partial a}{\partial\boldsymbol{n}} = 0 \qquad \text{on } \partial\Omega\backslash\{x=0\}. \tag{2.18k}$$

2.3 Numerical Approach

The purpose of the model presented is to predict the temperature distribution, the HAZ size in terms of the fraction of austenite and the kerf, i.e., the trail of molten steel produced by flame cutting of a high strength steel plate with 40 mm thickness. We apply the Finite Element Method (FEM) to solve the system (2.18a)-(2.18k) and the requirements for this are detailed in the following.

The material properties required for the model are the density, specific heat capacity and thermal conductivity of the considered Raex® 400 steel grade. These temperature dependant properties were obtained using the commercial software JMatPro® [31], which mainly requires as input the chemical composition of the steel (Table 2.2).

Table 2.2: Chemical composition of Raex® 400 (maximum % of elements). The steel is grain refined.

C	Si	Mn	P	S	Cr	Ni	Mo	B
0.23	0.80	1.70	0.025	0.015	1.50	1	0.50	0.005

After defining the geometric parameters and constants of the model, it is possible to solve the system of equations (2.18a)-(2.18k). This is achieved using the finite element package *pdelib2* [10] developed and maintained at WIAS. The nonlinearities together with the coupling were solved using a fixed-point algorithm and an adaptive mesh module was used to refine the mesh based on a residual-based a posteriori error estimator determining regions with steep gradients for the temperature and phase fractions [5].

As mentioned before, the heat loss due to vanishing thermal conductivity in the kerf is modelled by the mixture ansatz described in (2.16). We found the choice $\delta = 0.01$ a good

compromise yielding both a numerically stable scheme and vanishing heat transport in the kerf.

Note that the phase transition model (2.18b)-(2.18c) represents a system of transport equations and cannot be solved directly using FEM in 3D without encountering erroneous results [32]. The first step taken to deal with this problem is to add artificial diffusivity to the equation. This consists in adding a diffusion term with a coefficient $\varepsilon > 0$.

$$\boldsymbol{v} \cdot \nabla \boldsymbol{\zeta} - \varepsilon \Delta \boldsymbol{\zeta} = f(\theta, \boldsymbol{\zeta}) \tag{2.19}$$

The value of ε must be small enough to avoid too much diffusion but big enough to be effective. For our simulations, we found $\varepsilon = 10^{-8}$ m/s^2 to produce an adequate outcome, but still a further step is required. Equation (2.19) is a steady-state linear scalar convection-diffusion equation with a convection-dominated regime. It is well known that, with this regime, the solutions from FEM contain spurious oscillations. A stabilization method is required. We chose the Streamline-Upwind Petrov-Galerkin (SUPG) method that adds diffusion in the direction of the streamlines [32].

In order to highlight the need for the aforementioned steps to solve appropriately equations (2.18b)-(2.18c) when using FEM in a 3D domain, Figure 2.16 represent the numerical results for the liquid phase in each mentioned step. A temperature distribution in a plate was retrieved after solving the heat equation with a flame cutting. This temperature field was used as input to solve directly the transport equation (2.18b) leading to erratic results (see figure on the left). Then, the result obtained with the addition of artificial diffusivity (2.19) is in the middle of Figure 2.16 while the figure on the right displays the final result with the introduction of the SUPG method.

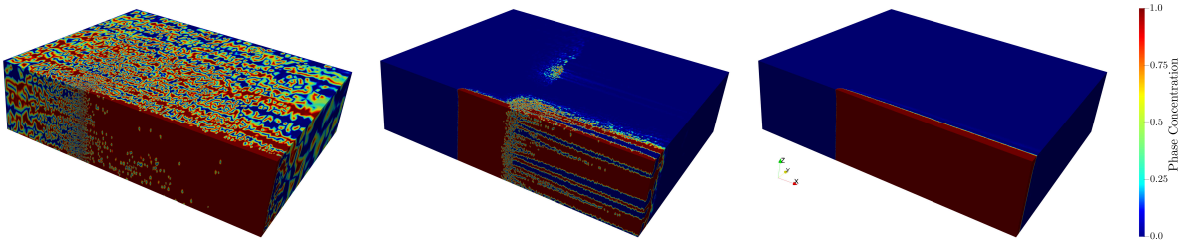

Figure 2.16: Numerical solution of the liquid phase equation with FEM. Left: full convection equation (2.14a), middle: with artificial diffusivity (2.19), right: with artificial diffusivity and SUPG stabilization.

2.4 Results and Validation

Experimental data from two experiments are used to calibrate the volumetric heat source. Both experiments consider a 40 mm Raex® 400 steel plate but different cutting speed: 135 and 270 mm/min. The results comprise isothermal curves in different planes transverse to the cutting direction, see Figure 2.13. In this section, the main results presented belong to the 135 mm/min case as it was used as reference case. Furthermore, the results obtained for 135, 202.5 and 270 mm/min cutting speeds are compared.

From the experimental data, the shape of the 1537 °C isothermal line in Figure 2.13 plus the estimated size of the kerf of 1 mm for the case with a cutting speed of 135 mm/min suggested to use the same values for the volumetric heat source as Thiébaud et al. [3]. These values are $r_1 = 2\,\text{mm}$, $r_2 = r_3 = 1\,\text{mm}$ and $z_1 = z_2 = 2\,\text{mm}$. The power P within Λ was set to 7.35 kW. The size of the computational domain was established to be in accordance with the Dirichlet conditions: $y_{max} = 100\,\text{mm}$ and $x_{max} = 140\,\text{mm}$. The vertical axis of the heat source Λ was located at (40 mm, 0). Heat transfer coefficients h_1 and h_2 were set to $5\,\text{W}/(\text{m}^2\,\text{K})$ and the external temperature θ_a was 25 °C. Regarding the phase equations, the latent heat values were 272 and 16 kJ/kg for liquid and austenite, respectively. The values of τ_l and τ_a representing the transformation speed were 10^{-2} and $5 \times 10^{-1}\,\text{s}$. It was found that is important that τ_l is smaller than τ_a to produce a small interphase region.

2.4.1 Case 135 mm/min

The main focus was on this case as it was used as the reference case. A general view of the temperature distribution around the heat source in the remaining steel is given in Figure 2.17. In this figure, we depict the temperature field in the computational domain where no liquid phase is present, i.e., without the kerf. The features of the heat source Λ can be sensed from the isothermal surfaces with the highest temperature values. As expected, the maximum temperature in the remaining plate is below the melting point (1537 °C).

The corresponding trail of liquid phase (molten steel) and austenite phase produced with the heat source is shown in Figure 2.18. Both phases start approximately at the isothermal surface corresponding to the temperature where the equilibrium volume fraction of each phase is 1, then the phases are transported in the direction of the movement, the x-direction. The trail of liquid is the closest to the cutting plane as expected from the higher temperatures being in this plane. In Figure 2.18, there is a transparent slice of the liquid and austenite volumes such that the inner profile of both phases along the thickness of the plate can be seen. The liquid phase is wider on top while in the middle and bottom it remains the same. On the other hand, the width of austenite is narrower on top while constant along the rest of the thickness.

To understand more clearly the next results, Figure 2.18 also illustrates the location of the straight lines A, B, C and D along which the results where extracted. In Figure 2.19, we can see the phases evolution along lines A (left) and B (right). As A crosses a zone of rapid increase in temperature the austenite phase grows very quickly until the melting point is reached and it decreases while the liquid phase grows. On the other hand, the B line is far enough from the torch and the temperature only causes austenite growth.

As the phases can be identified with the kerf and the Heat affected zone (HAZ), respectively, we can retrieve the width of both areas with line D. This is presented in Figure 2.20. On the transverse plane to the cutting direction we find the liquid phase, then a very small two-phase region and finally the remaining plate with the austenitized and the non-affected area. On the left-hand side the result is shown with the heat losses due to vanishing heat diffusion in the kerf. The right-hand side depicts the result with heat diffusion in the kerf (i.e., $\delta = 1$ in (2.16)) leading to a wider HAZ as expected. A further comparison of kerf and HAZ cross-section in the case with (left) and without heat losses in the kerf (right) is shown in Figure 2.21.

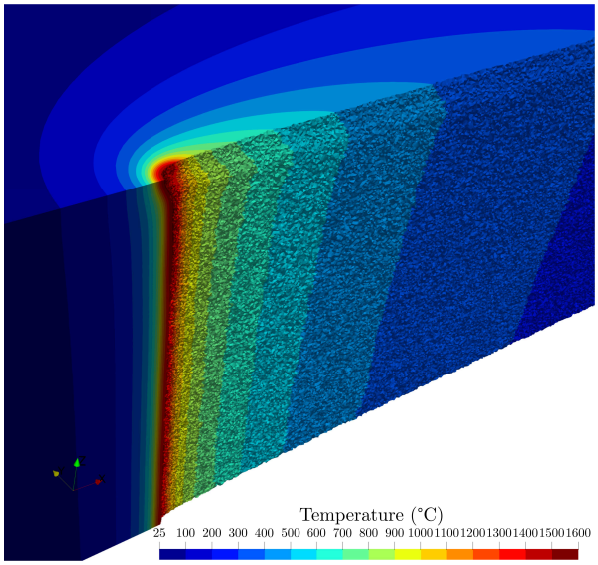

Figure 2.17: Temperature distribution around the heat source location. Case 135 mm/min.

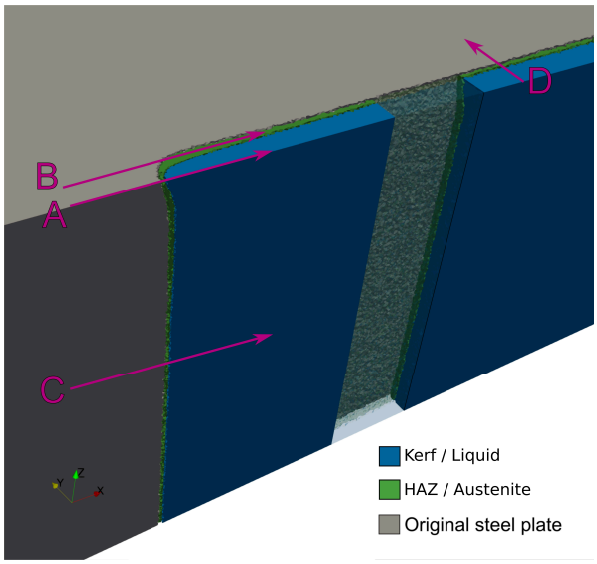

Figure 2.18: Trail of liquid phase (blue) and austenite (green) after flame cutting. Case 135 mm/min.

In the remaining plate, a rapid increase in temperature and the cooling afterwards can be observed in Figure 2.22. We track the temperature on the top (left) and middle (right) of the plate using lines A and C. Moreover, these lines are shifted in the y-direction to obtain more information about temperatures reached in the remaining plate. As shown in Figure 2.17, the maximum temperature is reached on the top of the plate. The curves closest to the cutting line vanish as the position corresponds to the liquid phase region.

2.4.2 Case 202.5 and 270 mm/min

To see the effect of different cutting speeds we multiplied the base speed 135 mm/min, by a factor 1.5 and 2, resulting in 202.5 and 270 mm/min. As it is explained in the model, the velocity $\boldsymbol{v}$ affects the volume Λ where the heat source is defined. Specifically, the speed affects the value of $C(\boldsymbol{v})$ which scales the radii of Λ with speed (cf. (2.5)). The function $C(\boldsymbol{v})$ is

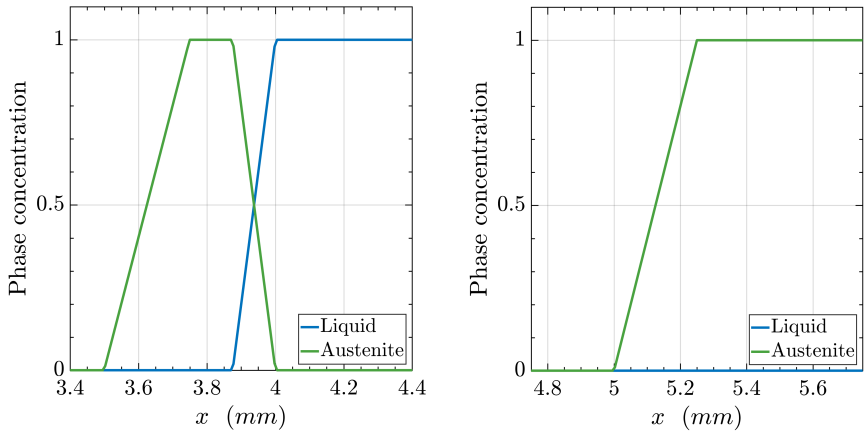

Figure 2.19: Evolution of phases along lines A (left) and B (right).

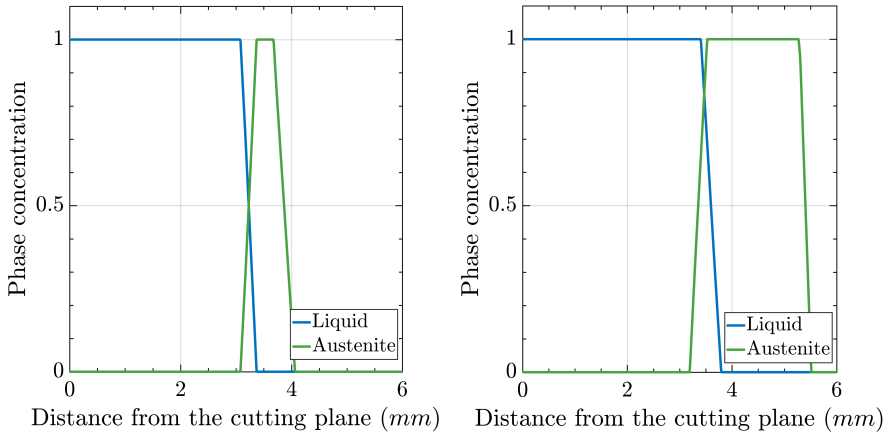

Figure 2.20: Liquid and austenite phases along line D. Left, with consideration of heat losses in the kerf, right without.

assumed to be linear and monotonically decreasing. More precisely, for the base case, we choose $C(135) = 1$, while $C(202.5) = 0.75$ and $C(270) = 0.5$.

The features of the results obtained with faster velocities are the same qualitatively. Quantitatively, with higher speed, the influence area of the torch and the temperature distribution produce a smaller kerf and HAZ. In Table 2.3, the average values of kerf and HAZ width for the three cases are shown. Table 2.3 provides a good insight of the trends: smaller region width with increasing speed and greater values for the kerf on the top than in the middle and at the bottom of the plate.

Table 2.3: Kerf and heat affected zone (HAZ) width after flame cutting on the top, middle and bottom of the plate for different velocities.

	Kerf width (mm)		HAZ width (mm)	
	Top	Middle and bottom	Top	Middle and bottom
135 mm/min	3.01	1.95	0.30	0.64
202.5 mm/min	2.28	1.50	0.42	0.56
270 mm/min	1.93	1.25	0.42	0.53

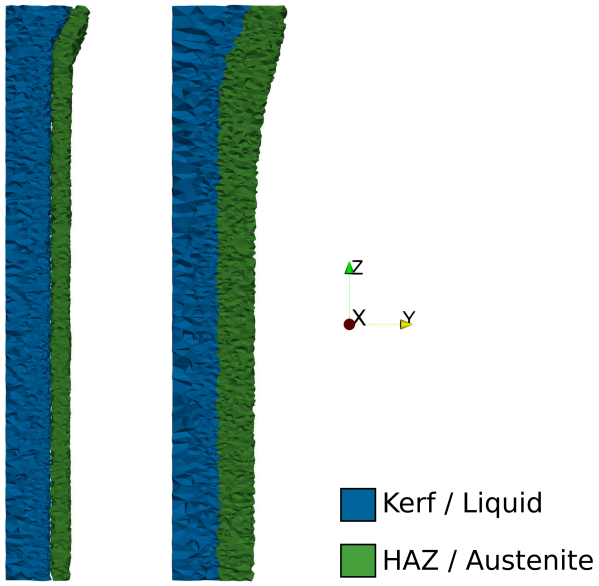

Figure 2.21: Comparison of the liquid and HAZ profiles with and without considering heat losses in the kerf. Left with, right without.

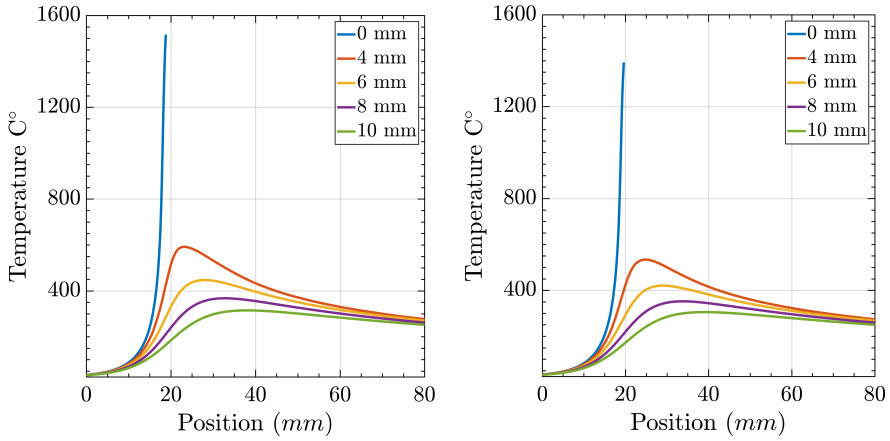

Figure 2.22: Evolution of nodal temperature from numerical simulation along lines A (left) and C (right). Lines A and C were shifted to distances of 2, 4, 6 and 8 mm from the cutting plane.

As the kerf width is known after the numerical simulation, we can focus on the remaining plate. In Figure 2.23, the temperature fields in the transverse plane to the cutting direction for the three cases are aligned to the resulting cutting edge. Thus, we can observe the difference in the temperature reached within the plate. As expected, with slower speed higher temperatures reach further into the plate.

2.5 Conclusions

Two different approaches are possible for consideration of removal of material during the simulation [23, 2], either the domain starts in the cutting plane (torch position) or in the cutting edge (resultant edge after cutting). In Thiébaud et al. [3] a mix of both options is used as the domain includes a predefined kerf for the area already affected by the flame. In this work, the domain starts in the cutting plane allowing us to describe the kerf size as the liquid phase created during flame cutting instead of predefining it. The heat losses occurring

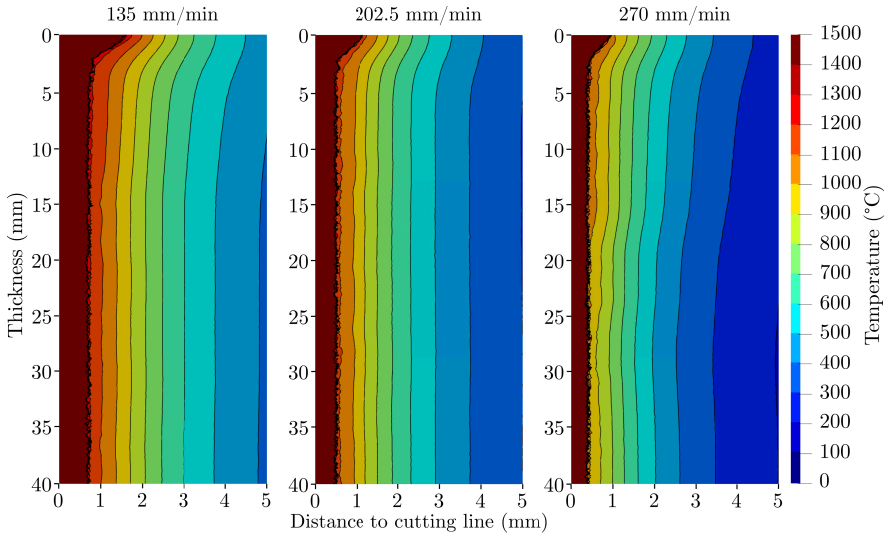

Figure 2.23: Isothermal contours in the remaining plate for different velocities.

in the kerf were identified as noteworthy in [3]. Thus, we consider them by reducing the thermal conductivity in the liquid region. We are convinced that this approach helps achieving more realistic values in the remaining plate. The disagreement between numerical results and experimental data is higher in the surface area (compare Figs. 2.13 and 2.23). More heat should be spread in the y-direction. In practice, this effect is caused by a deflection of the flame on top of the plate. A more complex definition of the heat source in Bae et al. [23] or [27] may provide more realistic results. For example in [23], it is divided into three terms, one of them is a Gaussian function which is only defined in the upper surface of the plate and may help balancing the temperatures obtained numerically, producing less heat in the cutting line but more into the width of the plate as should be expected according to experimental data. Thiébaud et al. and Jokiaho et al. [3, 2] get similar temperature profiles to the ones displayed in Figure 2.22. The total power required by Thiébaud et al. is 18.8 kW, which is higher than the one estimated in this study, 7.35 kW. This difference is mostly related to the different treatment of the kerf as explained before. The inclusion of quasi-stationary phases transition models for liquid and austenite in the present work provides a new tool for a deeper understanding of the flame cutting process. The liquid phase fraction allows for a rather precise description of the kerf while the austenite fraction does the same for the heat affected zone. The trend found of decreasing width of the HAZ with increasing speed (Table 2.3) is also observed in experimental results in Jokiaho et al. [26]. In their experiments the HAZ is assumed to be formed by a martensitic region, a two phase region and a tempered region. The width of the HAZ on the top of the plate is thinner than in the rest of the plate. This feature is inconsistent with experimental results [3, 23]. The reason for this is a thickening of the kerf close to the surface and accordingly less heat to create a wider HAZ close to the surface. However, this could be changed by changing the heat source which has been defined to match data from a different source. In order to mitigate the danger of cold cracks, preheating has been mentioned as an effective method. The model developed can be used in combination with preheating to study in detail the temperature during the whole process. In the following Chapter 3, a novel technique for induction preheating of the steel is presented and modelled.

Later, the optimal control of the preheating for the flame cutting process is discussed in Chapter 4.

3

Induction preheating of steel plates

Preheating of steel plates prior to thermal cutting is a standard practice. A common method to preheat the plates uniformly is to put on hold each plate in an oven for several minutes until a temperature in the range of 100 to 200 °C is achieved. In this chapter, induction heating will be considered as the preheating technique. A 3D-thermoelectric model for the induction preheating is presented. Results achieved with computer simulations are shown and are compared with experimental data. The final goal of the preheating is to achieve a homogeneous temperature along thickness in the cutting line just before the use of the flame cutting torch.

Outline. First, in Section 3.1, the process of induction heating is presented and proposed as an alternative for preheating of steel plates for flame cutting. Section 3.2 describes a mathematical model for induction preheating of steel plates. It consists of the coupling of the eddy currents model in the harmonic regime with the QSS heat equation. Section 3.3 details the setting used for simulations using FEM to test the feasibility of induction preheating. The results for two different cutting speeds are compared in Section 3.4. Experimental validation of the model is shown in Section 3.5. In Section 3.6, the experience obtained from the simulations is used to develop a simplified model of the distribution of the dissipated power on the plate. Finally, concluding remarks are noted in Section 3.7.

3.1 Motivation

Induction hardening is one of the common methods to heat treat steels. The heat is generated by induced electric currents. The principle is the following: a coil (inductor) that is connected to an alternating current source (converter) generates a periodically changing electromagnetic field. The temporal changing magnetic flux induces a current in the workpiece (conductor) that is close to the induction coil. Due to the resistance of the workpiece, some part of the power is transformed into eddy current losses which result into heating of the workpiece (Joule heating) [33, 34].

The distribution of the heat in the workpiece is complex. It depends on the magnetic fields created by the inductor and the induced currents in the conductor. These fields are determined by different factors such as the shape of inductor and conductor, the electrical current or material properties. Nonetheless, a constant feature of induction heating is known as *skin effect*. This effect consists in the eddy currents being concentrated in the surface layer of the workpiece.

The penetration or skin depth of the electric current is defined as the depth δ at which the current density falls to $1/e$ ($\sim$37 %) of its maximum value found near the surface, [35, 34]. The penetration depth depends on the electric and magnetic properties of the workpiece, but mainly on the frequency of the alternating current.

As stated before, the aspiration of this work is to introduce induction preheating to the flame cutting setting laid out in Chapter 2. Unlike the widely known induction hardening, which requires usually between 800 and 900 °C, the preheating temperature should be between 100 and 200 °C. The proposed induction preheating process comprises a steel plate (conductor) which is moving following a straight trajectory. This trajectory will be referred to as *cutting line*. A fixed copper coil (inductor) is positioned above the steel plate. As it is traversed by a electrical current, it will induce currents on the plate and, as a result, heat will be generated in the steel by the Joule effect.

To reduce the number of options for position and shape of the induction coil, it is important to recall the objective of the preheating. First, for energy efficiency, the preheating should impact only the heat affected zone (HAZ) which is created by flame cutting. As seen in Chapter 2, the HAZ is created around the cutting line, in the cutting edge of the remaining halves (see Figure 2.18). Therefore, the coil should be located at the cutting line. Conveniently, in order to produce the same effect in both resultant halves of the plate, the coil should have planar symmetry in the cutting plane.

Secondly, an industrial requirement of the preheating is to achieve uniform temperature along the thickness of the plate. Due to the symmetry of the plate, the most direct approach would be to apply heat from both sides of the plate, top and bottom. Unfortunately, the industrial setting modelled in Chapter 2 does not allow to introduce an extra coil heating from the bottom.

Considering one single coil on top of the cutting line, the skin effect causes the heat to be focused on the top surface of the workpiece. The heat requires some time to effectively reach the bottom due to conduction. Consequently, the coil should be at some distance from the torch so temperature uniformity is achieved.

Following the design of an induction heating device available for experimental validation, a U-shaped coil is considered for the induction preheating as portrayed in Figure 3.1. The longest side of the coil stays some millimetres over the cutting line providing heat in the area directly below it.

3.2 Model

The mathematical model consists of the coupling of a quasi-stationary heating model and a harmonic regime electromagnetic model. The electromagnetic problem must be solved

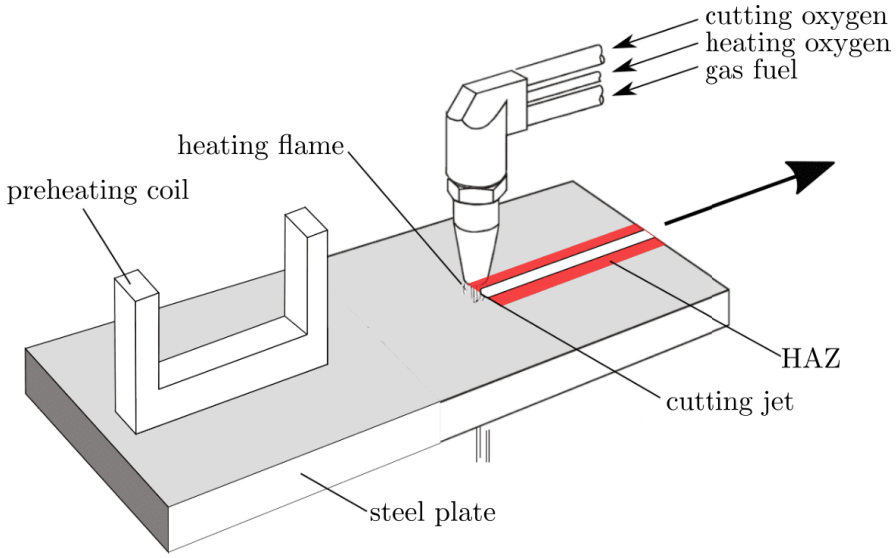

Figure 3.1: Scheme of flame cutting of a moving steel plate with an induction preheating coil.

throughout the complete domain: plate, coil and surrounding air but the heat equation only applies to the steel plate. Temperature dependent properties of the steel are considered and therefore, nonlinearities must be taken into account. Moreover, the magnetic permeability does not only depend on temperature but also on the magnetic field intensity, affecting the skin depth and distribution of the dissipated power in the plate.

The preheating occurs in the same line where the flame cutting takes place. Therefore, the steel plate moves following the previous trajectory with the speed chosen for cutting speed. The coil located at some millimetres over the cutting line induce currents on the steel which, by the Joule effect, generate heat in it.

3.2.1 Electromagnetic model

The electromagnetic model is obtained from Maxwell's equations and allows the modelling of electromagnetic fields on each point of the workpiece. Thus, the Joule effect can be obtained and can be used as the source term of the thermal problem presented in the next section. Since Maxwell's equations are defined throughout the space, with the aim of using the finite element method, it is necessary to consider air around the conductive parts and establish appropriate boundary conditions far enough from the area where the fields are concentrated. Thus, the computational domain comprises the steel plate Ω, coil Ω_{c1}, concentrator Ω_{c2} and surrounding air Ω_{air} (all four define Ω_T). A representation of the sets can be seen in Figure 3.2. Magnetic flux concentrators are high-permeability soft-magnetic materials with low electrical conductivity that provide more efficiency to induction heating by redirecting the magnetic field towards the workpiece [34]. As the coil is located on top of the cutting line, it can be assumed that a planar symmetry exists and only half of the domain is necessary to be modelled.

The study of electromagnetic phenomena is derived from Maxwell's equations, which are (3.1a) through (3.1d) where the fields are defined in all $\mathbb{R}^3$ and depend on position and time

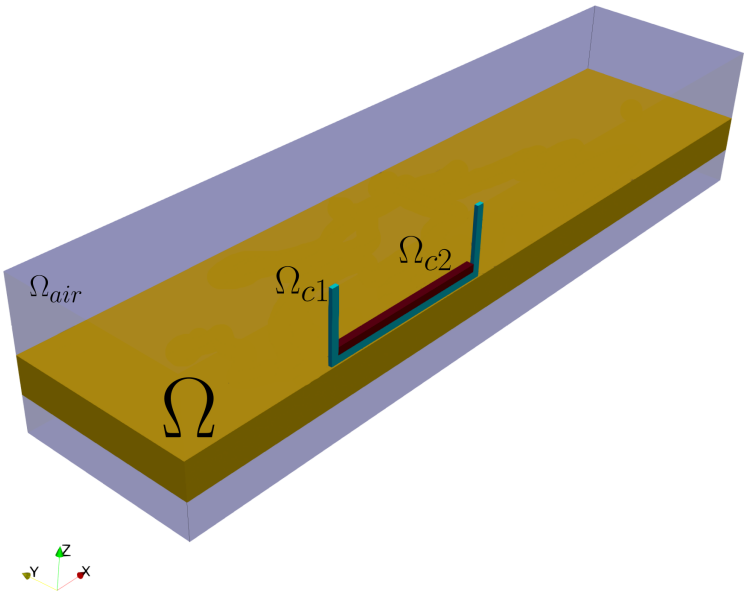

Figure 3.2: Domains for the induction preheating model.

(see [35]):

$$\frac{\partial \mathbf{B}}{\partial t} + \operatorname{curl} \mathbf{E} = \mathbf{0}, \tag{3.1a}$$

$$\operatorname{curl} \mathbf{H} = \mathbf{J} + \frac{\partial \mathbf{D}}{\partial t}, \tag{3.1b}$$

$$\operatorname{div} \mathbf{B} = 0, \tag{3.1c}$$

$$\operatorname{div} \mathbf{D} = \rho_V, \tag{3.1d}$$

$$\mathbf{B} = \mu \mathbf{H}, \tag{3.1e}$$

$$\mathbf{D} = \epsilon \mathbf{E}, \tag{3.1f}$$

$$\mathbf{J} = \sigma \mathbf{E}, \tag{3.1g}$$

where $\mathbf{E}$ is the electric field [V/m], $\mathbf{H}$ the magnetic field intensity [A/m], $\mathbf{B}$ the magnetic flux density [Wb/m^2], $\mathbf{D}$ the electric displacement [C/m^2] and $\mathbf{J}$ the current density [A/m^2]. These equations are completed with the constitutive laws (3.1e, 3.1f, 3.1g) describing the magnetic and electric behaviour of different materials. These are detailed below assuming that they all have an isotropic behaviour.

The Ohm's law (3.1g) relates the current density with the electric field. Here, σ denotes the electrical conductivity [A/(Vm)] which is positive in the conductors and null on non-conductive materials; while constant in the coil and concentrator, σ depends on the temperature θ in the steel. We define σ accordingly as

$$\sigma(\boldsymbol{x}, \theta) = \begin{cases} 0, & \boldsymbol{x} \in \Omega_{air} \\ \sigma_{c1}, & \boldsymbol{x} \in \Omega_{c1} \\ \sigma_{c2}, & \boldsymbol{x} \in \Omega_{c2} \\ \bar{\sigma}(\theta), & \boldsymbol{x} \in \Omega. \end{cases} \tag{3.2}$$

The constitutive law of the electric displacement $\mathbf{D}$ (3.1f) contains the electrical permittivity ϵ [F/m].

Since the steel of the plates is a ferromagnetic material, a nonlinear relationship is considered between the magnetic field and the magnetic flux density (3.1e); specifically,

$$\mathbf{B} = \mu(\mathbf{H}, \theta)\mathbf{H} = \boldsymbol{\mathcal{F}}(|\mathbf{H}|, \theta), \quad \text{in} \quad \Omega, \tag{3.3}$$

where μ is the magnetic permeability [H/m] which depends on $|\mathbf{H}|$ and on the temperature θ of the workpiece. Moreover, the copper of the coil is a non-magnetic material so that in the material, as in the air, we have the relationship

$$\mathbf{B} = \mu_0 \mathbf{H}, \tag{3.4}$$

with μ_0 being the vacuum permeability ($4\pi \cdot 10^{-7}$ H/m). In the remaining concentrator, the magnetic permeability of vacuum is multiplied by the relative magnetic permeability μ_{c2} of the material:

$$\mathbf{B} = \mu_0 \mu_{c2} \mathbf{H}, \quad \text{in} \quad \Omega_{c2}. \tag{3.5}$$

The full definition of μ is

$$\mu(\boldsymbol{x}, \theta, \mathbf{H}) = \begin{cases} \mu_0, & \boldsymbol{x} \in \Omega_{air} \cup \Omega_{c1} \\ \mu_0 \mu_{c2}, & \boldsymbol{x} \in \Omega_{c2} \\ \mu_0 \frac{\boldsymbol{\mathcal{F}}(|\mathbf{H}|, \theta)}{|\mathbf{H}|}, & \boldsymbol{x} \in \Omega. \end{cases} \tag{3.6}$$

The induction heating device proposed works at low frequency regime, therefore, the electric displacement in the Ampere's law (3.1b) in Maxwell's equations (3.1) can be neglected. The resulting model is known as eddy currents model:

$$\frac{\partial \mathbf{B}}{\partial t} + \operatorname{curl} \mathbf{E} = \mathbf{0}, \tag{3.7a}$$

$$\operatorname{curl} \mathbf{H} = \mathbf{J}, \tag{3.7b}$$

$$\operatorname{div} \mathbf{B} = 0, \tag{3.7c}$$

$$\operatorname{div} \mathbf{D} = \rho_V, \tag{3.7d}$$

$$\mathbf{B} = \mu \mathbf{H}, \tag{3.7e}$$

$$\mathbf{D} = \epsilon \mathbf{E}, \tag{3.7f}$$

$$\mathbf{J} = \sigma \mathbf{E}. \tag{3.7g}$$

Notice that there is a coupling between the magnetic and the electric field only in conductive regions ($\sigma \neq 0$), thus, the dielectric displacement $\mathbf{D}$ has no influence on the description of the eddy currents. We do not keep the Gauss' law for electric charge (3.7d) nor the constitutive law (3.7f). Instead, we retrieve from (3.7b) and (3.7g) that

$$\operatorname{div}(\sigma \boldsymbol{\mathcal{E}}) = 0 \quad \text{in the conductors.} \tag{3.8}$$

The model (3.7) is a partial differential equations transient problem. Taking into account that the current source used in the industrial process is of sinusoidal type, if the behaviour of the material was linear, the system (3.7) could be solved equivalently in harmonic regime (all fields would be sinusoidal). However, the nonlinearity in the magnetic behaviour requires to

solve a genuine transitory problem; this implies to approximate the solution until a steady state is reached, which requires very long computing time. Therefore, a solution common in the literature [36] is to solve the nonlinear problem in harmonic regime and this is the solution adopted in this work. The harmonic regime is based on the assumption that the fields on the Maxwell's equations are of the form:

$$\mathbf{G}(\boldsymbol{x}, t) = \mathrm{Re}(e^{i\omega t}\boldsymbol{\mathcal{G}}(\boldsymbol{x})), \tag{3.9}$$

where $\boldsymbol{\mathcal{G}}(\boldsymbol{x})$ is a complex field that depends only on the spatial variable $\boldsymbol{x}$ and is called the complex amplitude (or phasor) of $\mathbf{G}$; $\omega = 2\pi f$, is the angular frequency and f is the frequency of the current [Hz].

By replacing in (3.7) we obtain the electromagnetic Helmholtz's equations for the complex phasors $\boldsymbol{\mathcal{B}}$, $\boldsymbol{\mathcal{H}}$, $\boldsymbol{\mathcal{E}}$ and $\boldsymbol{\mathcal{J}}$:

$$i\omega\boldsymbol{\mathcal{B}} + \operatorname{curl}\boldsymbol{\mathcal{E}} = \mathbf{0}, \tag{3.10a}$$

$$\operatorname{curl}\boldsymbol{\mathcal{H}} = \boldsymbol{\mathcal{J}}, \tag{3.10b}$$

$$\operatorname{div}\boldsymbol{\mathcal{B}} = 0, \tag{3.10c}$$

$$\boldsymbol{\mathcal{B}} = \mu\boldsymbol{\mathcal{H}}, \tag{3.10d}$$

$$\boldsymbol{\mathcal{J}} = \sigma\boldsymbol{\mathcal{E}}. \tag{3.10e}$$

Under this setting, it is convenient to reformulate the electromagnetic problem in terms of the magnetic vector potential and the scalar electric potential. It allows to reduce the system consisting of four partial differential equations plus constitutive laws. This formulation is based on the relations $\operatorname{curl}\nabla f = 0$ and $\operatorname{div}\operatorname{curl} g = 0$ where f and g are scalar and vector valued functions respectively. Specifically, from Equation (3.10c), it can be deduced that a magnetic vector potential $\boldsymbol{\mathcal{A}}$ [Wb/m] exists, such that

$$\operatorname{curl}\boldsymbol{\mathcal{A}} = \boldsymbol{\mathcal{B}}. \tag{3.11}$$

The vector field $\boldsymbol{\mathcal{A}}$ is not unique. In fact, $\operatorname{curl}(\boldsymbol{\mathcal{A}} + \nabla V) = \boldsymbol{\mathcal{B}}$ for all scalar field V. In order to ensure uniqueness, a so-called *gauge condition* should be added. A common choice is the *Coulomb gauge*:

$$\operatorname{div}\boldsymbol{\mathcal{A}} = 0. \tag{3.12}$$

Using (3.10a), it holds

$$\operatorname{curl}(i\omega\boldsymbol{\mathcal{A}} + \boldsymbol{\mathcal{E}}) = \mathbf{0}. \tag{3.13}$$

As a consequence, we have the existence of the electric scalar potential V [V] such that

$$i\omega\boldsymbol{\mathcal{A}} + \boldsymbol{\mathcal{E}} = -\nabla V \quad \text{in} \quad \Omega_T. \tag{3.14}$$

From (3.10b), (3.10d), (3.10e) and (3.14) we deduce:

$$\operatorname{curl}\left(\frac{1}{\mu}\operatorname{curl}\boldsymbol{\mathcal{A}}\right) = -i\omega\sigma\boldsymbol{\mathcal{A}} - \sigma\nabla V \quad \text{in} \quad \Omega_T. \tag{3.15}$$

Equation (3.15) is defined in the whole domain Ω_T. It is interesting to make a more detailed description of the equation by using the subsets of Ω_T and the values taken by the current density [37].

First, combining (3.14) with the Ohm's law (3.10e) the following expression for the current density $\boldsymbol{\mathcal{J}}$ is obtained:

$$\boldsymbol{\mathcal{J}} = -i\omega\sigma\boldsymbol{\mathcal{A}} - \sigma\nabla V. \tag{3.16}$$

The current density can be thought of as consisting of two components: an impressed part $\boldsymbol{\mathcal{J}}_{\text{source}}$ and an induced part $\boldsymbol{\mathcal{J}}_{\text{eddy}}$.

The impressed part is due to the external source connected to the coil Ω_{c1} and is defined by the gradient of the scalar potential. The induced part is due to the time-varying B field in the coil itself [37]. Even though the conductivity of the concentrator is much lower than that of the coil, we do not disregard it. For this reason, we use the coil-concentrator set denoted as $\Omega_c = \Omega_{c1} \cup \Omega_{c2}$. Therefore, in the coil-concentrator,

$$\operatorname{curl}\left(\frac{1}{\mu}\operatorname{curl}\boldsymbol{\mathcal{A}}\right) + i\omega\sigma\boldsymbol{\mathcal{A}} = \boldsymbol{\mathcal{J}}_{\text{source}} \quad \text{in} \quad \Omega_c, \tag{3.17}$$

where

$$\boldsymbol{\mathcal{J}}_{\text{source}} = -\sigma\nabla V. \tag{3.18}$$

In the steel plate the induced current density lies but there is no source term. Consequently, (3.15) takes the form

$$\operatorname{curl}\left(\frac{1}{\mu}\operatorname{curl}\boldsymbol{\mathcal{A}}\right) + i\omega\bar{\sigma}(\theta)\boldsymbol{\mathcal{A}} = 0 \quad \text{in} \quad \Omega, \tag{3.19}$$

with

$$\boldsymbol{\mathcal{J}}_{\text{eddy}} = -i\omega\bar{\sigma}(\theta)\boldsymbol{\mathcal{A}}. \tag{3.20}$$

There electric conductivity σ in the air is null, and so (3.15) simplifies to

$$\operatorname{curl}\left(\frac{1}{\mu}\operatorname{curl}\boldsymbol{\mathcal{A}}\right) = 0 \quad \text{in} \quad \Omega_{air}. \tag{3.21}$$

This definition by subsets in the transient regime can be found in [38].

Recalling the condition (3.8) on $\boldsymbol{\mathcal{E}}$ for the conductors, we demand that also for the current it holds

$$\operatorname{div}\sigma\nabla V = 0 \quad \text{in} \quad \Omega_c. \tag{3.22}$$

The electrical current is defined only on the coil-concentrator Ω_c. This way, the electric scalar potential V disappears elsewhere.

Boundary conditions are necessary to complete the obtained system. They can be derived for the system (3.1) with the Gauss' and Stoke's theorems and then adjusted for the vector potential formulation [35, 33].

$$\operatorname{curl}\left(\frac{1}{\mu}\operatorname{curl}\boldsymbol{\mathcal{A}}\right)+i\omega\sigma\boldsymbol{\mathcal{A}}=-\sigma\nabla V,\ \text{in}\quad\Omega_c, \tag{3.23a}$$

$$\operatorname{curl}\left(\frac{1}{\mu}\operatorname{curl}\boldsymbol{\mathcal{A}}\right)+i\omega\bar{\sigma}(\theta)\boldsymbol{\mathcal{A}}=0,\qquad\text{in}\quad\Omega, \tag{3.23b}$$

$$\operatorname{curl}\left(\frac{1}{\mu}\operatorname{curl}\boldsymbol{\mathcal{A}}\right)=0,\qquad\text{in}\quad\Omega_{air}, \tag{3.23c}$$

$$\operatorname{div}\sigma\nabla V=0,\qquad\text{in}\quad\Omega_c, \tag{3.23d}$$

$$\boldsymbol{\mathcal{A}}\times\boldsymbol{n}=0,\qquad\text{on}\quad\partial\Omega_T, \tag{3.23e}$$

$$\sigma\nabla V\cdot\boldsymbol{n}=0,\qquad\text{on}\quad\partial\Omega_T. \tag{3.23f}$$

The system (3.23) is still incomplete as there is no description of the electrical current or voltage. With the current setting the most direct option is to define it as a potential difference between the two ends of the inductor (inflow Γ_{in}/outflow Γ_{out}). This is done by means of a jump condition on the potential V:

$$[\![V]\!]=V_0\quad\text{on}\quad\Gamma_{in}, \tag{3.24}$$

where $[\![\cdot]\!]$ denotes the jump of a quantity across Γ_{in} and V_0 denotes the voltage.

To simulate the induction heating process is necessary to couple the previous model with a heat transfer model. As it has been advanced over the chapter, the following coupling exists: the heat source of the thermal model depends on the solution of the electromagnetic problem while, in the electromagnetic problem, the properties σ and μ depend on the temperature in the steel. Next the thermal model to be solved is presented.

3.2.2 Thermal model

The mathematical model consists of the coupling of a quasi-stationary heating model and a harmonic regime electromagnetic model. Although the electromagnetic problem must be solved throughout the complete domain Ω_T, the heat equation only applies to the steel plate Ω.

We would like to add induction preheating to the current setting of flame cutting. Therefore, the hypotheses to consider the quasi-stationary state (QSS) presented in Chapter 2 are still valid. Therefore, the objective is to identify the stationary state distribution of temperature in the steel plate taking into account the movement of it. Like the previous model, to consider the movement of the steel plate, a velocity term is included into the classic heat equation. Thanks to the Joule effect, the area of the plate passing below the coil is heated by the electromagnetic field generated. The heat obtained by Joule effect, concentrated on the surface of the billet, is transferred to the bottom of the workpiece by conduction. The classic heat transfer equation in quasi-stationary regime to model this process can be written in the form:

$$\rho\left(\theta\right)C_p\left(\theta\right)\left(\boldsymbol{v}\cdot\nabla\theta\right)-\operatorname{div}\left(\kappa\left(\theta\right)\nabla\theta\right)=\frac{\bar{\sigma}(\theta)\omega^2}{2}|\boldsymbol{\mathcal{A}}|^2\quad\text{in}\quad\Omega, \tag{3.25}$$

where θ is the temperature [°C], κ the thermal conductivity [W/(mK)], ρ the density [kg/m^3], C_p the specific heat [J/K] and $\bar{\sigma}$ the electrical conductivity [A/(Vm)]. Note that these properties are temperature dependent. Moreover, the heat source is the Joule effect from the electromagnetic field and is determined by the current density $\boldsymbol{\mathcal{J}}$ in the workpiece as the average in a cycle (see for example [39]). For simplicity, we use an equivalent expression based on the magnetic vector potential $\boldsymbol{\mathcal{A}}$.

Equation (3.25) is completed with the boundary conditions

$$-\kappa(\theta)\frac{\partial\theta}{\partial\boldsymbol{n}} = h(\theta-\theta_a) \text{ on } \{z=0\}\cup\{z=z_{max}\}, \tag{3.26a}$$

$$-\kappa(\theta)\frac{\partial\theta}{\partial\boldsymbol{n}} = 0 \quad \text{on } \{x=x_{max}\}\cup\{y=0\}, \tag{3.26b}$$

$$\theta = \theta_a \quad \text{on } \{x=0\}\cup\{y=y_{max}\}. \tag{3.26c}$$

Three types of boundary conditions are considered for the surfaces of the plate: Neumann boundary condition for the heat losses due to convection (3.26a), homogeneous Neumann boundary condition to block the flux of heat (3.26b) and Dirichlet boundary condition for the faces not affected by the heat (3.26c). This way, h is the coefficient of heat exchange by convection and θ_a the external temperature of convection (i.e., the temperature of the air surrounding the workpiece).

Radiation losses are not considered as they are estimated to be negligible with the maximum temperature by preheating being not greater than 200 °C.

3.2.3 Complete model

The combination of the quasi-stationary heat equation (3.25) with the time-harmonic Maxwell's equations in vector potential formulation (3.23) are together in the following system of equations:

$$\operatorname{curl}\left(\frac{1}{\mu}\operatorname{curl}\boldsymbol{\mathcal{A}}\right)+i\omega\sigma\boldsymbol{\mathcal{A}} = -\sigma\nabla V, \quad \text{in } \Omega_c, \tag{3.27a}$$

$$\operatorname{curl}\left(\frac{1}{\mu(\theta)}\operatorname{curl}\boldsymbol{\mathcal{A}}\right)+i\omega\bar{\sigma}(\theta)\boldsymbol{\mathcal{A}} = 0, \quad \text{in } \Omega, \tag{3.27b}$$

$$\operatorname{curl}\left(\frac{1}{\mu}\operatorname{curl}\boldsymbol{\mathcal{A}}\right) = 0, \quad \text{in } \Omega_{air}, \tag{3.27c}$$

$$\operatorname{div}\sigma\nabla V = 0, \quad \text{in } \Omega_{c1}, \tag{3.27d}$$

$$\rho(\theta)C_p(\theta)(\boldsymbol{v}\cdot\nabla\theta)-\operatorname{div}(\kappa(\theta)\nabla\theta) = \frac{\bar{\sigma}(\theta)\omega^2}{2}|\boldsymbol{\mathcal{A}}|^2, \text{ in } \Omega, \tag{3.27e}$$

$$\boldsymbol{\mathcal{A}}\times\boldsymbol{n} = 0, \quad \text{on } \partial\Omega_T, \tag{3.27f}$$

$$\sigma\nabla V\cdot\boldsymbol{n} = 0, \quad \text{on } \partial\Omega_T, \tag{3.27g}$$

$$[\![V]\!] = V_0, \quad \text{on } \Gamma_{in}, \tag{3.27h}$$

$$-\kappa(\theta)\frac{\partial\theta}{\partial\boldsymbol{n}} = h(\theta-\theta_a), \quad \text{on } \{z=0\}\cup\{z=z_{max}\}, \tag{3.27i}$$

$$-\kappa(\theta)\frac{\partial\theta}{\partial\boldsymbol{n}} = 0, \quad \text{on } \{x=x_{max}\}\cup\{y=0\}, \tag{3.27j}$$

$$\theta = \theta_a, \quad \text{on } \{x=0\}\cup\{y=y_{max}\}. \tag{3.27k}$$

Summarizing, the problem to be solved reads as follows: *Given a voltage difference of* V_0 *between the two ends of* Ω_{c1} *find a vector field* $\boldsymbol{\mathcal{A}}$ *defined in* Ω_T*, and a scalar field* V *defined in* Ω_c *such that the system* (3.27) *is fulfilled.*

3.3 Simulation data: geometry, materials and process parameters

In the following, the complete model presented in Subsection 3.2.3 is solved with the finite elements method (FEM). The simulations were carried out using the FEM package *pdelib* developed in WIAS. The heat equation was solved only in the plate using P1 elements. On the other hand, the electromagnetics were solved in the whole computational domain using Nédélec edge elements [40] as P1 elements could lead to spurious solutions [35]. The FEM package was used in a similar induction heating 3D setting in [41, 5]. Mesh adaptivity was used to increase the number of elements where eddy currents are located. This is fundamental to consider the skin effect appropriately. All the necessary data regarding geometry, material and process parameters are presented and used to solve the model.

The computational domain represents a possible disposition of steel plate and coil for the preheating process. The whole domain comprises the four subdomains from Figure 3.2: steel plate, coil, concentrator and air. Only the plate or the set plate-coil-concentrator will be visually represented from now on. A triangulation of the domain is shown in Figure 3.3.

As the geometry has a planar symmetry through the cutting line, for the simulations, only half of the geometry from Figure 3.3 is considered to reduce computational time. This domain can be seen in Figure 3.4 and geometry data is compiled in Table 3.1.

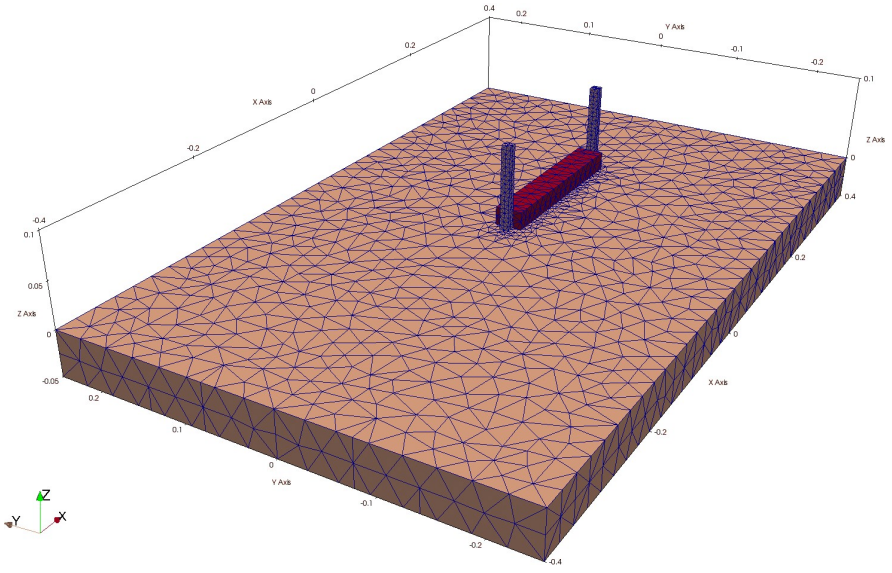

Figure 3.3: Steel plate, coil and concentrator disposition.

The materials used as well as the electromagnetic properties considered are collected in Table 3.2. Steel 34CrMo4 was selected for the simulation as all properties data needed were available. The properties were extracted from [33] and can be observed in Figure 3.5. For the induction coil, copper is chosen as it is commonly used. For the concentrator, Fluxtrol 50 is considered. This material is manufactured by the company Fluxtrol, Inc. and its properties

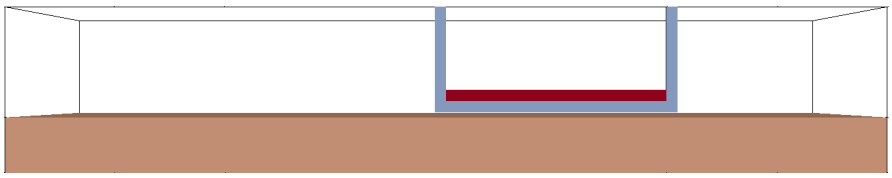

Figure 3.4: View of the computational domain from the symmetry plane.

Table 3.1: Geometry data used in the simulation.

Plate thickness	50 mm
Plate width	500 mm
Plate length	800 mm
Coil width	10 mm
Coil height	95 mm
Coil length	220 mm
Air gap between coil and plate	5 mm
Concentrator width	10 mm

can be found in [42]. The length of the coil was chosen to be similar to that of the device used for experimental validation in Section 3.5. The concentrator disposition around the coil is standard to improve the efficiency of induction heating by concentrating more magnetic field into the workpiece. This disposition can be also found in the experimental device (see Figure A.1).

Table 3.2: Materials and electrical properties used.

Region	Material	Electrical conductivity A/(Vm)	Relative magnetic permeability
Steel plate	Steel 34CrMo4	Figure 3.5	Figure 3.5
Coil	Copper	$5.9 \cdot 10^7$	1
Concentrator	Fluxtrol 50	0.2	50

The operation parameters concerning the researched process are the power supplied to the induction coil and the cutting speed. In order to have a good penetration of the dissipated power and, therefore, a good temperature homogeneity along the thickness of the plate, the choice of the frequency is very small, 5 Hz. The power supply is chosen to avoid temperatures over 200 °C around the cutting line with a cutting speed of 500 mm/min. To understand the effects of the speed in the magnitude and distribution of the temperature achieved, in another simulation, the current was fixed and the cutting speed was modified to 200 mm/min. The detailed process parameters can be found in Table 3.3.

Table 3.3: Process parameters data used in each simulation.

	Simulation 1	Simulation 2
Cutting speed	500 mm/min	200 mm/min
Frequency	5 Hz	5 Hz
Current	250 000 A	250 000 A

It has to be noticed that the current density is not being defined by means of a voltage as in (3.24). However, most of the simulations were done by controlling the current intensity

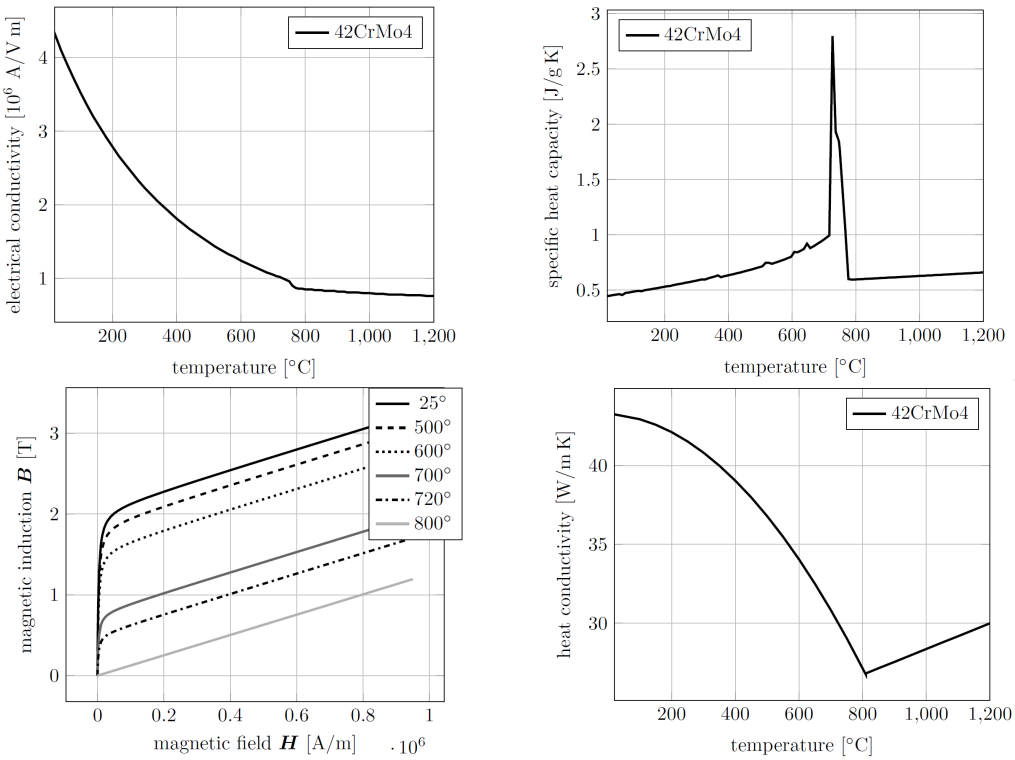

Figure 3.5: Steel 34CrMo4 temperature dependent properties [33].

I [A] (see Table 3.3). This is common in technical applications, where usually the current is controlled. This way, we impose the current intensity I crossing the cross section of the entrance Γ_{in} of the inductor Ω_{c1} as

$$\int_{\Gamma_{in}} \boldsymbol{\mathcal{J}} \cdot \boldsymbol{n} \, \mathrm{d}\, S = I. \tag{3.28}$$

Therefore in the weak formulation of Eq. (3.27g) we would have

$$\int_{\Gamma_{in}} \sigma \nabla V \cdot \boldsymbol{n} \, \mathrm{d}\, S = \int_{\Gamma_{in}} \boldsymbol{\mathcal{J}} \cdot \boldsymbol{n} \, \mathrm{d}\, S. \tag{3.29}$$

For more information on the characterization of electric sources we refer to [33, 43, 35].

3.4 Simulation results

With the simulation of the thermoelectric model, all variables from the system of equations (quasi-stationary heat equation and Maxwell equations) can be represented. Due to the goal of this work, homogenization of temperature in thickness, the focus will be on the temperature itself. Two simulations are analysed, each one having a different cutting speed: 500 and 200 mm/min. These feed rates were recommended by the industrial partner as they are attainable in the cutting shop. As stated before in Subsection 2.1.1, slower cutting speeds and preheating reduce the undesired side effects from flame cutting. The idea is to compare a currently used speed, 200 mm/min, with a higher one which is expected to be used with the support of preheating. The power supplied to the inductor is the same in both studies. It can

be expected that with lower speed, as the plate stays more time below the influence of the coil, the heating will be higher. The obtained results confirm this behaviour.

In the two following subsections, results from 500 and 200 mm/min cases are displayed. Several views from the temperature field can be examined: the whole set steel plate, inductor and concentrator (Figures 3.6), half of steel plate (Figures 3.7), top of steel plate (Figures 3.8, 3.12) and cutting surface (Figures 3.9, 3.13). Moreover, two graphs describe the evolution of the temperature on top and bottom of the cutting line (Figures 3.10, 3.14) and the evolution of difference between top and bottom temperature (Figures 3.11, 3.15).

The maximum temperature in the 500 mm/min case is 219.81 °C while in the 200 mm/min case is 343.18 °C. It is clear that the most interesting case from the industrial point of view is the fastest one as it can increase the production rate.

3.4.1 Cutting speed 500 mm/min

In this case, 200 °C is only surpassed in a small volume below the end of the coil. The furthest location from the cutting line, where over 200 °C is reached, is situated on the top of the plate and below 10 mm from the cutting line (Figure 3.8). The homogenization in thickness increases as the plate goes forward. 80 mm after the coil, temperature in thickness goes from 100 °C (bottom) to 171 °C (top). This difference keeps decreasing; for example, at 380 mm from the end of the coil, a difference of 10 °C is found: 100 °C in the bottom and 115 °C on top (Figure 3.11).The temperature results of the simulation with a cutting speed of 500 mm/min are presented below.

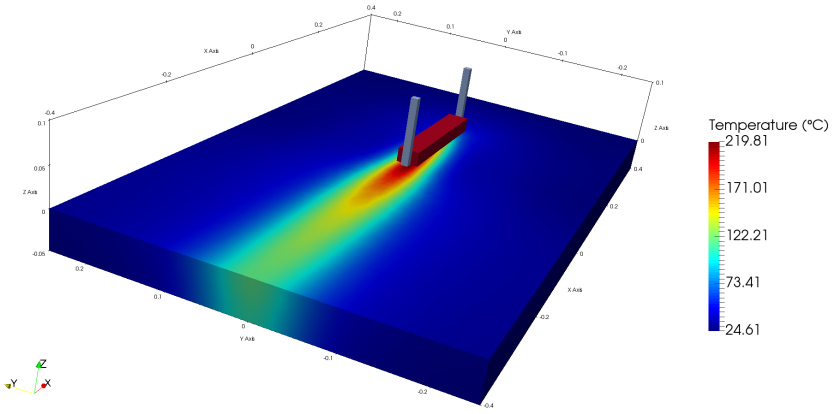

Figure 3.6: Temperature map in the steel plate with coil-concentrator on top (500 mm/min).

3.4.2 Cutting speed 200 mm/min

The results from the second case with cutting speed of 200 mm/min can be observed in the following figures. The temperature field from the isometric view looks qualitatively very similar to the ones in Figures 3.6 and 3.7 so we omit the figures for this case. On the other hand, the effect of the slower cutting speed is noticeable when comparing with the other figures. The slower speed allows more time for the heat to reach further into the plate due to conduction. This wider reach of the heat in the y-direction on top of the plate is clear in Figure 3.8 when

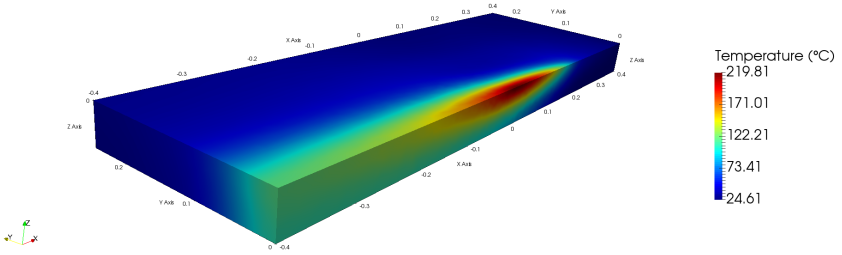

Figure 3.7: Temperature map in the steel plate with cut in the symmetry plane (500 mm/min).

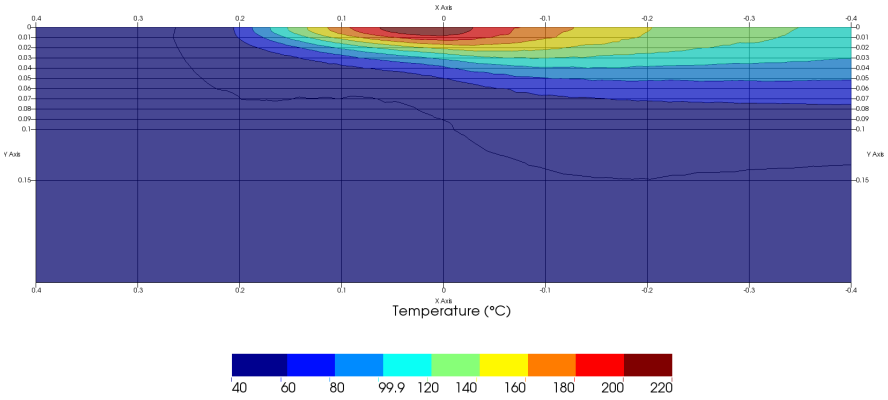

Figure 3.8: Temperatures from top of steel plate (500 mm/min).

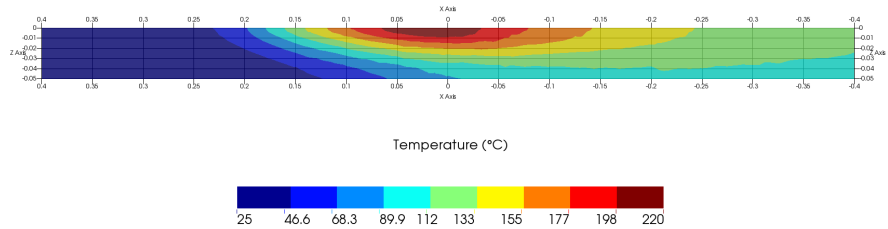

Figure 3.9: Temperatures from cutting surface of steel plate (500 mm/min).

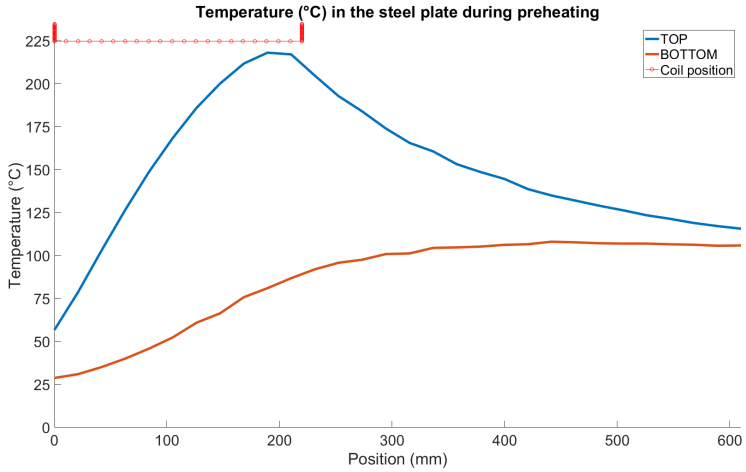

Figure 3.10: Temperature evolution on top and bottom of the cutting line (500 mm/min).

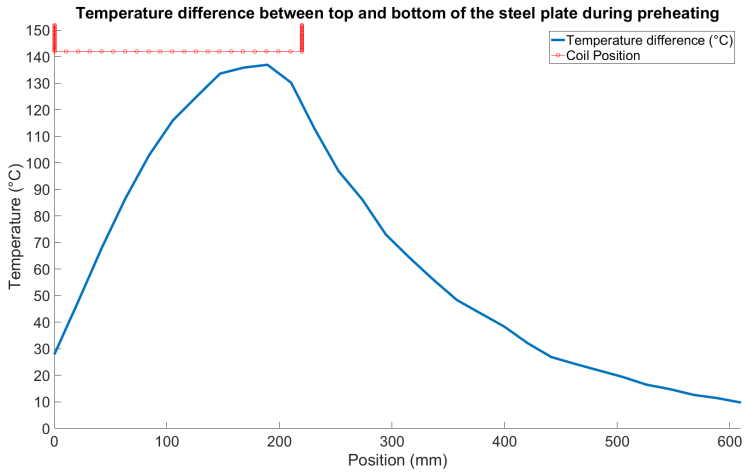

Figure 3.11: Evolution of difference of temperature between top and bottom of the cutting line (500 mm/min).

compared to Figure 3.10. Also, in the z-direction there is more spread of the heat thanks to the lower speed, see Figures 3.13, 3.14. The length of the plate considered is the same in both cases. Looking at the difference of temperature between the top and bottom of the plate (Figs. 3.11, 3.15) it can be seen how a better homogenization is reached in the 200 mm/min case. Translating position [mm] into time [s] by means of the cutting speed, it can be said that temperature homogenization (below 10 °C difference) of an area has been reached 135 s (450 mm) after this area has been below the start of the coil in the 200 mm/min. Meanwhile, for the 500 mm/min case, 72 s (600 mm) are necessary.

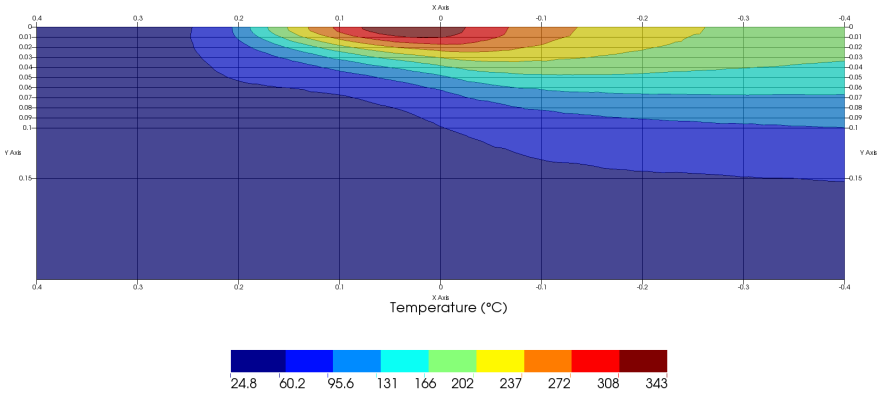

Figure 3.12: Temperatures from top of steel plate (200 mm/min).

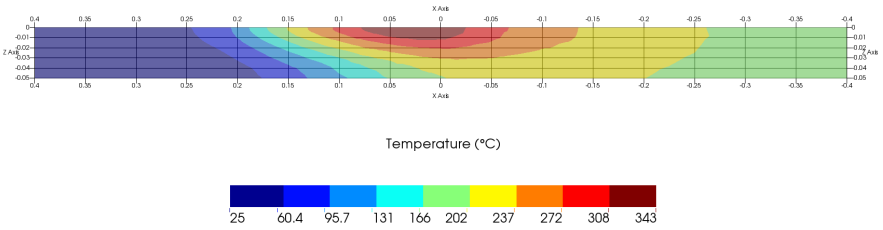

Figure 3.13: Temperatures from cutting surface of steel plate (200 mm/min).

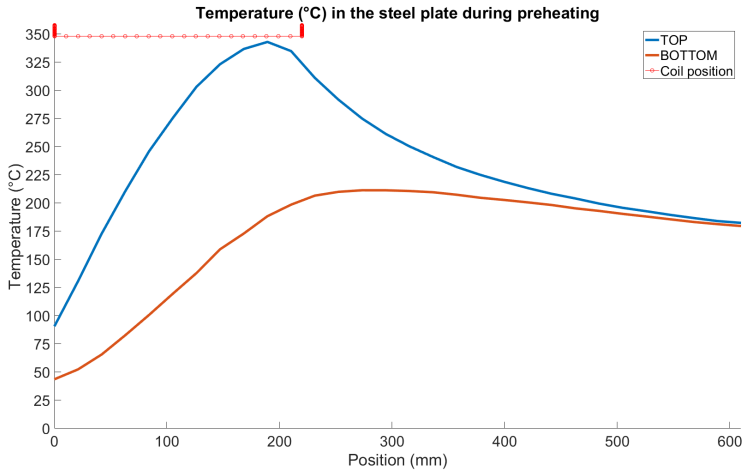

Figure 3.14: Temperature evolution on top and bottom of the cutting line (200 mm/min).

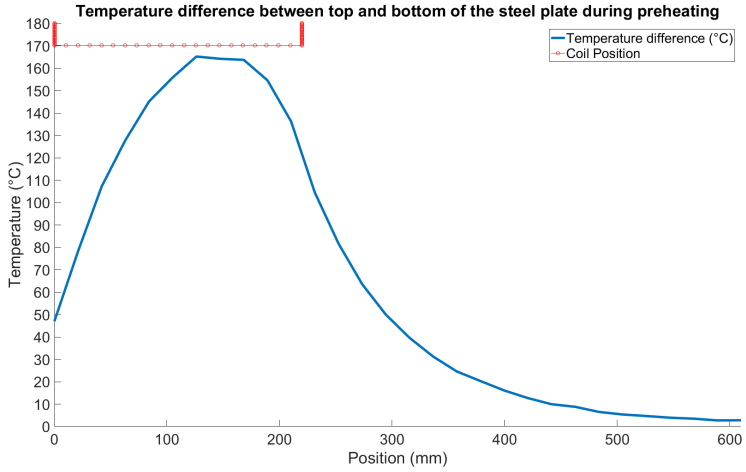

Figure 3.15: Evolution of difference of temperature between top and bottom of the cutting line (200 mm/min).

3.5 Experimental validation

Extensive work has been done to achieve experimental validation of the induction heating model. The industrial partner SSAB informed about an ongoing EU Interreg North project called NorFaST-HT (Nordic Community for Fast Steel Heat Treatments) coordinated by the University of Oulu in which SSAB is a participant. One of the objectives of this project is to research the feasibility of the induction preheating process for steel plates and developing a prototype. Thus, in collaboration with a laboratory from the University of Oulu, an experiment was designed to use as validation of the model described in Section 3.2. The goal is to replicate the experiment conditions in the model and compare temperature profiles on the plate. Now we describe the experimental setting and how temperature data was retrieved and later used for validation.

The experimental setting is very similar to the one already described in Section 3.3: an induction heating head box is fixed on top of a coil while a steel plate moves in a straight trajectory below it at constant speed. The induction heating device used is a CELES MP 25/400 manufactured by Fives Celes, see Figure 3.16a. The lower part of the device contains the

inductor, a coil with concentrator. Figure 3.16b describes the shape of the copper coil (yellow) and the concentrator (black). The concentrator consists of ferrites cores with a relative effective permeability of 2000. For a non-homogeneous core (e.g., gapped or composed of powder-like particles) the relative effective permeability would be the value of relative magnetic permeability of a hypothetical homogeneous material which would exhibit the same permeability [44]. Then, it is assumed that the relative magnetic permeability of the concentrator is 2000. More information on the device can be found in Appendix A.

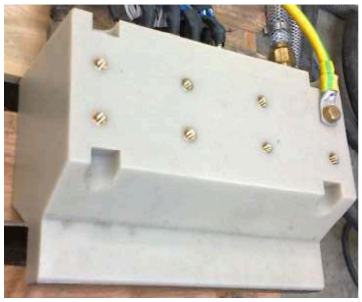

(a) Induction heating head box.

(b) Characteristics of the inner copper coil.

Figure 3.16: Description of the induction heating device CELES MP 25/400. (Courtesy of Fives Celes.)

The plate chosen for the experiment is a Raex® 500 steel plate of 20 mm thickness. Most steel properties necessaries for the model were retrieved, like in Chapter 2, using the commercial software JMatPro® [31], which mainly requires as input the chemical composition (see Table 3.4). Notice that the chemical composition is the same of Raex® 400 but with a higher content of carbon. The only property that could not be retrieved from JMatPro® is the magnetic permeability. Instead, the magnetic permeability of steel 34CrMo4 from Section 3.3 is used. It is assumed that within the temperature range of the experiment it should be similar enough.

Table 3.4: Chemical composition of Raex® 500 (maximum % of elements). The steel is grain refined.

C	Si	Mn	P	S	Cr	Ni	Mo	B
0.30	0.80	1.70	0.025	0.015	1.50	1	0.50	0.005

The plate moves at 750 mm/min below the induction head leaving an air gap of 2 mm between them. The induction heating device works at 80 % capacity producing 21.4 kW with a frequency of 209 kHz.

Thermocouples (TCs) were used to register the temperature values; they are able to record data every 0.01 s. Two sets of thermocouples (TC01 and TC02) were located along the cutting line. Each set consist of a TC located on the top and another one on the bottom. The bottom TCs were exactly at the centreline and the top TCs were at 5 mm distance from the centreline. The distance between the two sets of TCs is 150 mm.

The objective is to measure the quasi-steady-state (QSS) temperature. For that, it is required that the plate is long enough, and the thermocouples are located far enough from the coil to record a uniform pattern. QSS can be said is achieved when the temperature profiles are the same with independence of location where the data has been registered.

The temperature experimental data together with the results of the numerical simulation are shown in Figure 3.17. In the experimental results, it can be seen how the patterns from TC01 and TC02 are very similar when overlapped (shifted 12 s). This supports the idea that QSS has been achieved. Notice that, the temperature from top and bottom homogenizes after the heating. Although the top temperature is recorded 5 mm from the cutting line, this is comparable to the behaviour already seen in the test simulations (Section 3.4).

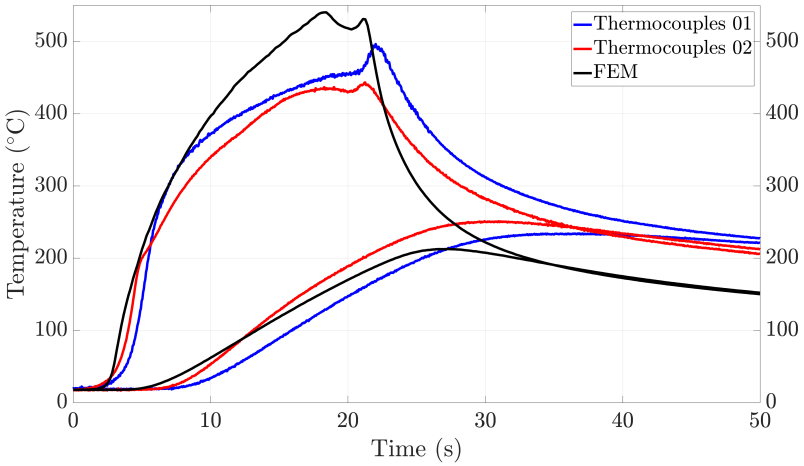

Figure 3.17: Comparison of experimental data and simulation results.

The FEM results were obtained by adjusting the current intensity until good agreement was achieved. Specifically, the simulation results portrayed were obtained with a current intensity of 360 A. The experimental data and the simulation results share the same trend: rapid heating of the top by the coil and homogenization between top and bottom after it.

The experimental validation was a partial success, the temperature values obtained in the simulation were similar and followed the same trend, but the heating and cooling rates did not match. This is thought to be caused by the many unknowns regarding the induction heating device, the electric current used and the thermodynamic and physical properties of the steel. The discussions regarding the differences between the experimental data and the simulation results lead to a thorough numerical study which contributed to better understanding of the model and to improvements in its numerical resolution.

3.6 Modelling of dissipated heat power

Research on the modelling of induction heating of steel plates has brought to the fore valuable knowledge about the distribution of power dissipated in the plate. In this section we present an analytical model able to describe the main patterns in the distribution of Joule heat under the induction heating setting proposed in Sections 3.3-3.5.

Different electromagnetic phenomena take part into the non-uniform distribution of the Joule heat during induction heating, the influence of which is higher or lower depending on the setting. Some of the most common phenomena are Rudnev et al. [34]:

(i) Skin effect.

(ii) Proximity effect.

(iii) Slot effect.

(iv) Ring effect.

(v) End and edge effects.

The proximity effect describes the fact that the eddy currents have a higher density in the workpiece if the coil-to-workpiece air gap is small (good coupling), resulting in an intense electrically efficient heating. The heat pattern will be relatively narrow and deep. Most of the conductor's current will be concentrated on the surface facing the workpiece; however, a small portion of the current will occur on its opposite side. A magnetic concentrator introduced properly (see Figures 3.2, 3.16b) is able to squeeze the inductor current (reducing external magnetic field) to the air gap between the inductor and the workpiece, that is, to the open area of the slot. This phenomenon is called electromagnetic slot effect.

In the current setting the most important is the skin effect while the end and edge effect are also relevant.

Skin depth. As stated before in this chapter, the penetration or skin depth of the electric current is defined as the depth δ at which the current density falls to $1/e$ ($\sim$37 %) of its maximum value found near the surface, [35, 34]. The penetration depth is usually defined in metres as

$$\delta = \sqrt{\frac{1}{\pi f \mu_0 \mu_r \sigma}}, \tag{3.30}$$

where σ is the electrical conductivity of the conductor, f the current frequency, μ_0 the magnetic permeability of free space and μ_r relative magnetic permeability of the conductor, steel being the conductor in our setting.

The value of δ is inversely proportional with the square root of frequency, relative magnetic permeability and conductivity. While the electrical current in the surface of the conductor decreases exponentially ($1/e$) towards its bottom, the power density decreases with the square of the exponential ($1/e^2$) from its value at the surface (see Eq. (3.25)).

However, according to [34], it is common to consider a regular exponential decay for the power density in most publications, but this is correct only if the conductivity of the conductor is homogeneous and constant. The conductivity σ of the steel it is known to be temperature dependant (see Figure 3.5) but within the temperature range of preheating the change is not too strong. Thus, for the sake of simplicity and for numerical reasons (smoothness), we will consider the decay of the power density in the steel plate due to the skin effect as

$$f_3(z) = e^{c_3 z}, \tag{3.31}$$

being c_3 a not null parameter. It is easy to check that f_3 verifies full power at surface of the plate ($z = 0$) with $f_3(0) = 1$ and negligible power at bottom ($z = -h$) with $f_3(-h) \approx 0$. Moreover, by the definition of skin effect, it must verify that $f_3(-\delta) = 1/e \approx 37\%$. This way,

$$\delta = 1/c_3. \tag{3.32}$$

Despite the conductivity σ and the relative magnetic permeability μ_r being temperature dependant for steel. During preheating, temperatures should not be higher than 400 °C and therefore, we can choose a constant value for the properties as reference. Therefore, we can find a clear relationship between the frequency f and the modelling constant c_3:

$$c_3 = \sqrt{\pi f \mu_0 \mu_r \sigma}. \tag{3.33}$$

Considering a generic carbon steel, we can choose a common value for σ of 7×10^6 A m/V and for μ_r, 100. Obtaining this way, a simple expression for c_3:

$$c_3 \approx 52.54\sqrt{f}. \tag{3.34}$$

In Table 3.5, we gather some values for c_3 and the skin depth δ for several frequency values.

Table 3.5: Relation between frequency f and modelling constant c_3.

Frequency f [Hz]	Constant c_3	Skin depth δ [mm]
1	52.54	19.03
5	117.49	8.51
50	371.53	2.69
1000	1661.54	0.60
10000	5254	0.19
100000	16615.4	0.06

In order to verify that the model provides a good approximation, it was compared with results obtained by solving the system (3.23) with FEM. Profiles of the dissipated power in the z-direction were extracted at different positions below the coil. Being aware that these profiles were different, the parameter $c3$ was obtained by solving a nonlinear curve-fitting (data-fitting) problem in the least-squares sense. The comparison of the modelling exponential curve with the FEM curves for two different settings is displayed in Figure 3.18.

The values obtained for $c3$ were approximately 6000 and 10000 while the frequency values were 5000 to 10 000 Hz respectively. On the other hand, by the formula from (3.34), the values of c_3 would have been approximately 3700 and 5200. Although the values differ, as we are dealing with exponentials we consider the proposed exponential decay to be a good approximation.

End and edge effect. After describing the skin effect, which influences the distribution of the power density in the z-direction (depth of plate), we can focus on x and y distribution on the surface of the plate. The power density on the surface of the plate is not uniform under the coil, that is, it is not distributed uniformly in a perfect rectangular shape. The end and edge effects are referred to the distortion of the electromagnetic field in the coil's end and edge regions. Figure 3.19 outlines these changes in the longitudinal (x-axis) and transverse (y-axis) directions. Accordingly, the effects are also known as longitudinal electromagnetic end effect and transversal electromagnetic edge effect, respectively.

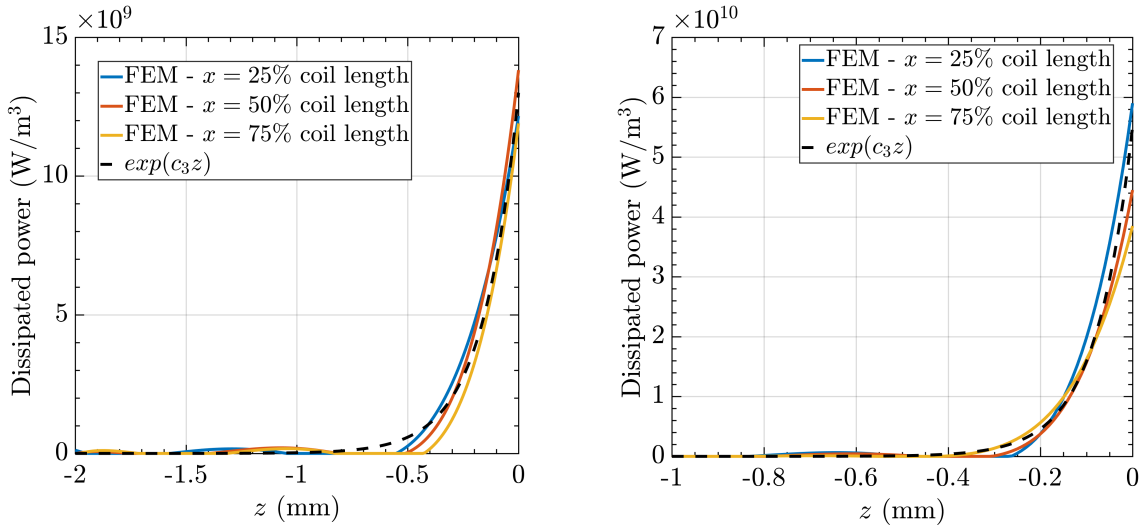

(a) $c_3 = 6000$. **(b)** $c_3 = 10000$.

Figure 3.18: Comparison of the model function for decay in the z-direction with FEM results.

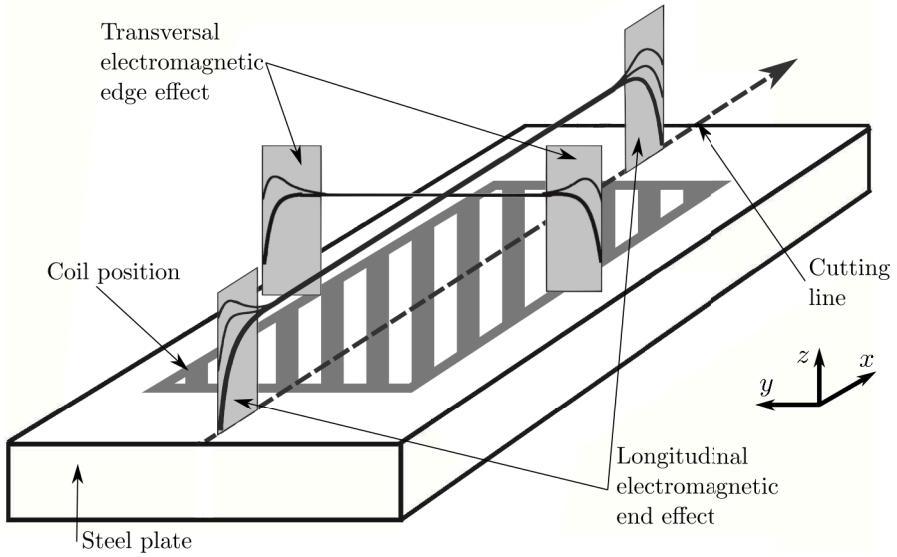

Figure 3.19: End and edge effects during induction heating.

From the modelling point of view, the longitudinal electromagnetic end effect was neglected. The effects on the power distribution are mainly related to the length of the coil which is not relevant to the study. Consequently, to represent that the power is distributed along the length of the coil, the function $\chi(x)$ was chosen. It is the characteristic function of the interval, along the x, axis where the coil is located, that is, this function has value 1 along the length of the coil and 0 otherwise.

Similarly to the modelling of the skin effect, dissipated power profiles from two FEM simulations were extracted. In this case, the profiles were taken from the surface of the steel plate in the x-direction. These were normalized and are represented with the respective $\chi(x)$ function indicating the location of the coil in Figure 3.20.

The main difference between the two profiles is that in Figure 3.20b the power raised the temperature in the plate over the Curie temperature and this way reducing drastically the

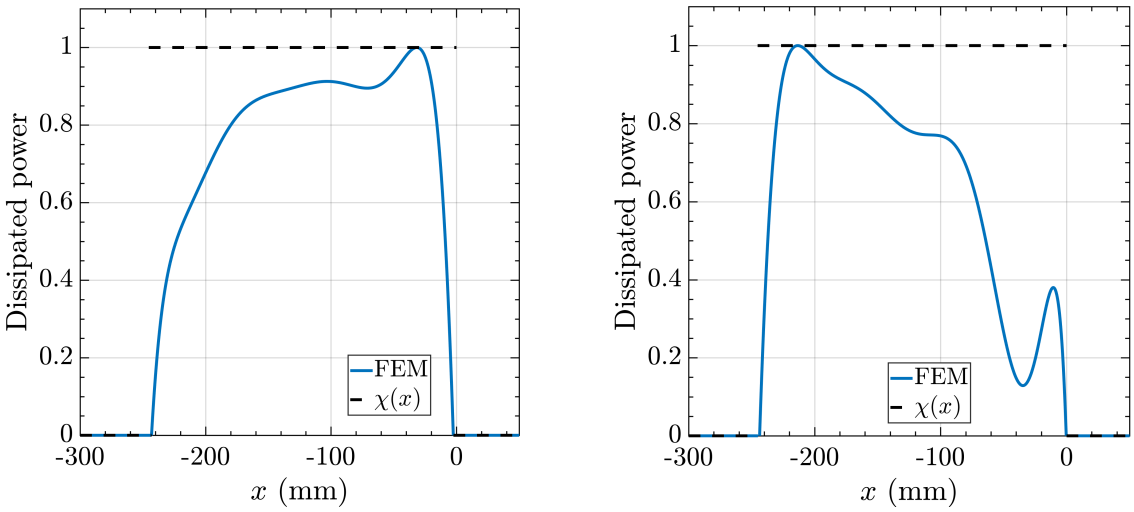

(a) Dissipated power profile.

(b) Dissipated power profile that reaches Curie temperature.

Figure 3.20: Normalized dissipated power profiles from preheating FEM simulations.

magnetic permeability of the steel and therefore reducing the absorption of eddy currents. On the other case, the temperature values were below 300 °C and could be used for preheating. As stated before, with the use of $\chi(x)$ we neglect the end effects, that is the steep increase and decrease of the power at the beginning and ending of the coil.

Finally, the transversal electromagnetic edge effect is important to understand how wide the heating from the cutting line is. We choose a exponential decay in the y-direction to reflect that the maximum power is induced in the centreline below the coil and decreases with the width of the coil. Similarly to Eq. (3.31),

$$f_2(y) = e^{-c_2 y}. \tag{3.35}$$

The constant c_2 is related to half the width of the coil as we are considering the symmetry along the cutting plane. For lack of references, the value was chosen based on the experience obtained from simulations.

Figure 3.21 show the decays of the dissipated power in the y-direction at different positions of the coil from two FEM simulations. Again, the value of the parameter c_2 was obtained by solving a least-square problem. The values employed in Figs. 3.21a and 3.21b were 300 and 182 respectively. It is noticeable that the patterns are not exactly exponentials, but we consider that by choosing the parameter c_2 of the order of 10^2 it is a valid approximation.

All in all, the 3D-model to describe the power density generated in the steel plate by an inductor located on top of it is

$$\gamma(\boldsymbol{x}) = \chi(x) e^{-c_2 y} e^{c_3 z}. \tag{3.36}$$

The signs within the exponential functions are in accordance with the definition of the steel plate. That is, $\{z = 0\}$ the surface, $\{z = -h\}$ the bottom, $\{y = 0\}$ the symmetry plane and $\{y = y_{max}\}$ the side at the maximum width of the plate.

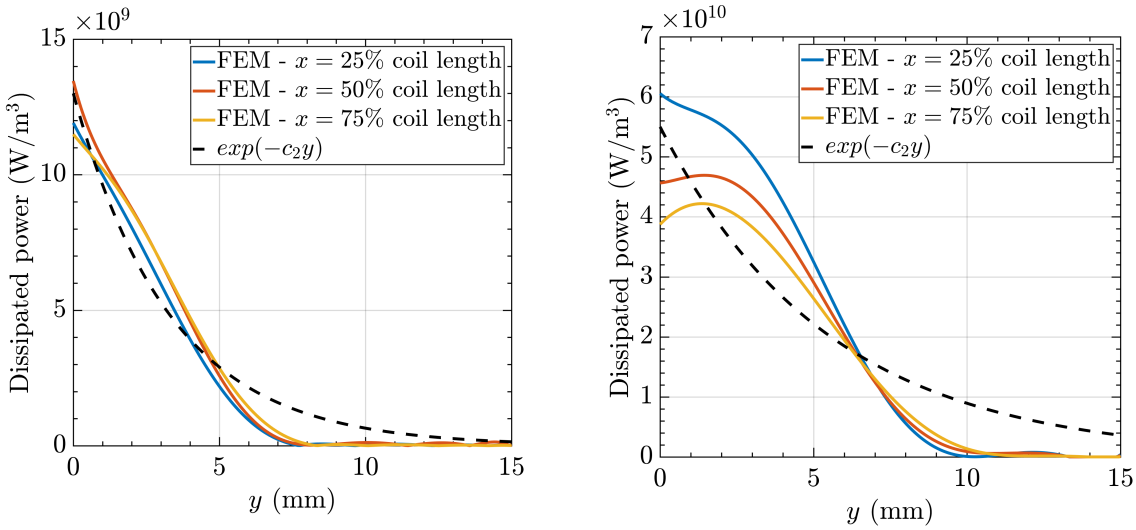

(a) $c_2 = 300$. **(b)** $c_2 = 182$.

Figure 3.21: Comparison of the model function for decay in the y-direction with FEM results.

3.7 Conclusions

Even though the results presented in Chapter 3 seem promising, in order to have a realistic use of the simulations for the industry, it is necessary that material properties of the specific steel employed in the real process are acquired.

The experience obtained was used to develop a simplified model of the Joule heat released in the plate during induction heating. The introduction of this model can substitute the computationally expensive electromagnetic model in the optimization algorithm presented in Chapter 4 and this way, obtain faster results.

To this end, we will define the heat source coming from the dissipated power as Q_{eddy} based on $\gamma(\boldsymbol{x})$ instead of $\frac{\bar{\sigma}(\theta)\omega^2}{2}|\boldsymbol{\mathcal{A}}|^2$ from (3.25).

4

Optimal control of the preheating for flame cutting of steel plates

We consider a model to describe the flame cutting of steel plates with an induction preheating process. The flame cutting model covered in Chapter 2 is expanded to include an extra heat source for the preheating. The experience from simulations of induction heating obtained in Chapter 3 is used to restrict the preheat source so it resembles the distribution that could be obtained from an induction coil located on top of the plate. The resulting model is analysed to prove the existence, uniqueness and regularity of the solutions of the system of equations. In addition, the final goal is to define an optimal control problem to find the power necessary to achieve a desired working temperature in the plate for flame cutting. From the analytical point of view, optimality conditions are derived for this involved nonlinear elliptic system. From the numerical point of view, the optimal control problem is solved numerically applying FEM and the projected gradient method [45].

Outline. First, in Section 4.1 the flame cutting process is presented jointly with the motivation for induction preheating. In Section 4.2, we describe a flame cutting model of steel plates with preheating, consisting of a quasi-stationary heat equation coupled with a set of equations describing the phase transitions in steel. We analyse the system of equations in Section 4.3. In Section 4.4 we derive a linearised version of the state equations. Section 4.5 is devoted to establish the optimal control problem which numerical resolution approach is given in Section 4.6. The results for a single flame cutting with preheating setting are presented in Section 4.7. Finally, some concluding remarks are set on Section 4.8.

4.1 Introduction

The manufacturing of steel plates relies on a cutting process to obtain a uniform shape in the final stage of production. Flame cutting is considered a common, versatile and efficient method as it can be used for a wide range of thicknesses and is more economical than other thermal cutting methods like plasma arc or laser.

During flame cutting, a plate moves at uniform speed below a fixed torch. The burning chemical reaction caused by the flame brings the material to melting point and the high pressure oxygen from the torch blows the molten material, leaving a thin gap named kerf. The remaining cutting edge, around which, a heat affected zone (HAZ) is created, undergoes microstructural changes. Specifically, solid-solid phase transitions that result in changes in the thermomechanical properties [28]. These changes are unwanted at this stage of the production as the properties of the steel have been already established with different heat treatment processes. Essentially, flame cutting causes high residual stresses in the cutting edge of the steel plate. These residual stresses can be divided into transformation and thermal stresses. Transformation stresses arise from the aforementioned microstructural changes which are accompanied by volume changes. Thermal stresses originate from the different heating and cooling rates experienced by the surface and the interior of the steel plate [46].

It has been found that, under certain cutting settings, cold cracks can appear a couple of days after the cutting possibly due to tensile stress, hydrogen content and the microstructural effects [47, 21]. However, preheating of the plates just before flame cutting has been found to lower residual stresses, this way, reducing the likeliness of cold cracks [1, 47, 21].

In this chapter, we propose a similar setting to the one described in Chapter 3 with an induction coil to be used for the preheating. A fixed copper coil is positioned above the steel plate. When the coil is traversed by an electrical current, it induces currents on the plate and, as a result, heat is generated in the steel by Joule effect. The coil above the cutting line and at some distance from the torch, preheats the area to be affected later by flame cutting (see Figure 4.1). This local preheating method is more energy efficient than a current practice which consist of preheating the whole plates in a furnace.

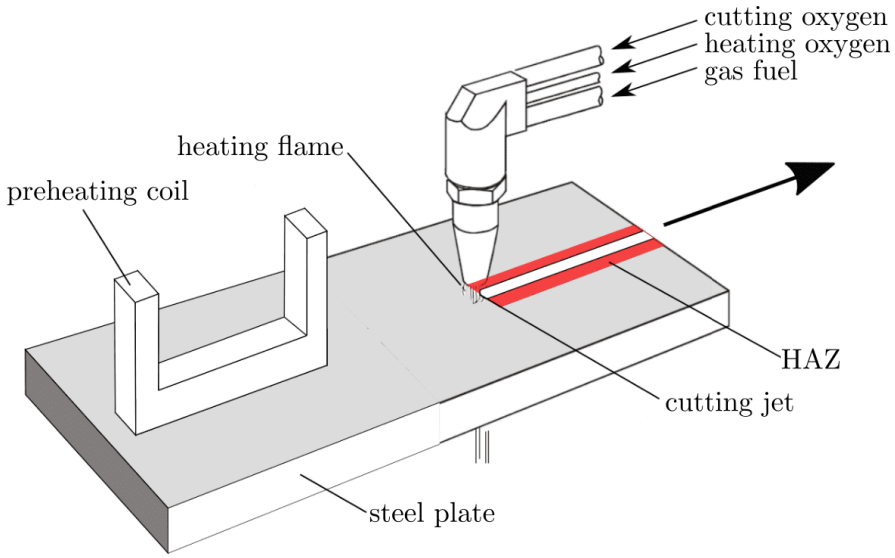

Figure 4.1: Scheme of flame cutting of a moving steel plate with induction preheating coil.

As explained in Chapter 2, in contrast to welding, which is a similar physical process, there are very few publications studying thermal cutting from a modelling and numerical simulation point of view, even less considering preheating. One of the few cases considering preheating of steel plates for cutting is Lindgren et al. [1] (1993). The authors use a 2D-model to study the temperature evolution in the section transverse to the direction of the flame cutting. The

thermal analysis is combined with a mechanical analysis and reveals the decrease in residual stress with a preheating stage of the plate prior to cutting. More recently, Jokiaho et al. [2] (2017) employ the commercial finite element software ABAQUS to model the flame cutting of thick plates. Again, a 2D-model is used to register the nodal temperature history in the transverse plane. The study focuses on experimental and numerical stress analyses under different operating conditions: thickness, speed, preheating stage. They conclude that lower residual stresses can be achieved by preheating and slowing the cutting speed, both combined or separately.

Instead of the global preheating considered in the previous references, we study the proposed local preheating by including it in the 3D flame cutting model illustrated in Chapter 2.

4.2 Model

The goal of the model is to understand the heat distribution in a moving steel plate during preheating and flame cutting with the subsequent heat affected zone (HAZ) and the trail of molten steel. The big dimensions of a steel plate (3000 mm long) in comparison to the HAZ caused by the flame (5 mm) allow to consider that a quasi-stationary state (QSS) is reached in the workpiece. Using the symmetry along the cutting line, we reduce the domain to only half of the steel plate, denoted by Ω. Accordingly, for the temperature θ in the plate, we can employ the quasi-stationary state (QSS) heat equation [30],

$$\rho C_p(\theta)\,(\boldsymbol{v}\cdot\nabla\theta) - \nabla\cdot(\tilde{\kappa}(\theta)\,\nabla\theta) + \rho\boldsymbol{L}\cdot\tilde{\boldsymbol{f}}(\theta,\boldsymbol{\zeta}) = q \quad \text{in } \Omega. \tag{4.1}$$

Different steel parameters are required for this equation: density ρ, heat capacity $C_p(\theta)$ and thermal conductivity $\tilde{\kappa}(\theta)$. One important aspect is that these properties are temperature dependent, adding nonlinearities to equation (4.1).The velocity $\boldsymbol{v}$ is a vector which, in this case, has only x as non-zero component as the trajectory of the plate is a straight line along the x axis: $\boldsymbol{v} = (v, 0, 0)^T$. The term $\rho\boldsymbol{L}\cdot\tilde{\boldsymbol{f}}(\theta,\boldsymbol{\zeta})$ corresponds to the heat absorbed and released during phase transitions, known as latent heat. The heat by the phase transformations is determined by the steel density ρ, the latent heat $\boldsymbol{L}$ and function $\tilde{\boldsymbol{f}}$. Each component $\boldsymbol{L}_i$ and $\tilde{\boldsymbol{f}}_i$ for $i = 1,\ldots,m$ corresponds to a phase transformation. As an example, if the model includes liquid, austenite and martensite phases we would have

$$\boldsymbol{\zeta} = (l, a, m)^T \quad \text{and} \quad \boldsymbol{f} = (f_l(\theta,l), f_a(\theta,l,a,m), f_m(\theta,l,a,m))^T. \tag{4.2}$$

The term q on the right-hand side of (4.1) is related to the heat source and therefore, to the flame and the iron burning exothermic reaction plus the heat added by induction preheating.

$$q = Q_F(\boldsymbol{v}) + Q_{\text{eddy}} = Q_F(\boldsymbol{v}) + u\cdot\gamma. \tag{4.3}$$

The definition of q includes the term $Q_F(\boldsymbol{v})$ describing the heat created by the torch. It is defined as a constant power density uniformly distributed within a particular volume Λ and assumed to be zero outside of it. The volume Λ is similar to a cylinder whose radius changes with height. The dependency of Q_F with respect of the velocity $\boldsymbol{v}$ comes from the consideration that the radius of Λ changes as a function of $\boldsymbol{v}$. For more information we refer to

Chapter 2 where the flame cutting model is described thoroughly. On the other hand, Q_{eddy}, relates to the heat generated by induction preheating. We define it with u, which will be the control variable of the optimal control problem. With the goal of achieving a realistic induction heating, we add γ as a projection factor to u. We choose γ according to the simple dissipated power distribution model developed in Section 3.6 so the preheating power is restricted to the length of a coil and has exponential decays in the depth of the plate (skin depth) and in the transverse direction of the induction coil.

As seen in (4.1), the phase transitions in steel have an effect on the temperature distribution. Accordingly, we introduce a set of equations corresponding to each transformation in steel occurring during flame cutting: solid-solid changes and solid-liquid (melting). The concentration of each transformation is stored in $\boldsymbol{\zeta}$ component-wise.

$$(\boldsymbol{v}\cdot\nabla)\boldsymbol{\zeta} - \varepsilon\Delta\boldsymbol{\zeta} - \tilde{\boldsymbol{f}}(\theta,\boldsymbol{\zeta}) = 0 \quad \text{in } \Omega. \tag{4.4}$$

This model is derived from [29], where a transient model based on the Leblond-Devaux model is proposed that reproduces the relative volume fraction of the different solid phases of steel during a heating and cooling cycle.

To complete the PDE system, we need to impose boundary conditions on the faces of Ω. This way, we use Γ_N for the faces where we impose Neumann boundary conditions and Γ_D where a Dirichlet condition is imposed. Finally, to simplify the notation, the product ρC_p is substituted by $\tilde{\eta}$.

Thus, the governing equations read as

$$\tilde{\eta}(\theta)(\boldsymbol{v}\cdot\nabla)\theta - \nabla\cdot(\tilde{\kappa}(\theta)\nabla\theta) + \rho\boldsymbol{L}\cdot\tilde{\boldsymbol{f}}(\theta,\boldsymbol{\zeta}) = q \quad \text{in } \Omega\,, \tag{4.5a}$$

$$\boldsymbol{n}\cdot\tilde{\kappa}(\theta)\nabla\theta + h(\theta-\theta_0) = 0 \quad \text{on } \Gamma_N\,, \qquad \theta = \theta_0 \quad \text{on } \Gamma_D\,, \tag{4.5b}$$

$$(\boldsymbol{v}\cdot\nabla)\boldsymbol{\zeta} - \varepsilon\Delta\boldsymbol{\zeta} - \tilde{\boldsymbol{f}}(\theta,\boldsymbol{\zeta}) = \boldsymbol{0} \quad \text{in } \Omega\,, \tag{4.5c}$$

$$\boldsymbol{n}\cdot\nabla\boldsymbol{\zeta} = \boldsymbol{0} \quad \text{on } \Gamma_N\,, \qquad \boldsymbol{\zeta} = \boldsymbol{\zeta}_0 \quad \text{on } \Gamma_D\,. \tag{4.5d}$$

The vector $\boldsymbol{n}$ is an outward normal unit vector to the corresponding surface. We assume that $\boldsymbol{v}\cdot\boldsymbol{n} \geq 0$ on Γ_N that $\tilde{\eta}$ and $\tilde{\kappa}$ are sufficiently smooth and bounded from below and above, i.e., $0 < c \leq \tilde{\eta}(r), \tilde{\kappa}(r) \leq C$ for two constants $c < C \in \mathbb{R}$.

Since the equation is rather transport dominated, we use the enthalpy transformation to get a linear transport term. We define $\eta(\theta) = \int_0^\theta \tilde{\eta}(r)\,\mathrm{d}\,r$. Note that the derivative $\eta' = \tilde{\eta}$ is well controlled from below and above, which assures that η is monotone and bijective such that η^{-1} is well defined and monotone, too. By defining $\vartheta := \eta(\theta)$ the equations can be reformulated for ϑ. With $\kappa(\vartheta) := \tilde{\kappa}(\eta^{-1}(\vartheta))/\tilde{\eta}(\eta^{-1}(\vartheta))$, $\boldsymbol{f}(\vartheta,\boldsymbol{\zeta}) := \tilde{\boldsymbol{f}}(\eta^{-1}(\vartheta),\boldsymbol{\zeta})$, and $g(\vartheta) := h\eta^{-1}(\vartheta)$, we find

$$(\boldsymbol{v}\cdot\nabla)\vartheta - \nabla\cdot(\kappa(\vartheta)\nabla\vartheta) + \rho\boldsymbol{L}\cdot\boldsymbol{f}(\vartheta,\boldsymbol{\zeta}) = q \quad \text{in } \Omega\,, \tag{4.6a}$$

$$\boldsymbol{n}\cdot\kappa(\vartheta)\nabla\vartheta + g(\vartheta) = 0 \quad \text{on } \Gamma_N\,, \qquad \vartheta = 0 \quad \text{on } \Gamma_D\,, \tag{4.6b}$$

$$(\boldsymbol{v}\cdot\nabla)\boldsymbol{\zeta} - \varepsilon\Delta\boldsymbol{\zeta} - \boldsymbol{f}(\vartheta,\boldsymbol{\zeta}) = \boldsymbol{0} \quad \text{in } \Omega\,, \tag{4.6c}$$

$$\boldsymbol{n}\cdot\nabla\boldsymbol{\zeta} = \boldsymbol{0} \quad \text{on } \Gamma_N\,, \qquad \boldsymbol{\zeta} = \boldsymbol{0} \quad \text{on } \Gamma_D\,. \tag{4.6d}$$

Note that, in order to reduce the notational complexity, we also normalized the Dirichlet boundary conditions to homogeneous ones. Therefore, we have to assume that θ_0 and $\boldsymbol{\zeta}_0$ are sufficiently smooth, i.e., $\theta_0 \in \boldsymbol{W}^{1-1/p,p}(\partial\Omega)$ and $\boldsymbol{\zeta}_0 \in H^{1/2}(\partial\Omega)^m$. See [48, Section 5.3] or [49, Proposition 3.31].

4.3 Existence, uniqueness, and regularity of the solutions to the state equations

Assumption 1. *Let Ω be a bounded Lipschitz domain in dimension $d = 2$ or 3 with two boundary parts $\partial\Omega = \Gamma_D \cup \Gamma_N$. We assume that $\boldsymbol{v} \in \mathcal{C}^1(\Omega)^d$ with $\nabla\cdot\boldsymbol{v} = 0$, $\boldsymbol{n}\cdot\boldsymbol{v} \le 0$ on Γ_D, and $\boldsymbol{n}\cdot\boldsymbol{v} \ge 0$ on Γ_N. The function $\kappa : \mathbb{R} \to \mathbb{R}$ is bounded from below and above and Lipschitz continuous, i.e., there exists $\underline{\kappa}, \overline{\kappa} \in \mathbb{R}$ such that $0 < \underline{\kappa} \le \kappa(y) \le \overline{\kappa}$ for all $y \in \mathbb{R}$ and $\kappa \in \mathcal{C}^{0,1}(\mathbb{R})$. Let the functions $g \in \mathcal{C}^{0,1}(\mathbb{R})$ be monotone. We assume that the function $\boldsymbol{f}$ has the following form: $\boldsymbol{f}(\vartheta,\boldsymbol{\zeta}) = \tilde{\boldsymbol{f}}(\boldsymbol{\zeta}_{eq}(\vartheta) - \boldsymbol{\zeta})$, where $\tilde{\boldsymbol{f}} : \mathbb{R}^m \to \mathbb{R}^m$ with $\tilde{\boldsymbol{f}} \in W^{1,\infty}(\mathbb{R}^m,\mathbb{R}^m)$ and $(\nabla\tilde{\boldsymbol{f}})_{ij} = 0$ for $i \ne j$ and $(\nabla\tilde{\boldsymbol{f}})_{ii} \ge 0$ for all i, $j \in \{1,\dots,m\}$. Additionally, $\boldsymbol{\zeta}_{eq} \in (W^{1,\infty}(\mathbb{R},\mathbb{R}))^m$ with $\boldsymbol{\zeta}_{eq_i}' \ge 0$ and $\rho\boldsymbol{L}_i \ge 0$ for $i \in \{1,\dots,m\}$. Note that the derivatives are all defined in a generalized sense and the inequalities only hold almost everywhere.*

Definition 2 (weak solution). *Let $p \in (3,6)$. For $q \in W^{-1,p}_{\Gamma_D}(\Omega)$ the pair $(\vartheta,\boldsymbol{\zeta}) \in \boldsymbol{W}^{1,p}_{\Gamma_D}(\Omega) \times H^1_{\Gamma_D}(\Omega)^m$ is a weak solution to system (4.6), if*

$$\int_\Omega (\boldsymbol{v}\cdot\nabla)\vartheta\varphi + \kappa(\vartheta)\nabla\vartheta\cdot\nabla\varphi + \rho\boldsymbol{L}\cdot\boldsymbol{f}(\vartheta,\boldsymbol{z})\varphi\,d\boldsymbol{x} + \int_{\Gamma_N} g(\vartheta)\varphi\,dS = \int_\Omega q\varphi\,d\boldsymbol{x}\,. \tag{4.7}$$

and

$$\int_\Omega (\boldsymbol{v}\cdot\nabla)\boldsymbol{\zeta}\cdot\boldsymbol{\psi} + \varepsilon\nabla\boldsymbol{\zeta} : \nabla\boldsymbol{\psi} - \boldsymbol{f}(\vartheta,\boldsymbol{\zeta})\cdot\boldsymbol{\psi}\,d\boldsymbol{x} = \boldsymbol{0} \tag{4.8}$$

are valid for all $\varphi \in W^{1,p'}_{\Gamma_D}(\Omega)$ with $1/p + 1/p' = 1$ and $\boldsymbol{\psi} \in H^1_{\Gamma_D}(\Omega)^m$.

Theorem 3. *Let the assumptions 1 be satisfied. Additionally, let $q \in W^{-1,p}$ for $p \in (3,6)$. Then there exists a unique solution $(\vartheta,\boldsymbol{\zeta})$ to the system modelling flame cutting of steel plates (4.6) in the sense of Definition (2), which enjoys additional regularity, i.e., $\vartheta \in \mathcal{C}^\alpha(\Omega)$ for some $\alpha > 0$.*

Before we prove Theorem 3, we provide a comparison criterion, which will prove the uniqueness assertion of Theorem 3.

Definition 4 (weak sub and super solution). *For $q \in \boldsymbol{H}^{-1}_{\Gamma_D}(\Omega)$ and $\boldsymbol{a} \in L^2(\Omega)^d$ the pair $(\vartheta,\boldsymbol{\zeta}) \in \boldsymbol{H}^1_{\Gamma_D}(\Omega) \times \boldsymbol{H}^1_{\Gamma_D}(\Omega)^m$ is a weak sub (super) solution to system (4.6), if*

$$\int_\Omega (\boldsymbol{v}\cdot\nabla)\vartheta\varphi + \kappa(\vartheta)\nabla\vartheta\cdot\nabla\varphi + \boldsymbol{L}\cdot\boldsymbol{f}(\vartheta,\boldsymbol{z})\varphi + \vartheta\boldsymbol{a}\cdot\nabla\varphi\,d\boldsymbol{x} + \int_{\Gamma_N} g(\vartheta)\varphi\,dS \le (\ge) \int_\Omega q\varphi\,d\boldsymbol{x}\,. \tag{4.9}$$

and

$$\int_\Omega (\boldsymbol{v}\cdot\nabla)\boldsymbol{\zeta}_i\cdot\boldsymbol{\psi}_i + \varepsilon\nabla\boldsymbol{\zeta}_i\cdot\nabla\boldsymbol{\psi}_i - \boldsymbol{f}_i(\vartheta,\boldsymbol{\zeta})\boldsymbol{\psi}_i\,d\boldsymbol{x} \le (\ge) 0 \quad \text{for all } i \in \{0,\dots,m\} \tag{4.10}$$

are valid for all $\varphi \in H^1_{\Gamma_D}(\Omega)$ *and* $\boldsymbol{\psi} \in H^1_{\Gamma_D}(\Omega)^m$ *with* φ, $\boldsymbol{\psi}_i \geq 0$ *a.e. on* Ω *for all* $i \in \{0, \dots, m\}$.

Proposition 5. *Let Assumption 1 be fulfilled and let* $\boldsymbol{a} \in L^2(\Omega)^d$. *Let* $(\underline{\vartheta}, \underline{\boldsymbol{\zeta}})$ *be a sub solution and* $(\overline{\vartheta}, \overline{\boldsymbol{\zeta}})$ *a super solution according to Definition 4. Additionally, let* $\underline{\vartheta} \leq \overline{\vartheta}$ *on* Γ_D *as well as* $\underline{\boldsymbol{\zeta}}_i \leq \overline{\boldsymbol{\zeta}}_i$ *on* Γ_D *for* $i \in \{1, \dots, m\}$. *Then it holds* $\underline{\vartheta} \leq \overline{\vartheta}$ *and* $\underline{\boldsymbol{\zeta}}_i \leq \overline{\boldsymbol{\zeta}}_i$ *a.e. on* Ω *for* $i \in \{1, \dots, m\}$.

Proof. To show the comparison principle, we follow the argument used in Casas and Tröltzsch [6], which is originated in Křížek and Liu [9] and has also been used in Druet et al. [7]. Here we extend this technique to the considered case, which differs from the previous cases by being vector-valued, and due to the non-monotone transport term and the non-monotone nonlinearity $\boldsymbol{f}$.

We define the test functions $\theta^\delta := \min\{\delta, \max\{0, \underline{\vartheta} - \overline{\vartheta}\}\}$ and $\boldsymbol{\omega}_i^\delta := \min\{\delta, \max\{0, \rho \boldsymbol{L}_i(\underline{\boldsymbol{\zeta}}_i - \overline{\boldsymbol{\zeta}}_i)\}\}$. It holds $\theta^\delta \in H^1_{\Gamma_D}(\Omega)$, $\boldsymbol{\omega}^\delta \in H^1_{\Gamma_D}(\Omega)^m$, such that testing (4.9) with θ^δ and (4.10) with $\boldsymbol{\omega}^\delta$ is allowed. Adding both resulting equations for $(\underline{\vartheta}, \underline{\boldsymbol{\zeta}})$ and subtracting the sum of both equations for $(\overline{\vartheta}, \overline{\boldsymbol{\zeta}})$, we find

$$\begin{aligned}
&\int_\Omega (\boldsymbol{v} \cdot \nabla)(\underline{\vartheta} - \overline{\vartheta})\theta^\delta + \left(\kappa(\underline{\vartheta})\nabla\underline{\vartheta} - \kappa(\overline{\vartheta})\nabla\overline{\vartheta}\right) \cdot \nabla\theta^\delta + \varepsilon\nabla(\underline{\boldsymbol{\zeta}} - \overline{\boldsymbol{\zeta}}) : \nabla\boldsymbol{\omega}^\delta + (\boldsymbol{v} \cdot \nabla)(\underline{\boldsymbol{\zeta}} - \overline{\boldsymbol{\zeta}}) \cdot \boldsymbol{\omega}^\delta \,\mathrm{d}\boldsymbol{x} \\
&+ \int_{\Gamma_N} (g(\underline{\vartheta}) - g(\overline{\vartheta}))\theta^\delta \,\mathrm{d}S + \int_\Omega (\boldsymbol{f}(\underline{\vartheta}, \underline{\boldsymbol{\zeta}}) - \boldsymbol{f}(\overline{\vartheta}, \overline{\boldsymbol{\zeta}})) \cdot (\theta^\delta \rho \boldsymbol{L} - \boldsymbol{\omega}^\delta) + (\underline{\vartheta} - \overline{\vartheta})\boldsymbol{a} \cdot \nabla\theta^\delta \,\mathrm{d}\boldsymbol{x} \leq 0
\end{aligned}$$

Integrating-by-parts the terms due to convection and ordering the terms, we observe

$$\int_{\partial\Omega} (\boldsymbol{v} \cdot \boldsymbol{n}) \left((\underline{\vartheta} - \overline{\vartheta})\theta^\delta + ((\underline{\boldsymbol{\zeta}} - \overline{\boldsymbol{\zeta}})) \cdot \boldsymbol{\omega}^\delta\right) \mathrm{d}S + \int_{\Gamma_N} (g(\underline{\vartheta}) - g(\overline{\vartheta}))\theta^\delta \,\mathrm{d}S \tag{4.11a}$$

$$+ \int_\Omega \kappa(\underline{\vartheta})(\nabla\underline{\vartheta} - \nabla\overline{\vartheta}) \cdot \nabla\theta^\delta + \varepsilon(\nabla\underline{\boldsymbol{\zeta}} - \nabla\overline{\boldsymbol{\zeta}}) : \nabla\boldsymbol{\omega}^\delta + (\boldsymbol{f}(\underline{\vartheta}, \underline{\boldsymbol{\zeta}}) - \boldsymbol{f}(\overline{\vartheta}, \overline{\boldsymbol{\zeta}})) \cdot (\theta^\delta \rho \boldsymbol{L} - \boldsymbol{\omega}^\delta) \,\mathrm{d}\boldsymbol{x} \tag{4.11b}$$

$$\leq \int_\Omega (\underline{\vartheta} - \overline{\vartheta})(\boldsymbol{v} \cdot \nabla)\theta^\delta + (\underline{\boldsymbol{\zeta}} - \overline{\boldsymbol{\zeta}}) \cdot (\boldsymbol{v} \cdot \nabla)\boldsymbol{\omega}^\delta - (\kappa(\underline{\vartheta}) - \kappa(\overline{\vartheta}))\nabla\overline{\vartheta} \cdot \nabla\theta^\delta - (\underline{\vartheta} - \overline{\vartheta})\boldsymbol{a} \cdot \nabla\theta^\delta \,\mathrm{d}\boldsymbol{x}\,. \tag{4.11c}$$

Due to the assumptions on $\boldsymbol{v}$ on the boundary, the order of the elements on the Dirichlet part, and the monotony of g, all boundary terms in line (4.11a) are positive.

For every $\delta > 0$, we introduce the sets

$$\Omega_0^\theta := \{\boldsymbol{x} \in \Omega | \underline{\vartheta}(\boldsymbol{x}) > \overline{\vartheta}(\boldsymbol{x})\}\,, \qquad \Omega_\delta^\theta := \{\boldsymbol{x} \in \Omega_0^\theta | \underline{\vartheta}(\boldsymbol{x}) - \overline{\vartheta}(\boldsymbol{x}) > \delta\}\,, \tag{4.12a}$$

$$\Omega_0^i := \{\boldsymbol{x} \in \Omega | \underline{\boldsymbol{\zeta}}_i(\boldsymbol{x}) > \overline{\boldsymbol{\zeta}}_i(\boldsymbol{x})\}\,, \qquad \Omega_\delta^i := \{\boldsymbol{x} \in \Omega_0^i | \rho \boldsymbol{L}_i(\underline{\boldsymbol{\zeta}}_i(\boldsymbol{x}) - \overline{\boldsymbol{\zeta}}_i(\boldsymbol{x})) > \delta\}\,. \tag{4.12b}$$

We observe that $\Omega_\delta^\theta \nearrow \Omega_0^\theta$ and $\Omega_\delta^i \nearrow \Omega_0^i$ for $i \in \{1, \dots, m\}$ as $\delta \searrow 0$. Further, we observe that $\operatorname{supp}(\theta^\delta) = \Omega_0^\theta$ and $\operatorname{supp}(\boldsymbol{\omega}_i^\delta) = \Omega_0^i$ as well as $\operatorname{supp}(\nabla\theta^\delta) = \Omega_0^\theta / \Omega_\delta^\theta$ and $\operatorname{supp}(\nabla\boldsymbol{\omega}_i^\delta) = \Omega_0^i / \Omega_\delta^i$ for $i \in \{1, \dots, m\}$.

The last observation allow us to conclude that

$$\begin{aligned}\int_\Omega \kappa(\underline{\vartheta})(\nabla\underline{\vartheta}-\nabla\overline{\vartheta})\cdot\nabla\theta^\delta+\varepsilon(\nabla\underline{\boldsymbol{\zeta}}-\nabla\overline{\boldsymbol{\zeta}}):\nabla\boldsymbol{\omega}^\delta\,\mathrm{d}\,\boldsymbol{x} &= \int_{\Omega_0^\theta/\Omega_\delta^\theta}\kappa(\underline{\vartheta})|\nabla\theta^\delta|^2\,\mathrm{d}\,\boldsymbol{x}\\ &\quad+\sum_{i=1}^m\int_{\Omega_0^i/\Omega_\delta^i}\varepsilon|\nabla\boldsymbol{\omega}_i^\delta|^2\,\mathrm{d}\,\boldsymbol{x}\\ &\geq \underline{\kappa}\|\nabla\theta^\delta\|_{L^2}^2+\varepsilon\|\nabla\boldsymbol{\omega}^\delta\|_{L^2}^2\,.\end{aligned}\tag{4.13}$$

Similarly, we find for the right-hand side (4.11c) that

$$\begin{aligned}&\int_\Omega(\underline{\vartheta}-\overline{\vartheta})(\boldsymbol{v}\cdot\nabla)\theta^\delta+(\underline{\boldsymbol{\zeta}}-\overline{\boldsymbol{\zeta}})\cdot(\boldsymbol{v}\cdot\nabla)\boldsymbol{\omega}^\delta-(\kappa(\underline{\vartheta})-\kappa(\overline{\vartheta}))\nabla\overline{\vartheta}\cdot\nabla\theta^\delta-(\underline{\vartheta}-\overline{\vartheta})\boldsymbol{a}\cdot\nabla\theta^\delta\,\mathrm{d}\,\boldsymbol{x}\\
&=\int_{\Omega_0^\theta/\Omega_\delta^\theta}(\underline{\vartheta}-\overline{\vartheta})(\boldsymbol{v}\cdot\nabla)\theta^\delta-(\kappa(\underline{\vartheta})-\kappa(\overline{\vartheta}))\nabla\overline{\vartheta}\cdot\nabla\theta^\delta-(\underline{\vartheta}-\overline{\vartheta})\boldsymbol{a}\cdot\nabla\theta^\delta\,\mathrm{d}\,\boldsymbol{x}\\
&\quad+\sum_{i=1}^m\int_{\Omega_0^i/\Omega_\delta^i}(\underline{\boldsymbol{\zeta}}_i-\overline{\boldsymbol{\zeta}}_i)(\boldsymbol{v}\cdot\nabla)\boldsymbol{\omega}_i^\delta\,\mathrm{d}\,\boldsymbol{x}\\
&\leq\delta(1+\|\kappa'\|_\infty)\left(\int_{\Omega_0^\theta/\Omega_\delta^\theta}|\boldsymbol{v}|^2+|\nabla\overline{\vartheta}|^2+|\boldsymbol{a}|^2\,\mathrm{d}\,\boldsymbol{x}\right)^{1/2}\|\nabla\theta^\delta\|_{L^2}\\
&\quad+\delta\sum_{i=1}^m\left(\int_{\Omega_0^i/\Omega_\delta^i}\rho^2\boldsymbol{L}_i^2|\boldsymbol{v}|^2\,\mathrm{d}\,\boldsymbol{x}\right)^{1/2}\|\nabla\boldsymbol{\omega}_i^\delta\|_{L^2}\,.\end{aligned}\tag{4.14}$$

It remains to estimate the nonlinear coupling function $\boldsymbol{f}$. Inserting the definition of $\boldsymbol{f}$, we observe

$$\begin{aligned}(\boldsymbol{f}(\underline{\vartheta},\underline{\boldsymbol{\zeta}})-\boldsymbol{f}(\overline{\vartheta},\overline{\boldsymbol{\zeta}})) &= (\tilde{\boldsymbol{f}}(\boldsymbol{\zeta}_{\mathrm{eq}}(\underline{\vartheta})-\underline{\boldsymbol{\zeta}})-\tilde{\boldsymbol{f}}(\boldsymbol{\zeta}_{\mathrm{eq}}(\overline{\vartheta})-\overline{\boldsymbol{\zeta}}))\\
&=\sum_{i=1}^m\int_{(\zeta_{\mathrm{eq}_i}(\overline{\vartheta})-\overline{\zeta}_i)}^{(\zeta_{\mathrm{eq}_i}(\underline{\vartheta})-\underline{\zeta}_i)}\tilde{\boldsymbol{f}}_i'(s)\,\mathrm{d}\,s\left((\boldsymbol{\zeta}_{\mathrm{eq}_i}(\underline{\vartheta})-\boldsymbol{\zeta}_{\mathrm{eq}_i}(\overline{\vartheta}))-(\underline{\boldsymbol{\zeta}}_i-\overline{\boldsymbol{\zeta}}_i)\right).\end{aligned}$$

We define $\boldsymbol{h}_i:=\int_{(\zeta_{\mathrm{eq}_i}(\overline{\vartheta})-\overline{\zeta}_i)}^{(\zeta_{\mathrm{eq}_i}(\underline{\vartheta})-\underline{\zeta}_i)}\tilde{\boldsymbol{f}}_i'(s)\,\mathrm{d}\,s$ and keep in mind that this function is non-negative according to Assumption 1. Using this generalized fundamental lemma of differential and integral calculus, we find for the considered term

$$\begin{aligned}&\int_\Omega(\boldsymbol{f}(\underline{\vartheta},\underline{\boldsymbol{\zeta}})-\boldsymbol{f}(\overline{\vartheta},\overline{\boldsymbol{\zeta}}))\cdot(\theta^\delta\rho\boldsymbol{L}-\boldsymbol{\omega}^\delta)\,\mathrm{d}\,\boldsymbol{x}\\
&=\int_\Omega\sum_{i=1}^m\boldsymbol{h}_i\left((\boldsymbol{\zeta}_{\mathrm{eq}_i}(\underline{\vartheta})-\boldsymbol{\zeta}_{\mathrm{eq}_i}(\overline{\vartheta}))-(\underline{\boldsymbol{\zeta}}_i-\overline{\boldsymbol{\zeta}}_i)\right)(\theta^\delta\rho\boldsymbol{L}_i-\boldsymbol{\omega}_i^\delta)\,\mathrm{d}\,\boldsymbol{x}\\
&=\int_\Omega\sum_{i=1}^m\boldsymbol{h}_i\left(\rho\boldsymbol{L}_i(\boldsymbol{\zeta}_{\mathrm{eq}_i}(\underline{\vartheta})-\boldsymbol{\zeta}_{\mathrm{eq}_i}(\overline{\vartheta}))\theta^\delta+(\underline{\boldsymbol{\zeta}}_i-\overline{\boldsymbol{\zeta}}_i)\boldsymbol{\omega}_i^\delta\right)\mathrm{d}\,\boldsymbol{x}\\
&\quad-\int_\Omega\sum_{i=1}^m\boldsymbol{h}_i\left((\boldsymbol{\zeta}_{\mathrm{eq}_i}(\underline{\vartheta})-\boldsymbol{\zeta}_{\mathrm{eq}_i}(\overline{\vartheta}))\boldsymbol{\omega}_i^\delta+(\underline{\boldsymbol{\zeta}}_i-\overline{\boldsymbol{\zeta}}_i)\theta^\delta\rho\boldsymbol{L}_i\right)\mathrm{d}\,\boldsymbol{x}.\end{aligned}\tag{4.15}$$

We consider the last line further on. Inserting the definitions of $\boldsymbol{\omega}^\delta$ and θ^δ, we may observe

$$
\begin{aligned}
&- \int_\Omega \sum_{i=1}^m \boldsymbol{h}_i \left((\boldsymbol{\zeta}_{\mathrm{eq}_i}(\underline{\vartheta}) - \boldsymbol{\zeta}_{\mathrm{eq}_i}(\overline{\vartheta}))\boldsymbol{\omega}_i^\delta + (\underline{\boldsymbol{\zeta}}_i - \overline{\boldsymbol{\zeta}}_i)\theta^\delta \rho \boldsymbol{L}_i \right) \mathrm{d}\,\boldsymbol{x} \\
&= -\sum_{i=1}^m \int_{\Omega_0^i} \boldsymbol{h}_i \left((\boldsymbol{\zeta}_{\mathrm{eq}_i}(\underline{\vartheta}) - \boldsymbol{\zeta}_{\mathrm{eq}_i}(\overline{\vartheta}))\boldsymbol{\omega}_i^\delta \right) \mathrm{d}\,\boldsymbol{x} - \sum_{i=1}^m \rho \boldsymbol{L}_i \boldsymbol{h}_i \int_{\Omega_0^\theta} \left(\underline{\boldsymbol{\zeta}}_i - \overline{\boldsymbol{\zeta}}_i \right) \theta^\delta \,\mathrm{d}\,\boldsymbol{x} \\
&\geq -\sum_{i=1}^m \int_{\Omega_0^i \cap \Omega_0^\theta} \boldsymbol{h}_i \left((\boldsymbol{\zeta}_{\mathrm{eq}_i}(\underline{\vartheta}) - \boldsymbol{\zeta}_{\mathrm{eq}_i}(\overline{\vartheta}))\boldsymbol{\omega}_i^\delta \right) \mathrm{d}\,\boldsymbol{x} - \sum_{i=1}^m \rho \boldsymbol{L}_i \int_{\Omega_0^\theta \cap \Omega_0^i} \boldsymbol{h}_i \left(\underline{\boldsymbol{\zeta}}_i - \overline{\boldsymbol{\zeta}}_i \right) \theta^\delta \,\mathrm{d}\,\boldsymbol{x}\,,
\end{aligned}
$$

where the equality holds due to the support of the functions $\boldsymbol{\omega}_i^\delta$ and θ^δ and the inequality holds since the functions under the integral, i.e., $\boldsymbol{h}_i(\boldsymbol{\zeta}_{\mathrm{eq}_i}(\underline{\vartheta}) - \boldsymbol{\zeta}_{\mathrm{eq}_i}(\overline{\vartheta}))\boldsymbol{\omega}_i^\delta$ and $\boldsymbol{h}_i \left(\underline{\boldsymbol{\zeta}}_i - \overline{\boldsymbol{\zeta}}_i \right) \theta^\delta$, are negative on the sets $\Omega_0^i/\Omega_0^\theta$ and $\Omega_0^\theta/\Omega_0^i$, respectively. We further decompose the right-hand side, implying

$$
\begin{aligned}
&-\sum_{i=1}^m \int_{\Omega_0^i \cap \Omega_0^\theta} \boldsymbol{h}_i \left((\boldsymbol{\zeta}_{\mathrm{eq}_i}(\underline{\vartheta}) - \boldsymbol{\zeta}_{\mathrm{eq}_i}(\overline{\vartheta}))\boldsymbol{\omega}_i^\delta \right) \mathrm{d}\,\boldsymbol{x} - \sum_{i=1}^m \rho \boldsymbol{L}_i \int_{\Omega_0^\theta \cap \Omega_0^i} \boldsymbol{h}_i \left(\underline{\boldsymbol{\zeta}}_i - \overline{\boldsymbol{\zeta}}_i \right) \theta^\delta \,\mathrm{d}\,\boldsymbol{x} \\
&= -\sum_{i=1}^m \int_{\Omega_0^i \cap \Omega_0^\theta / \Omega_\delta^\theta} \boldsymbol{h}_i \left((\boldsymbol{\zeta}_{\mathrm{eq}_i}(\underline{\vartheta}) - \boldsymbol{\zeta}_{\mathrm{eq}_i}(\overline{\vartheta}))\boldsymbol{\omega}_i^\delta \right) \mathrm{d}\,\boldsymbol{x} - \sum_{i=1}^m \rho \boldsymbol{L}_i \int_{\Omega_0^\theta \cap \Omega_0^i / \Omega_\delta^i} \boldsymbol{h}_i \left(\underline{\boldsymbol{\zeta}}_i - \overline{\boldsymbol{\zeta}}_i \right) \theta^\delta \,\mathrm{d}\,\boldsymbol{x} \\
&\quad -\sum_{i=1}^m \int_{\Omega_0^i \cap \Omega_\delta^\theta} \boldsymbol{h}_i \left((\boldsymbol{\zeta}_{\mathrm{eq}_i}(\underline{\vartheta}) - \boldsymbol{\zeta}_{\mathrm{eq}_i}(\overline{\vartheta}))\boldsymbol{\omega}_i^\delta \right) \mathrm{d}\,\boldsymbol{x} - \sum_{i=1}^m \rho \boldsymbol{L}_i \int_{\Omega_0^\theta \cap \Omega_\delta^i} \boldsymbol{h}_i \left(\underline{\boldsymbol{\zeta}}_i - \overline{\boldsymbol{\zeta}}_i \right) \theta^\delta \,\mathrm{d}\,\boldsymbol{x}\,.
\end{aligned}
$$

We consider the last line of the previous equation, the definitions of $\boldsymbol{\omega}^\delta$ and θ^δ imply

$$
\begin{aligned}
&-\sum_{i=1}^m \int_{\Omega_0^i \cap \Omega_\delta^\theta} \boldsymbol{h}_i \left((\boldsymbol{\zeta}_{\mathrm{eq}_i}(\underline{\vartheta}) - \boldsymbol{\zeta}_{\mathrm{eq}_i}(\overline{\vartheta}))\boldsymbol{\omega}_i^\delta \right) \mathrm{d}\,\boldsymbol{x} - \sum_{i=1}^m \rho \boldsymbol{L}_i \int_{\Omega_0^\theta \cap \Omega_\delta^i} \boldsymbol{h}_i \left(\underline{\boldsymbol{\zeta}}_i - \overline{\boldsymbol{\zeta}}_i \right) \theta^\delta \,\mathrm{d}\,\boldsymbol{x} \\
&\geq -\sum_{i=1}^m \int_{\Omega_0^i \cap \Omega_\delta^\theta} \boldsymbol{h}_i \left((\boldsymbol{\zeta}_{\mathrm{eq}_i}(\underline{\vartheta}) - \boldsymbol{\zeta}_{\mathrm{eq}_i}(\overline{\vartheta}))\delta \right) \mathrm{d}\,\boldsymbol{x} - \sum_{i=1}^m \rho \boldsymbol{L}_i \int_{\Omega_0^\theta \cap \Omega_\delta^i} \boldsymbol{h}_i \left(\underline{\boldsymbol{\zeta}}_i - \overline{\boldsymbol{\zeta}}_i \right) \delta \,\mathrm{d}\,\boldsymbol{x} \\
&\geq -\sum_{i=1}^m \int_{\Omega_0^i \cap \Omega_\delta^\theta} \rho \boldsymbol{L}_i \boldsymbol{h}_i \left((\boldsymbol{\zeta}_{\mathrm{eq}_i}(\underline{\vartheta}) - \boldsymbol{\zeta}_{\mathrm{eq}_i}(\overline{\vartheta}))\theta^\delta \right) \mathrm{d}\,\boldsymbol{x} - \sum_{i=1}^m \int_{\Omega_0^\theta \cap \Omega_\delta^i} \boldsymbol{h}_i \left(\underline{\boldsymbol{\zeta}}_i - \overline{\boldsymbol{\zeta}}_i \right) \boldsymbol{\omega}_i^\delta \,\mathrm{d}\,\boldsymbol{x}\,,
\end{aligned}
$$

since $\boldsymbol{\omega}_i^\delta \leq \rho \boldsymbol{L}_i \delta = \rho \boldsymbol{L}_i \theta^\delta$ on $\Omega_0^i \cap \Omega_\delta^\theta$ and $\rho \boldsymbol{L}_i \theta^\delta \leq \rho \boldsymbol{L}_i \delta = \boldsymbol{\omega}_i^\delta$ on $\Omega_0^\theta \cap \Omega_\delta^i$ for all $i \in \{1, \ldots, m\}$.

Inserting everything back into (4.15), we conclude

$$
\begin{aligned}
&\int_\Omega (\boldsymbol{f}(\underline{\vartheta}, \underline{\boldsymbol{\zeta}}) - \boldsymbol{f}(\overline{\vartheta}, \overline{\boldsymbol{\zeta}})) \cdot (\theta^\delta \rho \boldsymbol{L} - \boldsymbol{\omega}^\delta) \,\mathrm{d}\,\boldsymbol{x} \\
&\geq \sum_{i=1}^m \left(\int_{\Omega_0^\theta} \rho \boldsymbol{L}_i \boldsymbol{h}_i (\boldsymbol{\zeta}_{\mathrm{eq}_i}(\underline{\vartheta}) - \boldsymbol{\zeta}_{\mathrm{eq}_i}(\overline{\vartheta}))\theta^\delta \,\mathrm{d}\,\boldsymbol{x} + \int_{\Omega_0^i} \boldsymbol{h}_i (\underline{\boldsymbol{\zeta}}_i - \overline{\boldsymbol{\zeta}}_i)\boldsymbol{\omega}_i^\delta \,\mathrm{d}\,\boldsymbol{x} \right) \\
&\quad -\sum_{i=1}^m \int_{\Omega_0^i \cap \Omega_0^\theta / \Omega_\delta^\theta} \boldsymbol{h}_i \left((\boldsymbol{\zeta}_{\mathrm{eq}_i}(\underline{\vartheta}) - \boldsymbol{\zeta}_{\mathrm{eq}_i}(\overline{\vartheta}))\boldsymbol{\omega}_i^\delta \right) \mathrm{d}\,\boldsymbol{x} - \sum_{i=1}^m \rho \boldsymbol{L}_i \int_{\Omega_0^\theta \cap \Omega_0^i / \Omega_\delta^i} \boldsymbol{h}_i \left(\underline{\boldsymbol{\zeta}}_i - \overline{\boldsymbol{\zeta}}_i \right) \theta^\delta \,\mathrm{d}\,\boldsymbol{x} \\
&\quad -\sum_{i=1}^m \int_{\Omega_0^i \cap \Omega_\delta^\theta} \rho \boldsymbol{L}_i \boldsymbol{h}_i \left((\boldsymbol{\zeta}_{\mathrm{eq}_i}(\underline{\vartheta}) - \boldsymbol{\zeta}_{\mathrm{eq}_i}(\overline{\vartheta}))\theta^\delta \right) \mathrm{d}\,\boldsymbol{x} - \sum_{i=1}^m \int_{\Omega_0^\theta \cap \Omega_\delta^i} \boldsymbol{h}_i \left(\underline{\boldsymbol{\zeta}}_i - \overline{\boldsymbol{\zeta}}_i \right) \boldsymbol{\omega}_i^\delta \,\mathrm{d}\,\boldsymbol{x} \\
&\geq \sum_{i=1}^m \left(\int_{\Omega_0^\theta / (\Omega_0^i \cap \Omega_\delta^\theta)} \rho \boldsymbol{L}_i \boldsymbol{h}_i (\boldsymbol{\zeta}_{\mathrm{eq}_i}(\underline{\vartheta}) - \boldsymbol{\zeta}_{\mathrm{eq}_i}(\overline{\vartheta}))\theta^\delta \,\mathrm{d}\,\boldsymbol{x} + \int_{\Omega_0^i / (\Omega_0^\theta \cap \Omega_\delta^i)} \boldsymbol{h}_i (\underline{\boldsymbol{\zeta}}_i - \overline{\boldsymbol{\zeta}}_i)\boldsymbol{\omega}_i^\delta \,\mathrm{d}\,\boldsymbol{x} \right) \\
&\quad -\sum_{i=1}^m \int_{\Omega_0^i \cap \Omega_0^\theta / \Omega_\delta^\theta} \boldsymbol{h}_i \left((\boldsymbol{\zeta}_{\mathrm{eq}_i}(\underline{\vartheta}) - \boldsymbol{\zeta}_{\mathrm{eq}_i}(\overline{\vartheta}))\boldsymbol{\omega}_i^\delta \right) \mathrm{d}\,\boldsymbol{x} - \sum_{i=1}^m \rho \boldsymbol{L}_i \int_{\Omega_0^\theta \cap \Omega_0^i / \Omega_\delta^i} \boldsymbol{h}_i \left(\underline{\boldsymbol{\zeta}}_i - \overline{\boldsymbol{\zeta}}_i \right) \theta^\delta \,\mathrm{d}\,\boldsymbol{x}\,.
\end{aligned}
$$

The first line on the right-hand side of the previous inequality is positive such that we can estimate it from below by zero. Estimating the other terms appropriately, we find

$$\begin{aligned}
&\int_\Omega (\boldsymbol{f}(\underline{\vartheta},\underline{\boldsymbol{\zeta}}) - \boldsymbol{f}(\overline{\vartheta},\overline{\boldsymbol{\zeta}})) \cdot (\theta^\delta \rho \boldsymbol{L} - \boldsymbol{\omega}^\delta) \,\mathrm{d}\boldsymbol{x} \\
&\geq -\sum_{i=1}^m \int_{\Omega_0^i \cap \Omega_0^\theta / \Omega_\delta^\theta} \boldsymbol{h}_i \left((\boldsymbol{\zeta}_{\mathrm{eq}_i}(\underline{\vartheta}) - \boldsymbol{\zeta}_{\mathrm{eq}_i}(\overline{\vartheta}))\boldsymbol{\omega}_i^\delta \right) \mathrm{d}\boldsymbol{x} - \sum_{i=1}^m \rho \boldsymbol{L}_i \int_{\Omega_0^\theta \cap \Omega_0^i / \Omega_\delta^i} \boldsymbol{h}_i \left(\underline{\boldsymbol{\zeta}}_i - \overline{\boldsymbol{\zeta}}_i \right) \theta^\delta \,\mathrm{d}\boldsymbol{x} \\
&\geq -\delta \|\boldsymbol{\zeta}_{\mathrm{eq}}'\|_\infty \sum_{i=1}^m \left(\int_{\Omega_0^i \cap \Omega_0^\theta / \Omega_\delta^\theta} \left(\max_i \boldsymbol{h}_i \right)^2 \mathrm{d}\boldsymbol{x} \right)^{1/2} \|\boldsymbol{\omega}_i^\delta\|_{L^2} \\
&\quad - \delta \sum_{i=1}^m \left(\int_{\Omega_0^\theta \cap \Omega_0^i / \Omega_\delta^i} (\max_i \boldsymbol{h}_i)^2 \right)^{1/2} \|\theta^\delta\|_{L^2} \,.
\end{aligned} \tag{4.16}$$

Collecting now the estimates (4.13), (4.14), and (4.16) and combining them with (4.11) implies

$$\begin{aligned}
\underline{\kappa} \|\nabla \theta^\delta\|_{L^2}^2 + \varepsilon \|\nabla \boldsymbol{\omega}^\delta\|_{L^2}^2 \leq{}& \delta (1 + \|\kappa'\|_\infty) \left(\int_{\Omega_0^\theta / \Omega_\delta^\theta} |\boldsymbol{v}|^2 + |\nabla \overline{\vartheta}|^2 + |\boldsymbol{a}|^2 \,\mathrm{d}\boldsymbol{x} \right)^{1/2} \|\nabla \theta^\delta\|_{L^2} \\
&+ \delta \sum_{i=1}^m \left(\int_{\Omega_0^i / \Omega_\delta^i} \rho^2 L_i^2 |\boldsymbol{v}|^2 \,\mathrm{d}\boldsymbol{x} \right)^{1/2} \|\nabla \boldsymbol{\omega}_i^\delta\|_{L^2} \\
&+ \delta \|\boldsymbol{\zeta}_{\mathrm{eq}}'\|_\infty \sum_{i=1}^m \left(\int_{\Omega_0^i \cap \Omega_0^\theta / \Omega_\delta^\theta} \left(\max_i \boldsymbol{h}_i \right)^2 \mathrm{d}\boldsymbol{x} \right)^{1/2} \|\boldsymbol{\omega}_i^\delta\|_{L^2} \\
&+ \delta \sum_{i=1}^m \left(\int_{\Omega_0^\theta \cap \Omega_0^i / \Omega_\delta^i} (\max_i \boldsymbol{h}_i)^2 \right)^{1/2} \|\theta^\delta\|_{L^2} \,.
\end{aligned}$$

Poincaré's inequality allows us to conclude

$$\begin{aligned}
&\mathrm{meas}(\Omega_\delta^\theta) + \sum_{i=1}^m \mathrm{meas}(\Omega_\delta^i) \\
&\leq \frac{1}{\delta} \left(\left(\int_{\Omega_\delta^\theta} \delta^2 \,\mathrm{d}\boldsymbol{x} \right)^{1/2} + \sum_{i=1}^m \left(\int_{\Omega_\delta^i} \rho^2 \boldsymbol{L}_i^2 \delta^2 \,\mathrm{d}\boldsymbol{x} \right)^{1/2} \right) \leq \frac{1}{\delta} \left(\|\theta^\delta\|_{L^2} + \|\boldsymbol{\omega}^\delta\|_{L^2} \right) \\
&\leq c \frac{1}{\delta} \left(\underline{\kappa} \|\nabla \theta^\delta\|_{L^2} + \varepsilon \|\nabla \boldsymbol{\omega}^\delta\|_{L^2} \right) \\
&\leq c \left(\int_{\Omega_0^\theta / \Omega_\delta^\theta} |\boldsymbol{v}|^2 + |\nabla \overline{\vartheta}|^2 + |\boldsymbol{a}|^2 \,\mathrm{d}\boldsymbol{x} \right)^{1/2} + c \sum_{i=1}^m \left(\int_{\Omega_0^i / \Omega_\delta^i} \rho^2 L_i^2 |\boldsymbol{v}|^2 \,\mathrm{d}\boldsymbol{x} \right)^{1/2} \\
&\quad + c \sum_{i=1}^m \left(\int_{\Omega_0^i \cap \Omega_0^\theta / \Omega_\delta^\theta} \left(\max_i \boldsymbol{h}_i \right)^2 \mathrm{d}\boldsymbol{x} \right)^{1/2} + c \sum_{i=1}^m \left(\int_{\Omega_0^\theta \cap \Omega_0^i / \Omega_\delta^i} (\max_i \boldsymbol{h}_i)^2 \right)^{1/2} .
\end{aligned}$$

The integrability of $\boldsymbol{v}$, $\nabla \overline{\vartheta}$, $\boldsymbol{a}$, and $(\max_i \boldsymbol{h}_i)$ grants that the right-hand side of the previous inequality vanishes as $\delta \to 0$. This let us conclude that $\mathrm{meas}(\Omega_\delta^\theta) + \sum_{i=1}^m \mathrm{meas}(\Omega_\delta^i) \to 0$ as $\delta \to 0$ which implies $\mathrm{meas}(\Omega_0^\theta) + \sum_{i=1}^m \mathrm{meas}(\Omega_0^i) = 0$ and therewith, the assertion. □

Now, after having provided a comparison criterion useful for the uniqueness stated in Theorem 3, we go back to the proof of Theorem 3 which asserts the existence and uniqueness of a weak solution (Def. 2) of the system (4.6).

Proof. Existence: We want to employ a fixed-point technique based on Schauder's fixed point. Therefore, we define the mapping

$$\mathcal{T} : L^2_R \to L^2_R\,, \quad \text{where } L^2_R := \{u \in L^2(\Omega); \|u\|_{L^2} \le R\}\,.$$

The operator $\mathcal{T}$ maps $(\overline{\vartheta})$ to the solution ϑ of the system

$$(\boldsymbol{v}\cdot\nabla)\vartheta - \nabla\cdot(\kappa(\vartheta)\nabla\vartheta) + \rho\boldsymbol{L}\cdot\boldsymbol{f}(\vartheta,\boldsymbol{\zeta}) = q \qquad \text{in } \Omega\,, \tag{4.17a}$$

$$\boldsymbol{n}\cdot\kappa(\vartheta)\nabla\vartheta = g(\vartheta) \qquad \text{on } \Gamma_N\,, \tag{4.17b}$$

$$\vartheta = 0 \qquad \text{on } \Gamma_D\,, \tag{4.17c}$$

$$(\boldsymbol{v}\cdot\nabla)\boldsymbol{\zeta} - \varepsilon\Delta\boldsymbol{\zeta} = \boldsymbol{f}(\overline{\vartheta},\boldsymbol{\zeta}) \qquad \text{in } \Omega\,, \tag{4.17d}$$

$$\boldsymbol{n}\cdot\nabla\boldsymbol{\zeta} = \boldsymbol{0} \qquad \text{on } \Gamma_N\,, \tag{4.17e}$$

$$\boldsymbol{\zeta} = \boldsymbol{0} \qquad \text{on } \Gamma_D\,. \tag{4.17f}$$

Note that the coupling between both is removed in the sense that we can now first solve (4.17d) to attain $\boldsymbol{\zeta}$ and insert this function in (4.17a) in order to find ϑ, the image of the mapping $\mathcal{T}$. Considering the operator $\mathcal{A}_{\overline{\vartheta}}$ associated to (4.17d),

$$\langle \mathcal{A}_{\overline{\vartheta}}(\boldsymbol{\zeta}), \boldsymbol{\psi}\rangle := \int_\Omega (\boldsymbol{v}\cdot\nabla)\boldsymbol{\zeta}\cdot\boldsymbol{\psi} + \varepsilon\nabla\boldsymbol{\zeta} : \nabla\boldsymbol{\psi} - \boldsymbol{f}(\overline{\vartheta},\boldsymbol{\zeta})\cdot\boldsymbol{\psi}\,\mathrm{d}\,\boldsymbol{x}\,. \tag{4.18}$$

It is a routine matter to show that $\mathcal{A}_{\overline{\vartheta}} : H^1_{\Gamma_D}(\Omega)^m \to (H^1_{\Gamma_D}(\Omega)^m)^*$ is a continuous and pseudomonotone mapping.

Additionally, using $\varphi = \vartheta$ as test function in (4.18), we may infer

$$\begin{aligned}
\langle \mathcal{A}_{\overline{\vartheta}}(\boldsymbol{\zeta}), \boldsymbol{\zeta}\rangle &= \int_\Omega (\boldsymbol{v}\cdot\nabla)\boldsymbol{\zeta}\cdot\boldsymbol{\zeta} + \varepsilon\nabla\boldsymbol{\zeta} : \nabla\boldsymbol{\zeta} - \boldsymbol{f}(\overline{\vartheta},\boldsymbol{\zeta})\cdot\boldsymbol{\zeta}\,\mathrm{d}\,\boldsymbol{x} \\
&= \int_\Omega \frac{1}{2}(\boldsymbol{v}\cdot\nabla)|\boldsymbol{\zeta}|^2 + \varepsilon|\nabla\boldsymbol{\zeta}|^2 - \tilde{\boldsymbol{f}}(-\boldsymbol{\zeta})\cdot\boldsymbol{\zeta} - \boldsymbol{\zeta}_{\mathrm{eq}}(\overline{\vartheta})\int_0^1 \nabla\tilde{\boldsymbol{f}}(-\boldsymbol{\zeta} + s\boldsymbol{\zeta}_{\mathrm{eq}}(\overline{\vartheta}))\,\mathrm{d}\,s\boldsymbol{\zeta}\,\mathrm{d}\,\boldsymbol{x} \\
&\ge \int_{\Gamma_N} \frac{1}{2}\boldsymbol{v}\cdot\boldsymbol{n}|\boldsymbol{\zeta}|^2\,\mathrm{d}\,S + \varepsilon\int_\Omega |\nabla\boldsymbol{\zeta}|^2\,\mathrm{d}\,\boldsymbol{x} - C\int_\Omega |\boldsymbol{\zeta}|\,\mathrm{d}\,\boldsymbol{x}\,.
\end{aligned}$$

that $\mathcal{A}_{\overline{\vartheta}}$ is coercive, which guarantees that $\mathcal{A}_{\overline{\vartheta}}$ is surjective. Additionally, we find a constant such that $\|\boldsymbol{\zeta}\|_{H^1_{\Gamma_D}} \le C$ for any $\overline{\vartheta} \in L^2_R$. The inequality is achieved by applying an integration-by-parts formula

$$\int_\Omega \frac{1}{2}(\boldsymbol{v}\cdot\nabla)|\boldsymbol{\zeta}|^2\,\mathrm{d}\,\boldsymbol{x} = \int_{\Gamma_N}\frac{1}{2}\boldsymbol{v}\cdot\boldsymbol{n}|\boldsymbol{\zeta}|^2\,\mathrm{d}\,S - \int_\Omega \frac{1}{2}\mathrm{div}\,\boldsymbol{v}|\boldsymbol{\zeta}|^2\,\mathrm{d}\,\boldsymbol{x} \tag{4.19}$$

and the fundamental theorem of differentiation and integration on $\tilde{\boldsymbol{f}}$

$$\tilde{\boldsymbol{f}}(\boldsymbol{\zeta}_{eq}(\overline{\vartheta}) - \boldsymbol{\zeta}) - \tilde{\boldsymbol{f}}(-\boldsymbol{\zeta}) = \boldsymbol{\zeta}_{\mathrm{eq}}(\overline{\vartheta})\int_0^1 \nabla\tilde{\boldsymbol{f}}(s\boldsymbol{\zeta}_{\mathrm{eq}} - \boldsymbol{\zeta}(\overline{\vartheta}))\,\mathrm{d}\,s. \tag{4.20}$$

The uniqueness of solutions to (4.17d) is a consequence of the monotony of $\tilde{\boldsymbol{f}}$.

To show the continuity of the mapping $\mathcal{T}$, we consider the operator $\mathcal{H}_{\boldsymbol{\zeta}} : H^1_{\Gamma_D}(\Omega) \to H^{-1}_{\Gamma_D}(\Omega)$ given by

$$\langle \mathcal{H}_{\boldsymbol{\zeta}}(\vartheta), \varphi \rangle := \int_\Omega (\boldsymbol{v} \cdot \nabla)\vartheta\varphi + \kappa(\vartheta)\nabla\vartheta \cdot \nabla\varphi + \rho\boldsymbol{L} \cdot \boldsymbol{f}(\vartheta, \boldsymbol{\zeta})\varphi \,\mathrm{d}\,\boldsymbol{x} + \int_{\Gamma_N} g(\vartheta)\varphi \,\mathrm{d}\,S\,. \tag{4.21}$$

This operator is bijective, i.e., for every $q \in H^{-1}_{\Gamma_D}$ there exists a unique solution $\vartheta \in H^1_{\Gamma_D}$ such that $\mathcal{H}_{\boldsymbol{\zeta}}(\vartheta) = q$ in $H^{-1}_{\Gamma_D}$. Indeed, the existence follows from standard arguments concerning pseudomonotone mappings (see for instance Roubíček [50, Thm. 2.36]). Here, we only concentrate on the coercivity of the operator, since the pseudomonotony is fairly standard. Using $\varphi = \vartheta$ as test function in (4.21), we may infer

$$\begin{aligned}
\langle \mathcal{H}_{\boldsymbol{\zeta}}(\vartheta), \vartheta \rangle &= \int_\Omega \frac{1}{2}(\boldsymbol{v} \cdot \nabla)|\vartheta|^2 + \kappa(\vartheta)|\nabla\vartheta|^2 + \rho\boldsymbol{L} \cdot \boldsymbol{f}(\vartheta, \boldsymbol{\zeta})\vartheta \,\mathrm{d}\,\boldsymbol{x} + \int_{\Gamma_N} g(\vartheta)\vartheta \,\mathrm{d}\,S \\
&\geq \int_\Omega \kappa(\vartheta)|\nabla\vartheta|^2 + \rho\boldsymbol{L}\tilde{\boldsymbol{f}}(\boldsymbol{\zeta}_{\mathrm{eq}}(\vartheta))\vartheta - \rho\boldsymbol{L} \cdot \int_0^1 \nabla\tilde{\boldsymbol{f}}(\boldsymbol{\zeta}_{\mathrm{eq}}(\vartheta) - s\boldsymbol{\zeta}) \,\mathrm{d}\, s\boldsymbol{\zeta}\vartheta \,\mathrm{d}\,\boldsymbol{x} \\
&\quad + \int_{\Gamma_N} g(\vartheta)\vartheta + \frac{1}{2}\boldsymbol{v} \cdot \boldsymbol{n}|\vartheta|^2 \,\mathrm{d}\,S \\
&\geq \frac{\kappa}{2}\|\nabla\vartheta\|^2_{L^2} - C\|\boldsymbol{\zeta}\|^2_{L^2}\,.
\end{aligned}$$

The first inequality may be observed by applying an integration-by-parts formula as in (4.19) and the fundamental theorem of differentiation and integration on $\tilde{\boldsymbol{f}}$ similar to (4.20) as

$$\tilde{\boldsymbol{f}}(\boldsymbol{\zeta}_{eq}(\vartheta) - \boldsymbol{\zeta}) - \tilde{\boldsymbol{f}}(\zeta_{eq}(\vartheta) = -\zeta \int_0^1 \nabla\tilde{\boldsymbol{f}}(\boldsymbol{\zeta}_{\mathrm{eq}} - s\boldsymbol{\zeta}(\vartheta)) \,\mathrm{d}\, s. \tag{4.22}$$

The second inequality follows from the monotony of g as well as the condition $\boldsymbol{v} \cdot \boldsymbol{n} \geq 0$ on Γ_N and the boundedness of $\nabla\tilde{\boldsymbol{f}}$ and that $\delta\|\vartheta\|^2_{L^2}$ can be absorbed into the leading order term for δ small enough.

The uniqueness of solutions to (4.17) follows from similar (but simpler) arguments as the uniqueness of the full system (see Proposition 5).

The mapping $\mathcal{T}$ is well defined, i.e., maps into L^2_R, for R big enough follows from the previous estimate, the bound we found on $\boldsymbol{\zeta}$, and the boundedness of q in L^2.

The continuity of $\mathcal{T}$ follows from the continuity of the solution operators $\mathcal{A}_{\overline{\vartheta}}$ and $\mathcal{H}_{\boldsymbol{\zeta}}$. Since $H^1_{\Gamma_D}$ is compactly embedded into L^2, Schauder's fixed point theorem assures the existence of a solution to the coupled system in the sense of Definition 2.

Regularity: In order to prove that the solution has the asserted regularity, we cite different results from the literature. Concerning the Hölder regularity, we observe that the energy balance can be written as

$$-\nabla\cdot(\kappa(\vartheta(\boldsymbol{x}))\nabla\vartheta) = F \quad \text{in } W^{-1,p}_{\Gamma_D} \quad \text{for } p > 3$$

where the right-hand side F is given by

$$\langle F, \varphi \rangle = -\int_\Omega (\boldsymbol{v} \cdot \nabla)\vartheta\varphi + \rho\boldsymbol{L} \cdot \boldsymbol{f}(\vartheta, \boldsymbol{\zeta})\varphi \,\mathrm{d}\,\boldsymbol{x} - \int_{\Gamma_N} g(\vartheta)\varphi \,\mathrm{d}\,S + \int_\Omega q\varphi \,\mathrm{d}\,\boldsymbol{x}\,.$$

This functional may be estimated by

$$|\langle F, \varphi \rangle| \leq c \left(|\boldsymbol{v}| \|\nabla \vartheta\|_{L^2} + |\rho \boldsymbol{L}| \|\boldsymbol{f}(\vartheta, \boldsymbol{\zeta})\|_{L^2} + \|g(\vartheta)\|_{W^{-1/p,p}(\Gamma_N)} + \|q\|_{W^{-1,p}} \right) \|\varphi\|_{W^{1,p'}}, \quad (4.23)$$

where $p' = p/(p-1)$. We used the embeddings $W^{1,p'}_{\Gamma_D}(\Omega) \hookrightarrow L^2(\Omega)$ and $W^{1,p'}(\Omega) \hookrightarrow W^{1-1/p',p'}(\Gamma_N) = W^{1/p,p'}(\Gamma_N)$ for $p \in (3,6)$, i.e., $p' \in (6/5, 3/2)$. The result in [51] provides the Hölder continuity of the solution $\vartheta \in \mathcal{C}^{0,\alpha}(\Omega)$ for some $\alpha > 0$.

Uniqueness: The uniqueness follows from Proposition 5 with $\boldsymbol{a} = 0$. Indeed, the comparison criterion implies that ϑ is unique and also $\rho \boldsymbol{L} \cdot \boldsymbol{\zeta}$. Since $\boldsymbol{\zeta} = \boldsymbol{0}$ is always a sub solution to equation (4.8), $\boldsymbol{\zeta}_i$ is positive such that the condition $\rho \boldsymbol{L}_i \geq 0$ for all $i \in \{0, \dots, m\}$, which implies that $\boldsymbol{\zeta}$ is unique. □

Corollary 6. *The solution operator $\mathcal{S} : W^{-1,p}_{\Gamma_D}(\Omega) \to W^{1,p}_{\Gamma_D}(\Omega) \times H^1_{\Gamma_D}(\Omega)^m$ mapping q to a solution according to Definition 2 is even continuous, i.e., $q_n \to q$ in $W^{-1,p}_{\Gamma_D}(\Omega)$ implies $\mathcal{S}(q_n) \to \mathcal{S}(q)$ in $W^{1,p}_{\Gamma_D}(\Omega) \times H^1_{\Gamma_D}(\Omega)^m$.*

4.4 Linearised state equations

In order to prove the Fréchet differentiability of the solution operator $\mathcal{S}$ from Theorem 6, we want to employ the implicit function theorem. For this, first it is convenient to prove the existence and uniqueness of a solution of the linearised state equations.

Assumption 7. *There exists a $M > 0$ such that $|\kappa'(y)| \leq M$ for all $y \in \mathbb{R}$.*

Theorem 8. *Let $(\vartheta^*, \boldsymbol{\zeta}^*)$ be given and $p \in (3,6)$. For every $q \in W^{-1,p}_{\Gamma_D}(\Omega)$ there exists a unique solution $(\vartheta, \boldsymbol{\zeta}) \in W^{1,p}(\Omega) \times H^1_{\Gamma_D}(\Omega)^m$ to the linearised state equations*

$$\begin{aligned}
(\boldsymbol{v} \cdot \nabla)\vartheta - \nabla \cdot (\kappa(\vartheta^*)\nabla\vartheta + \kappa'(\vartheta^*)\vartheta\nabla\vartheta^*) & \\
+ \rho \boldsymbol{L} \cdot (\boldsymbol{f}_\vartheta(\vartheta^*, \boldsymbol{\zeta}^*)\vartheta + \boldsymbol{f}_{\boldsymbol{\zeta}}(\vartheta^*, \boldsymbol{\zeta}^*) \cdot \boldsymbol{\zeta}) &= q && \text{in } \Omega, && (4.24a)\\
\boldsymbol{n} \cdot \kappa(\vartheta^*)\nabla\vartheta + \kappa'(\vartheta^*)\vartheta\nabla\vartheta^* &= g'(\vartheta^*)\vartheta && \text{on } \Gamma_N, && (4.24b)\\
\vartheta &= 0 && \text{on } \Gamma_D, && (4.24c)\\
(\boldsymbol{v} \cdot \nabla)\boldsymbol{\zeta} - \varepsilon\Delta\boldsymbol{\zeta} - (\boldsymbol{f}_{\boldsymbol{\zeta}}(\vartheta^*, \boldsymbol{\zeta}^*) \cdot \boldsymbol{\zeta} + \boldsymbol{f}_\vartheta(\vartheta^*, \boldsymbol{\zeta}^*)\vartheta) &= \boldsymbol{0} && \text{in } \Omega, && (4.24d)\\
\boldsymbol{n} \cdot \nabla\boldsymbol{\zeta} &= \boldsymbol{0} && \text{on } \Gamma_N, && (4.24e)\\
\boldsymbol{\zeta} &= \boldsymbol{0} && \text{on } \Gamma_D. && (4.24f)
\end{aligned}$$

Proof. The *existence* follows from the linearity of the equation, the uniqueness and Fredholm's theorem.

We are going to split the equation into parts, the main part and the compact perturbations. Therefore, we introduce the operator $\mathcal{A}(\vartheta^*, \boldsymbol{\zeta}^*) : (H^1_{\Gamma_D})^{m+1} \to (H^{-1}_{\Gamma_D})^{m+1}$ via

$$\langle \mathcal{A}(\vartheta^*, \boldsymbol{\zeta}^*)(\vartheta, \boldsymbol{\zeta}), (\varphi, \boldsymbol{\psi}) \rangle = \int_\Omega \kappa(\vartheta^*)\nabla\vartheta \cdot \nabla\varphi + \varepsilon\nabla\boldsymbol{\zeta} : \nabla\boldsymbol{\psi} \,\mathrm{d}\boldsymbol{x} + \int_{\Gamma_N} g'(\vartheta^*)\vartheta\varphi \,\mathrm{d}\boldsymbol{x}$$

and the operator $\mathcal{B}(\vartheta^*, \boldsymbol{\zeta}^*) : (L^{2p/(p-2)}(\Omega))^{m+1} \to (H^{-1}_{\Gamma_D})^{m+1}$ via

$$\langle \mathcal{B}(\vartheta^*, \boldsymbol{\zeta}^*)(\vartheta, \boldsymbol{\zeta}), (\varphi, \boldsymbol{\psi}) \rangle = \int_\Omega \kappa'(\vartheta^*)\vartheta \nabla \vartheta^* \cdot \nabla \varphi - (\boldsymbol{v} \cdot \nabla)\varphi\vartheta - (\boldsymbol{v} \cdot \nabla)\boldsymbol{\psi} \cdot \boldsymbol{\zeta} \,\mathrm{d}\boldsymbol{x}$$

as well as the boundary part operator $\mathcal{C}(\vartheta^*, \boldsymbol{\zeta}^*) : (L^2(\Gamma_N))^{m+1} \to (H^{-1}_{\Gamma_D})^{m+1}$

$$\langle \mathcal{C}(\vartheta^*, \boldsymbol{\zeta}^*)(\vartheta, \boldsymbol{\zeta}), (\varphi, \boldsymbol{\psi}) \rangle = \int_{\Gamma_N} (\boldsymbol{v} \cdot \boldsymbol{n})(\varphi\vartheta + \boldsymbol{\zeta} \cdot \boldsymbol{\psi}) \,\mathrm{d}S$$

as well as the compact embedding operator $j : H^1_{\Gamma_D}(\Omega) \to L^{2p/(p-2)}(\Omega)$ as well as $j_{\mathrm{tr}} : H^1_{\Gamma_D}(\Omega) \to L^2(\Gamma_N)$. These operators are well defined , i.e., for $\mathcal{B}$ we observe

$$\begin{aligned}
&\int_\Omega \kappa'(\vartheta^*)\vartheta \nabla \vartheta^* \cdot \nabla \varphi - (\boldsymbol{v} \cdot \nabla)\varphi\vartheta - (\boldsymbol{v} \cdot \nabla)\boldsymbol{\psi} \cdot \boldsymbol{z} \,\mathrm{d}\boldsymbol{x} \\
&\leq c \left(\|\vartheta\|_{L^{2p/(p-2)}} \|\nabla \vartheta^*\|_{L^p} \|\nabla \varphi\|_{L^2} + \|\nabla \varphi\|_{L^2} \|\vartheta\|_{L^2} + \|\nabla \boldsymbol{\psi}\|_{L^2} \|\boldsymbol{z}\|_{L^2} \right) .
\end{aligned}$$

For every $q \in H^{-1}_{\Gamma_D}(\Omega)$ the system (4.24) can now be expressed as the operator equation

$$\mathcal{A}(\vartheta^*, \boldsymbol{\zeta}^*) + \mathcal{B}(\vartheta^*, \boldsymbol{\zeta}^*) \circ j + \mathcal{C}(\vartheta^*, \boldsymbol{\zeta}^*) \circ j_{\mathrm{tr}} = q \qquad \text{in } H^{-1}_{\Gamma_D}(\Omega) .$$

Applying the inverse of $\mathcal{A}(\vartheta^*, \boldsymbol{\zeta}^*)$ we arrive at

$$I + \mathcal{A}(\vartheta^*, \boldsymbol{\zeta}^*)^{-1} \left(\mathcal{B}(\vartheta^*, \boldsymbol{\zeta}^*) \circ j + \mathcal{C}(\vartheta^*, \boldsymbol{\zeta}^*) \circ j_{\mathrm{tr}} \right) = \mathcal{A}(\vartheta^*, \boldsymbol{\zeta}^*)^{-1} q \qquad \text{in } H^1_{\Gamma_D}(\Omega) .$$

Due to the compactness of j and j_{tr} we can apply Fredholm's theorem stating: for every $q \in H^{-1}_{\Gamma_D}(\Omega)$, we will find a unique solution to the above equation if the homogeneous equation admits only the trivial solution. Since $\mathcal{A}(\vartheta^*, \boldsymbol{\zeta}^*)$ is an isomorphism, we need to prove the uniqueness of solutions to the linearised equation (4.24).

Uniqueness: The uniqueness follows by Proposition 5, with $\kappa(\vartheta) = \kappa(\vartheta^*)$, $\boldsymbol{a} = \kappa'(\vartheta^*)\nabla\vartheta^*$, and $\tilde{\boldsymbol{f}}(\cdot) = (\nabla \tilde{\boldsymbol{f}}(\boldsymbol{\zeta}_{\mathrm{eq}}(\vartheta^*) - \boldsymbol{\zeta}^*))^{-1} \cdot$, as well as $\boldsymbol{\zeta}_{\mathrm{eq}}(\vartheta) = \boldsymbol{\zeta}'_{\mathrm{eq}}(\vartheta^*)\vartheta$.

Regularity: First we remark that ϑ admits the additional regularity. By observing that the linearised equation can be written as

$$-\nabla \cdot (\kappa(\vartheta^*)\nabla\vartheta) = F := \nabla \cdot (\kappa'(\vartheta^*)\vartheta\nabla\vartheta^*) - (\boldsymbol{v} \cdot \nabla)\vartheta - \rho \boldsymbol{L} \cdot (\boldsymbol{f}_\vartheta(\vartheta^*, \boldsymbol{\zeta}^*)\vartheta + \boldsymbol{f}_{\boldsymbol{\zeta}}(\vartheta^*, \boldsymbol{\zeta}^*) \cdot \boldsymbol{\zeta}) + q .$$

For the right-hand side F we find that F is bounded in $W^{-1,r}_{\Gamma_D}(\Omega)$ for some $r > 2$. Indeed, by estimating F, we find

$$\begin{aligned}
\langle F, \varphi \rangle = &\int_\Omega \kappa'(\vartheta^*)\vartheta \nabla \vartheta^* \cdot \nabla \varphi - (\boldsymbol{v} \cdot \nabla)\vartheta\varphi - \rho \boldsymbol{L} \cdot (\boldsymbol{f}_\vartheta(\vartheta^*, \boldsymbol{\zeta}^*)\vartheta\varphi + \boldsymbol{f}_{\boldsymbol{\zeta}}(\vartheta^*, \boldsymbol{\zeta}^*) \cdot \boldsymbol{\zeta}\varphi) + q\varphi \\
&\leq \|\vartheta\|_{L^6} \|\nabla \vartheta^*\|_{L^p} \|\nabla \varphi\|_{L^{6p/(5p-6)}} + |\boldsymbol{v}| \|\nabla \varphi\|_{L^2} \|\vartheta\|_{L^2} \\
&\quad + |\rho \boldsymbol{L}| \|\boldsymbol{f}_\vartheta(\vartheta^*, \boldsymbol{\zeta}^*)\|_{L^2} \|\vartheta\|_{L^6} \|\varphi\|_{L^6} + \|\boldsymbol{f}_{\boldsymbol{\zeta}}(\vartheta^*, \boldsymbol{\zeta}^*)\|_{L^2} \|\boldsymbol{\zeta}\|_{L^2} \|\varphi\|_{L^6} .
\end{aligned}$$

By the standard embeddings, we find that $F \in W^{-1,6p/(p+6)}$, which is bigger than 2 since $p > 3$. By a bootstrap argument, we get additional regularity. Finally, for $\vartheta \in L^\infty$, we find that $F \in W^{-1,p}_{\Gamma_D}(\Omega)$ which implies by the result [51] that $\vartheta \in W^{1,p}_{\Gamma_D}(\Omega)$. □

Assumption 9. *Let f and κ be $\mathcal{C}^2$ functions, such that $\boldsymbol{f} \in \mathcal{C}^2(\mathbb{R}, \mathbb{R}^m; \mathbb{R}^m)$ and $\kappa \in \mathcal{C}^2(\mathbb{R})$.*

Theorem 10. *Let the assumptions of Theorem 8 and Assumption 9 be fulfilled. Then the control-to-state mapping $\mathcal{S} : W^{-1,p}_{\Gamma_D}(\Omega) \to W^{1,p}_{\Gamma_D}(\Omega) \times H^1_{\Gamma_D}(\Omega)^m$, $\mathcal{S}(u) = y_u = (\vartheta_u, \boldsymbol{\zeta}_u)$, is of class C^2. Moreover, for any function w, $\tilde{w}$, and $\bar{w} \in W^{-1,p}(\Omega)$ the functions $y_w = (\vartheta_w, \boldsymbol{\zeta}_w) = \mathcal{S}'(u)w$ and $y_{\tilde{w},\bar{w}} = (\vartheta_{\tilde{w},\bar{w}}, \boldsymbol{\zeta}_{\tilde{w},\bar{w}}) = \mathcal{S}''(u) : [\tilde{w} \otimes \bar{w}]$ are the unique solutions in $W^{-1,p}(\Omega)$ of the equations*

$$\left\{\begin{aligned} (\boldsymbol{v}\cdot\nabla)\vartheta - \Delta\left(\kappa(\vartheta_u)\vartheta\right) + \rho\boldsymbol{L}\cdot\left(\boldsymbol{f}_\vartheta(\vartheta_u,\boldsymbol{\zeta}_u)\vartheta + \boldsymbol{f}_{\boldsymbol{\zeta}}(\vartheta_u,\boldsymbol{\zeta}_u)\cdot\boldsymbol{\zeta}\right) &= w && \text{in } \Omega,\\ \boldsymbol{n}\cdot\nabla(\kappa(\vartheta_u)\vartheta) &= g'(\vartheta_u)\vartheta && \text{in } \Gamma_N,\\ \vartheta &= 0 && \text{on } \Gamma_D,\\ (\boldsymbol{v}\cdot\nabla)\boldsymbol{\zeta} - \left(\boldsymbol{f}_{\boldsymbol{\zeta}}(\vartheta_u,\boldsymbol{\zeta}_u)\cdot\boldsymbol{\zeta} + \boldsymbol{f}_\vartheta(\vartheta_u,\boldsymbol{\zeta}_u)\vartheta\right) &= \mathbf{0} && \text{in } \Omega,\\ \boldsymbol{\zeta} &= \mathbf{0} && \text{on } \Gamma_D\,, \end{aligned}\right. \tag{4.25}$$

and

$$\left\{\begin{aligned} (\boldsymbol{v}\cdot\nabla)\vartheta - \Delta\left(\kappa(\vartheta_u)\vartheta\right) + \rho\boldsymbol{L}\cdot\left(\boldsymbol{f}_\vartheta(\vartheta_u,\boldsymbol{\zeta}_u)\vartheta + \boldsymbol{f}_{\boldsymbol{\zeta}}(\vartheta_u,\boldsymbol{\zeta}_u)\cdot\boldsymbol{\zeta}\right)&\\ -\Delta(\kappa'(\vartheta_u)\vartheta_{\tilde{w}}\vartheta_{\bar{w}}) + \rho\boldsymbol{L}\cdot(y_{\tilde{w}}\cdot\nabla_y^2\boldsymbol{f}(y_u)y_{\bar{w}}) &= 0 && \text{in } \Omega,\\ \boldsymbol{n}\cdot\nabla(\kappa(\vartheta_u)\vartheta + \kappa'(\vartheta_u)\vartheta_{\tilde{w}}\vartheta_{\bar{w}}) - g''(\vartheta_u)\vartheta_{\tilde{w}}\vartheta_{\bar{w}} &= g'(\vartheta_u)\vartheta && \text{in } \Gamma_N,\\ \vartheta &= 0 && \text{on } \Gamma_D,\\ (\boldsymbol{v}\cdot\nabla)\boldsymbol{\zeta} - \left(\boldsymbol{f}_{\boldsymbol{\zeta}}(\vartheta_u,\boldsymbol{\zeta}_u)\cdot\boldsymbol{\zeta} + \boldsymbol{f}_\vartheta(\vartheta_u,\boldsymbol{\zeta}_u)\vartheta\right) - y_{\tilde{w}}\cdot\nabla_y^2\boldsymbol{f}(y_u)y_{\bar{w}} &= \mathbf{0} && \text{in } \Omega,\\ \boldsymbol{\zeta} &= \mathbf{0} && \text{on } \Gamma_D\,, \end{aligned}\right. \tag{4.26}$$

respectively. Note that the unknown of the systems is always denoted by $(\vartheta, \boldsymbol{\zeta})$.

Proof. Let us introduce the operator $\mathcal{F} : W^{1,p}_{\Gamma_D}(\Omega) \times H^1_{\Gamma_D}(\Omega)^m \times W^{-1,p}_{\Gamma_D}(\Omega) \to W^{-1,p}_{\Gamma_D}(\Omega) \times H^{-1}_{\Gamma_D}(\Omega)^m$ via

$$\langle \mathcal{F}(\vartheta,\boldsymbol{\zeta},u),(\varphi,\boldsymbol{\psi})\rangle := \begin{pmatrix} \int_\Omega (\boldsymbol{v}\cdot\nabla\vartheta)\varphi + \kappa(\vartheta)\nabla\vartheta\cdot\nabla\varphi + \rho\boldsymbol{L}\cdot\boldsymbol{f}(\vartheta,\boldsymbol{\zeta})\varphi\,\mathrm{d}\,\boldsymbol{x} + \int_{\Gamma_N} g(\vartheta)\varphi\,\mathrm{d}\,S - \langle (Q+u),\varphi\rangle\,\mathrm{d}\,\boldsymbol{x} \\ \int_\Omega (\boldsymbol{v}\cdot\nabla\boldsymbol{\zeta})\cdot\boldsymbol{\psi} + \varepsilon\nabla\boldsymbol{\zeta} : \nabla\boldsymbol{\psi} - \boldsymbol{f}(\vartheta,\boldsymbol{\zeta})\boldsymbol{\psi}\,\mathrm{d}\,\boldsymbol{x} \end{pmatrix}$$

for every $\varphi \in W^{1,p}_{\Gamma_D}(\Omega)$ and $\boldsymbol{\psi} \in H^1_{\Gamma_D}(\Omega)^m$. Due to assumption 9, this operator is well defined and of class C^1. Moreover, the identity $\mathcal{F}(\vartheta_u, \boldsymbol{\zeta}_u, u) = 0$ holds for all $u \in W^{-1,p}$. We want to apply the implicit function theorem to deduce differentiability of the solution operator and obtain the directional derivative as the solution to the system (4.25). Therefore, we observe that the derivative $(\partial/\partial y)\mathcal{F}(y_u, u)$ is given by the solution $(\vartheta, \boldsymbol{\zeta})$ of the linearised system (4.24) with $(\vartheta^*, \boldsymbol{\zeta}^*) = (\vartheta_u, \boldsymbol{\zeta}_u)$ and vanishing right-hand side $q = 0$. According to Theorem 8, for any $q \in W^{-1,p}_{\Gamma_D}(\Omega)$ there exists a unique solution $y_w = (\vartheta_w, \boldsymbol{\zeta}_w) \in W^{1,p}_{\Gamma_D}(\Omega) \times (H^1_{\Gamma_D}(\Omega))^m$ to the linearised equation (4.24). Hence, $(\partial/\partial y)\mathcal{F}(y_u, u)$ is an isomorphism and the implicit function theorem grants the assertions of the theorem after some standard calculations. □

4.5 Optimal control problem

In the following, we focus on the optimal control of the state equations (4.6). Consider the cost functional

$$J(\vartheta, u) = \frac{\alpha_1}{2} \int_{\Omega_1} (\vartheta - \vartheta_d)^2 \,\mathrm{d}\,\boldsymbol{x} + \frac{\alpha_2}{2} \int_{\Omega} u^2 \,\mathrm{d}\,\boldsymbol{x}\,, \tag{4.27}$$

where $\vartheta_d \in L^2$, $\Omega_1 \subseteq \Omega$ and $\alpha_i > 0$ for $i = 1, 2$.

Associated to the state equations (4.6), we introduce the optimal control problem

$$\begin{aligned} &\min_u J(\vartheta_u, u) \\ &\text{subject to weak formulation of system (4.6)} \\ &u \in U_{ad}. \end{aligned} \tag{4.28}$$

The function ϑ_u is the first component of the solution to the state equation (4.6). The set U_{ad} is the set of all admissible controls. First, we study the existence of a solution to the optimal control problem consisting of the functional (4.27) and the state equations (4.6).

Theorem 11. *Let the assumption 1 be fulfilled. Then there exists at least one optimal control to the functional* (4.27)*, where* $(\vartheta_u, \boldsymbol{\zeta}_u)$ *is the weak solution to* (4.6) *according to Definition 2.*

Proof. We prove the assertion via the standard direct approach in the calculus of variations. Let $\{u_n\}_{n\in\mathbb{N}} \subset L^2(\Omega)$ be a minimizing sequence to the functional, with associated solution $y_{u_n} = (\vartheta_{u_n}, \boldsymbol{\zeta}_{u_n})$ to the system of state equations (4.6). Since (4.27) is bounded, we can extract a not-relabelled subsequence such that $u_n \rightharpoonup u$ weakly in L^2 such that $u_n \to u$ strongly in $W^{-1,p}$. From the continuity of the solution operator $\mathcal{S}$ to the system of state equations (4.6), we may infer that $y_{u_n} \to y$ in $W^{1,p}_{\Gamma_D}(\Omega) \times H^1_{\Gamma_D}(\Omega)^m$. The continuity of the functional u with respect to the convergence of $\vartheta_{u_n} \to \vartheta_u$ in $W^{1,p}_{\Gamma_D}(\Omega)$ and the weak-lower semi-continuity of the functional J (see (4.27)) with respect to weak convergence $u_n \rightharpoonup u$ in L^2 implies

$$J(\vartheta_u, u) \leq \liminf_{n\to\infty} J(\vartheta_{u_n}, u_n) \leq \lim_{n\to\infty} J(\vartheta_{u_n}, u_n) = \inf\,.$$

The infimum is attained since $\{u_n\}$ was assumed to be a minimizing sequence. □

Theorem 12. *Let the Assumptions 7 and 9 be fulfilled. Then the function* $\tilde{J}$*,* $\tilde{J}(u) = J(\vartheta_u, u)$*, is twice continuously differentiable, such that for every* u*,* w*,* $\tilde{w}$*, and* $\bar{w} \in L^2(\Omega)$*, it holds*

$$\tilde{J}'(u)w = \int_\Omega \alpha_2 u w \,d\,\boldsymbol{x} + \int_\Omega \gamma p_u w \,d\,\boldsymbol{x} \tag{4.29}$$

and

$$\begin{aligned} \tilde{J}''(u)[\tilde{w} \otimes \bar{w}] = &\int_{\Omega_1} \alpha_1 \tilde{\vartheta}\bar{\vartheta} \,d\,\boldsymbol{x} + \int_\Omega \alpha_2 \tilde{w}\bar{w} \,d\,\boldsymbol{x} - \int_\Omega \gamma \nabla p_u \cdot \nabla(\kappa'(\vartheta_u)\vartheta_{\tilde{w}}\vartheta_{\bar{w}}) \,d\,\boldsymbol{x} \\ &- \int_\Omega \left(\rho \boldsymbol{L} \cdot (y_{\tilde{w}} \nabla_y^2 \boldsymbol{f}(y_u) y_{\bar{w}}) p_u - (y_{\tilde{w}} \nabla_y^2 \boldsymbol{f}(y_u) y_{\bar{w}}) \cdot \boldsymbol{q}_u\right) d\,\boldsymbol{x} \qquad (4.30) \\ &- \int_{\Gamma_N} g''(\vartheta_u)\vartheta_{\tilde{w}}\vartheta_{\bar{w}} p_u \,d\,S\,, \qquad (4.31) \end{aligned}$$

where $(p_u, \boldsymbol{q}_u)$ *is the unique solution to the adjoint equation*

$$\begin{cases} -(\boldsymbol{v}\cdot\nabla)p - \kappa(\vartheta_u)\Delta p + \rho\boldsymbol{L}\cdot\boldsymbol{f}_\vartheta(\vartheta_u,\boldsymbol{\zeta}_u)p + \boldsymbol{f}_\vartheta(\vartheta_u,\boldsymbol{\zeta}_u)\cdot\boldsymbol{q} &= \alpha_1(\vartheta_u-\vartheta_d)\chi_{\Omega_1} & \text{in } \Omega, \\ \kappa(\vartheta_u)\boldsymbol{n}\cdot\nabla p + (\boldsymbol{v}\cdot\boldsymbol{n})p &= g'(\vartheta_u)p & \text{on } \Gamma_N, \\ p &= 0 & \text{on } \Gamma_D, \\ -(\boldsymbol{v}\cdot\nabla)\boldsymbol{q} - \varepsilon\Delta\boldsymbol{q} - \boldsymbol{f}_{\boldsymbol{\zeta}}(\vartheta_u,\boldsymbol{\zeta}_u)\cdot\boldsymbol{q} + \rho\boldsymbol{L}\cdot\boldsymbol{f}_{\boldsymbol{\zeta}}(\vartheta_u,\boldsymbol{\zeta}_u)p &= \boldsymbol{0} & \text{in } \Omega, \\ \varepsilon\boldsymbol{n}\cdot\nabla\boldsymbol{q} + (\boldsymbol{v}\cdot\boldsymbol{n})\boldsymbol{q} &= \boldsymbol{0} & \text{on } \Gamma_N, \\ \boldsymbol{q} &= \boldsymbol{0} & \text{on } \Gamma_D, \end{cases} \tag{4.32}$$

and $y_{\tilde{w}} = (\vartheta_{\tilde{w}}, \boldsymbol{\zeta}_{\tilde{w}}) = \mathcal{S}'(u)\tilde{w}$, $y_{\bar{w}} = (\vartheta_{\bar{w}}, \boldsymbol{\zeta}_{\bar{w}}) = \mathcal{S}'(u)\bar{w}$ *and* ∇_y *has to be understood as the component wise derivative* $(\partial_\vartheta, \partial_{\boldsymbol{\zeta}})^T$.

Proof. The only point one has to observe is that the differential operator associated to the problem (4.32) is actually the adjoint operator in $\mathcal{L}(W^{1,p}_{\Gamma_D}(\Omega)\times H^1_{\Gamma_D}(\Omega)^m, W^{-1,p}_{\Gamma_D}(\Omega)\times H^{-1}_{\Gamma_D}(\Omega)^m)$ to the operator associated to the problem (4.24). Therewith, existence and uniqueness for the adjoint problem follows immediately. □

4.6 Numerical approach

In this section we are going to establish the setting where the optimal control of preheating for flame cutting from Section 4.5 is solved. To simplify the exposition, we consider $\boldsymbol{\zeta}$, the vector containing the steel phases to be unidimensional, ζ, as it will only contain the liquid steel phase concentration. Equivalently, the vector $\boldsymbol{L}$ will contain only latent heat for the melting transformation L. Because of the availability of material data and numerical reasons, in this section we use the system (4.5) instead of the system (4.6) used for analysis in Section 4.3. This way, the state equations (4.5) can be written in the weak formulation as

$$\begin{aligned} \int_\Omega \tilde{\eta}(\theta)(\boldsymbol{v}\cdot\nabla\theta)\varphi\,\mathrm{d}\boldsymbol{x} + \int_\Omega \tilde{\kappa}(\theta)\nabla\theta\cdot\nabla\varphi\,\mathrm{d}\boldsymbol{x} = &\int_\Omega \left(Q_F(v) + u\cdot\gamma - \rho L\tilde{f}(\theta,\zeta)\right)\varphi\,\mathrm{d}\boldsymbol{x} \\ &+ \int_{\Gamma_N} g_1(\boldsymbol{x},\theta)\varphi ds \end{aligned} \tag{4.33}$$

$$\int_\Omega (\boldsymbol{v}\cdot\nabla\zeta)\psi\,\mathrm{d}\boldsymbol{x} + \int_\Omega \varepsilon\nabla\zeta\cdot\nabla\psi\,\mathrm{d}\boldsymbol{x} = \int_\Omega \tilde{f}(\theta,\zeta)\psi\,\mathrm{d}\boldsymbol{x} \tag{4.34}$$

with the different Neumann boundary conditions for the temperature θ stored in $g_1(\boldsymbol{x},\theta)$ as

$$g_1(\boldsymbol{x},\theta) = \begin{cases} h(\theta_a-\theta), & \text{for } \boldsymbol{x}\in\{z=0\}\cup\{z=-z_{max}\} \\ 0, & \text{for } \boldsymbol{x}\in\{y=0\}\cup\{x=x_{max}\} \end{cases} \tag{4.35}$$

and the test functions $\varphi \in W^{1,p'}_{\Gamma_D}(\Omega)$ with $1/p + 1/p' = 1$ and $\psi \in H^1_{\Gamma_D}(\Omega)$.

Using the cost functional $J(\theta, u)$ from (4.27), the resultant adjoint system with variables p and q equivalent to (4.32) is

$$
\begin{aligned}
&-\int_{\Omega} \tilde{\eta}\left(\theta\right)\left(\boldsymbol{v}\cdot\nabla p\right)\phi\,\mathrm{d}\,\boldsymbol{x}+\int_{\Omega}\rho L\tilde{f}_{\theta}'\left(\theta,\zeta\right)p\phi\,\mathrm{d}\,\boldsymbol{x}-\int_{\Omega}\tilde{f}_{\theta}'\left(\theta,\zeta\right)q\phi\,\mathrm{d}\,\boldsymbol{x}-\int_{\Omega}\tilde{\kappa}\left(\theta\right)\Delta p\phi\,\mathrm{d}\,\boldsymbol{x}\\
&=\alpha_1\int_{\Omega_1}\left(\theta-\theta_d\right)\phi\,\mathrm{d}\,\boldsymbol{x} \qquad (4.36)\\
&\int_{\Omega}\left(\boldsymbol{v}\cdot\nabla q\right)\lambda dx-\int_{\Omega}\varepsilon\nabla q\cdot\nabla\lambda dx-\int_{\Gamma_N}q(\boldsymbol{v}\cdot\boldsymbol{n})\lambda ds+\int_{\Omega}\tilde{f}_{\zeta}'\left(\theta,\zeta\right)q\lambda dx-\int_{\Omega}\rho L\tilde{f}_{\zeta}'\left(\theta,\zeta\right)p\lambda dx\\
&=0 \qquad (4.37)
\end{aligned}
$$

with test functions $\phi \in W^{1,p'}_{\Gamma_D}(\Omega)$ with $1/p + 1/p' = 1$ and $\lambda \in H^1_{\Gamma_D}(\Omega)$.

Notice that the term in (4.36) with $\tilde{\kappa}\left(\theta\right)\Delta p$ was not expanded integrating by parts due to the nonlinearities involved. Instead, we define an auxiliary variable ω equal to Δp such that

$$
\int_{\Omega}\omega\xi\,\mathrm{d}\,\boldsymbol{x}=-\int_{\Omega}\nabla p\cdot\nabla\xi\,\mathrm{d}\,\boldsymbol{x}-\int_{\Gamma_N}g_2(\boldsymbol{x},\theta,\tilde{\eta},\tilde{\kappa})p\xi ds,\quad\forall\xi\in H^1_{\Gamma_D}(\Omega) \qquad (4.38)
$$

The function $g_2(\boldsymbol{x},\theta,\tilde{\eta},\tilde{\kappa})$ contains the Neumann boundary conditions of the adjoint variable p with

$$
g_2(\boldsymbol{x},\theta,\tilde{\eta},\tilde{\kappa})=\begin{cases}-\dfrac{h}{\tilde{\kappa}(\theta)}, & \text{for } \boldsymbol{x}\in\{z=0\}\cup\{z=-z_{max}\}\\ -\dfrac{\tilde{\eta}(\theta)}{\tilde{\kappa}(\theta)}\boldsymbol{v}\cdot\boldsymbol{n}, & \text{for } \boldsymbol{x}\in\{x=x_{max}\}\\ 0, & \text{for } \boldsymbol{x}\in\{y=0\}.\end{cases} \qquad (4.39)
$$

As it was mentioned in Section 4.2, γ is a projection factor in the QSS heat equation (4.33) such that the resultant preheating power reflects the behaviour of a realistic induction heating device. We recall the definition of γ in (3.36):

$$
\gamma(\boldsymbol{x})=\chi(x)e^{-c_2y}e^{c_3z}. \qquad (4.40)
$$

The function $\chi(x)$ is the characteristic function of the interval along the x axis where the coil is located, that is, this function has value 1 along the length of the coil and 0 otherwise. This is in correspondence with the fact that the induced currents are located just below the coil and that it cannot be located too close to the flame. The exponential decay in the y-direction reflects that the maximum power is induced in the cutting line below the coil and decreases with the width of the coil, this is known as transversal edge effect. The constant c_2 is related to half the width of the coil as we are considering the symmetry along the cutting plane. Finally, the decline in current density in the z-direction is known as the skin effect and c_3 is related to the depth of the skin effect which is the depth at which the current density falls to $1/e$ ($\sim$37 %) of its value near the surface [35, 34]. A more descriptive definition of γ is given in Section 3.6. See Figure 4.2 for clarification where the different coloured subdomains highlight the location of the flame Λ with respect to where the preheating $u\cdot\gamma$ is concentrated.

The numerical algorithm for the solution of the optimal control requires solving the state system (4.33)-(4.34) and the adjoint system (4.36)-(4.38) and update the control based on (4.29). Then iterate until a convergence condition is fulfilled.

For this, we apply the Finite Element Method (FEM) using the finite element package *pdelib2* [10] developed and maintained at WIAS. The nonlinearities together with the coupling of (4.33)-(4.34) were solved using a fixed-point algorithm and an adaptive mesh module was used to refine the mesh based on a residual-based a posteriori error estimator determining regions with steep gradients for the temperature and melting fraction [5]. Note that the phase transition equation (4.4) cannot be solved directly using FEM without encountering erroneous results and thus we use the Streamline-Upwind Petrov-Galerkin (SUPG) stabilization method to achieve a correct solution [32, 4]. This mesh is reused for the adjoint system (4.36)-(4.38) which can be solved instead in one single step.

To complete the algorithm, we can derive from (4.29) the expression for the approximations of the control variable u using the projected gradient method as

$$u^{k+1} = \mathbb{P}_{[0,\infty)} \left[u^k - m(\alpha_2 u^k + p\gamma) \right] \tag{4.41}$$

with m the gradient step size. The projection $\mathbb{P}_{[0,\infty)}$ is in place to guarantee that the control u is in the admissible set U_{ad}. The definition of U_{ad} is the following:

$$U_{ad} = \{u \in L^2(\Omega) : u(\boldsymbol{x}) \geq 0 \quad \forall \boldsymbol{x} \in \Omega\}. \tag{4.42}$$

This represents that, if u is not null, it can only be positive, i.e., be a heat source and not a sink.

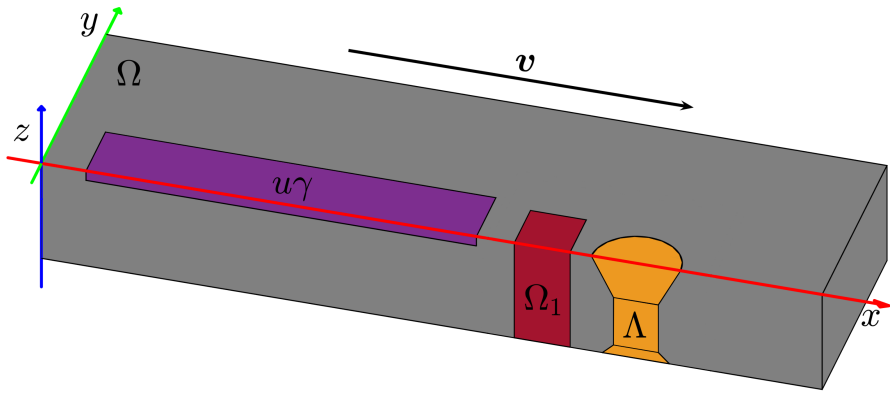

Figure 4.2: Computational domain of optimal control problem. The subdomains in Ω remark (from left to right) where most of the preheating power from $u \cdot \gamma$ is located, Ω_1 where the desired temperature must be achieved and the location of the flame at Λ.

4.7 Results

In this section we present a numerical solution of the optimal control problem from Sections 4.5 and 4.6. We consider a 40 mm Raex® 400 steel plate moving with a cutting speed of 135 mm/min. The aim is to compute the optimal induction preheating source for flame cutting.

According to industrial specifications, the optimal preheating should generate a uniform temperature from top to bottom of the plate just before flame cutting. Furthermore, this desired working temperature is different for different thicknesses and compositions of steel. In the case of Raex® 400 and 40 mm thickness, the working temperature should be between 100

and 125 °C. Notice that the preheating temperature choice is not consistent with the values of Figure 2.6. This is because the values 100 and 125 °C were provided by the industrial partner SSAB from an older report. This way, we define the desired temperature field θ_d in the cost functional (4.27) as 112.5 °C in Ω. To represent that the desired temperature is only needed in a specific area of the plate, we define Ω_1 as a box (rectangular cuboid) around the cutting plane located 20 mm before the flame location and reaching from top to the bottom of the plate (See Figure 4.2). The width of the box is 80 mm in the x-direction and 3 mm in the y-direction.

The steel properties required for the model are the density, specific heat and thermal conductivity. They were derived using the commercial software JMatPro® [31]. This software mainly requires as input the chemical composition of the steel (Table 2.2).

Regarding the phase equation (4.4), the function $\tilde{f}(\theta, \zeta)$ is defined as

$$\tilde{f}(\theta, \zeta) = \frac{1}{\tau_\zeta}[\zeta_{eq}(\theta) - \zeta]_+ \tag{4.43}$$

Here, $\zeta_{eq}(\theta)$ represent the equilibrium volume fraction of liquid at temperature θ. The equilibrium volume fraction of the liquid phase $\zeta_{eq}(\theta)$ should have the maximum value 1, when the temperature exceeds 1537 °C (melting point). Tacitly neglecting a mushy zone, we define $\zeta_{eq}(\theta) = H(\theta - 1537)$, where H is the Heaviside function. In addition, we define the positive part function as $[x]_+ = xH(x)$. The value of τ_ζ representing the transformation velocity is 10^{-2} s. Furthermore, the latent heat value for the melting reaction is 272 kJ/kg. This choice for $\zeta_{eq}(\theta)$ complies with the assumptions in Section 4.3.

As stated, the system (4.5) requires appropriate boundary conditions to be solved. Newton's cooling law is imposed on the top and bottom of the plate to describe the exchange of heat with surrounding air with the convection factor h with value 5 W/(m^2 K). On the symmetry plane $\{y = 0\}$ and on the outflow boundary $\{x = x_{max}\}$, a homogeneous Neumann condition is imposed implicating that there is no heat flux in the normal direction. The temperature of the plate before the process is θ_0 and far enough from the torch, the temperature suffers no change. Therefore, a Dirichlet condition of 25 °C is enforced on the plane $\{y = y_{max}\}$ and on the inflow plane $\{x = 0\}$. On the phase equation side, the Dirichlet condition indicates that there is no volume fraction of liquid in the in-flow plane, far from the heat source. Otherwise, the homogeneous Neumann condition reflects that stationarity has been achieved on the outflow boundary.

With all the aforementioned information, we can focus on the temperature field θ near the flame and the fraction of liquid steel ζ. Figure 4.3 shows θ and ζ near the location of the flame and the immediate area following the movement of the plate. On the left side, the isothermal contours over 1750 °C are useful to recognise the features of Λ, the volume where the heat from the flame is defined. The maximum temperature is reached on the top of the plate in the torch centre, and the temperature is dissipated according to the direction of the movement. On the right, the liquid phase or steel removed can be seen. The phase starts at the isothermal surface corresponding where the equilibrium volume fraction is 1, in this case, the 1537 °C. Moreover, there is a transparent slice such that the inner profile along the thickness can be

observed. The trail is wider on top while on the middle and bottom remains the same. The fields θ and ζ remain almost constant in this region during the algorithm.

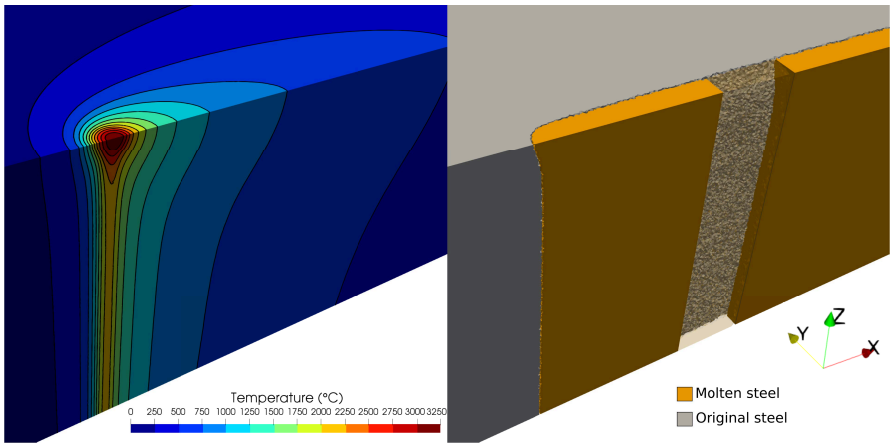

Figure 4.3: Temperature around the flame location and liquid trail generated by it.

Regarding the preheating, the γ function (4.40) used to restrict the control u so it is identifiable to an induction coil is characterized by the parameters c_2 and c_3 with values 100 and 300 respectively. To complete the definition, $\chi(x)$ is nonzero in the x-axis only from 0 to 800 mm. This way it represents a coil of the same length. The distance between the flame and the coil is 200 mm as the centre of the flame is located at 1000 mm (see Figure 4.1 and 4.2).

$$\chi(x) = \begin{cases} 1, & \text{for } 0 \leq x \leq 800 \\ 0, & \text{otherwise} \end{cases} \tag{4.44}$$

Without the term γ, the control could include, for example, direct heating on Ω_1 or from the bottom of the plate which is inconsistent with the location of the coil on top of the plate. The projection $\mathbb{P}_{[0,\infty)}$ is required on u so it is greater or equal than zero, otherwise it could take negative values that can be understood as cooling.

Finally, the weights α_1 and α_2 in the cost functional J (4.27) were chosen so the main focus was on achieving the desired working temperature without limit on the preheating power. This way, we found the values 10^{12} and 1 respectively to produce good results.

We will denote the values for the preheating source, i.e., the control u in each iteration of the algorithm as u^k. Moreover, we will refer to the product $u \cdot \gamma$ as restricted control $\bar{u}$ and equivalently $\bar{u}^k$ in each iteration. In Figure 4.4 we display several iterations of the restricted control on the top of the plate in the x-axis.

As the initial guess for the projected gradient method we take $u^0 \equiv 0$. As stopping criterion we choose the relative error $|J(\theta^{k+1}, u^{k+1}) - J(\theta^k, u^k)|/J(\theta^k, u^k)$. In this example, it is fulfilled after 572 iterations when the relative error is smaller than 10^{-4}.

On Figure 4.5 we can see the evaluations of the cost functional during the iterations while on Figure 4.6 we can see how the termination condition of the algorithm is fulfilled. Notice that the sudden jumps in the curves are related to a remesh of the domain for better computation of the temperature and liquid phase fields.

Figure 4.7 shows the simulated temperature in the cutting plane with the location of the coil for two different algorithm iterations. We compare the results from iteration 150 with the

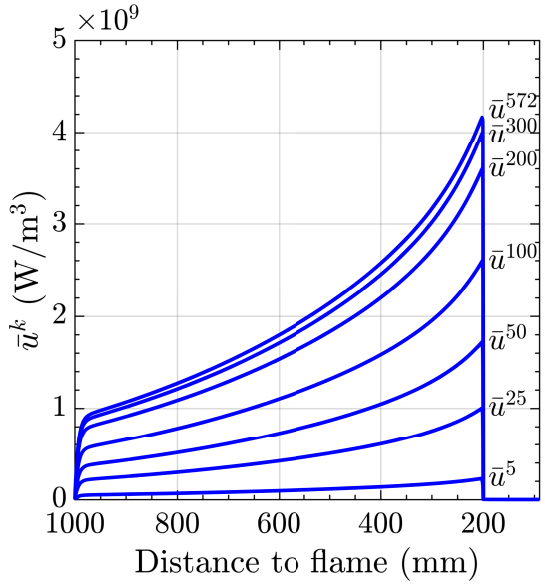

Figure 4.4: Evolution of the restricted control $\bar{u}$ on the top of the cutting plane.

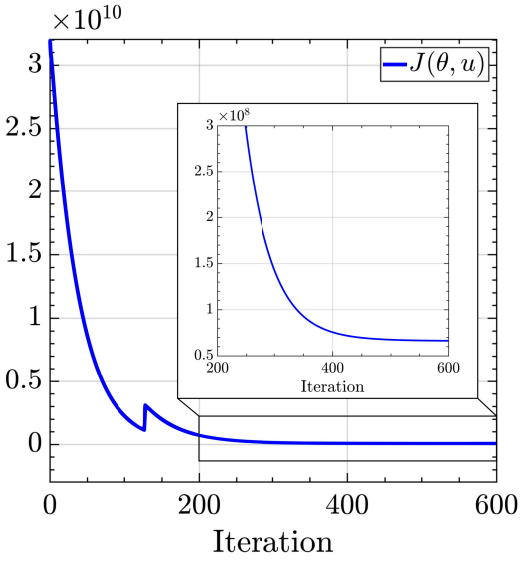

Figure 4.5: Cost functional evaluations.

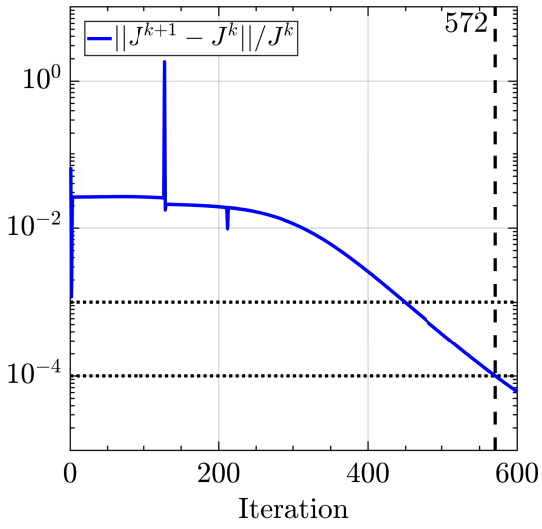

Figure 4.6: Residual during algorithm.

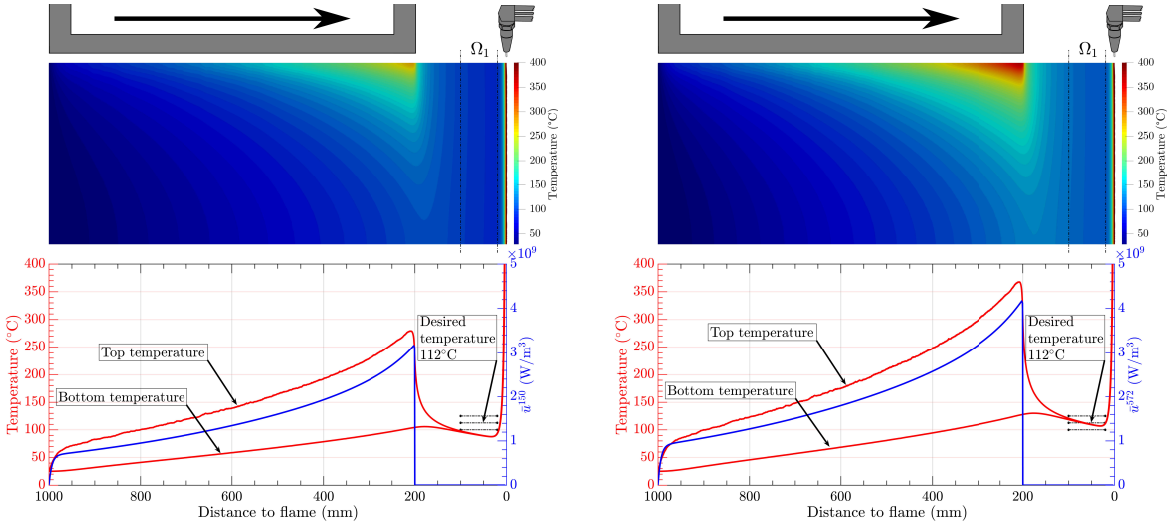

(a) Iteration 150. **(b)** Iteration 572.

Figure 4.7: Top: Temperature field in the cutting plane. Bottom: Top and bottom temperature in the cutting plane together with the optimal restricted control.

results from the optimal control which is reached at iteration 572. In the upper part we can see the temperature field generated by the preheating in the whole width of the plate just before flame cutting. Be aware that in the initial iteration of the algorithm, the control is set to zero, therefore there is no preheating, and the temperature in the whole plate before the flame is the ambient temperature of 25 °C. In the shown cases, it can be seen how the temperature from the top is conducted by diffusion to the bottom and then it reaches certain uniformity. In the bottom graph we focus on the evolution of the temperature on the top and bottom of the plate. The optimal restricted control is also plotted to see the influence in the raise of the temperature. Notice also how after the shutdown of the joule heat due to the end of the coil the top temperature balances with the bottom temperature and then they together reach uniformity in the region Ω_1. In the optimal case (Fig. 4.7b), the temperature in Ω_1 is very close to a constant value of 112.5 °C and within the previously mentioned desired range of 100 to 125 °C.

4.8 Conclusions

The goal of the optimal control problem is to find a preheating source resembling the heat generated by an induction heating coil. From the analytical point of view, the main novelty of this work is that optimality conditions could be derived for the involved nonlinear elliptic system. There are already several articles treating quasilinear systems (see for instance [6], [7], [8], and references therein). In comparison to the previous works, the system at hand deals with a quasilinear elliptic equation for vector-valued functions. But the main difficulty is rather hidden in the lower order terms, since these are non-monotone, which is essentially new up to our knowledge. The non-monotone terms can be handled due to their special structure, which allows to prove a comparison principle for the considered system. This comparison principle adapts the proof in Casas and Tröltzsch [6], which originates from Křížek and Liu [9] to the

considered system. We extend this technique to incorporate the non-monotone lower-order terms, which then allows to derive first order optimality conditions for the system.

The numerical approach allows to obtain a solution to the optimal control problem. When the specified convergence conditions have been fulfilled, the values achieved for the control u (preheating) produce the desired temperature values θ in the area close to the flame Ω_1. The projection factor γ ensures that the optimal preheating profile u can be related to a predefined coil shape. The optimal preheating shows a realistic total energy output, specifically, the total dissipated power by the induction coil in the studied case is 2.7 kW, which is in the range of nowadays induction heating devices. Although, when compared to a standard dissipated power profile obtained with a U-shaped coil from Chapter 3, it is clear that the optimal preheating cannot be achieved in the same way. This is visible in Figure 4.8. The steep increase in power generated by the U-shaped coil is not desirable if the optimal control wants to be achieved. Therefore, the coil portrayed in Figure 4.7 to show the location of the coil cannot itself achieve such power distribution. However, a simple way to possibly decrease the power at the beginning of the coil could be by tilting the coil in such a way that the gap between coil and plate is increased. Another option to find the proper coil by means of an optimal shape control problem will be commented in Chapter 5 along with other possible future work.

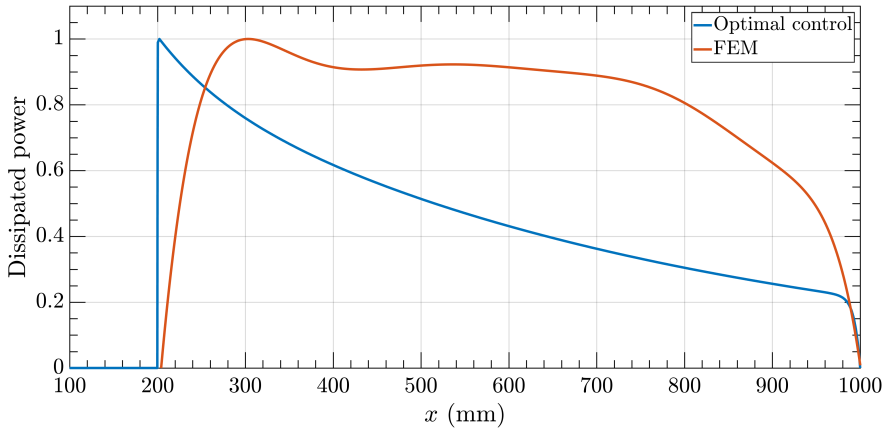

Figure 4.8: Optimal preheating profile comparison with preheating profile from FEM simulations.

5

Conclusion and Outlook

The goal of this work was to study the inductive preheating for thermal cutting of steel plates by means of modelling, simulation and optimal control to solve the problem of cut edge cracking (cold cracks). For this, the process has been divided into different stages.

First, the flame cutting of steel plates was studied separately. It has to be noted that, unlike welding or laser cutting, which are similar physical processes, the modelling literature around flame cutting is quite brief at the time of writing. A 3D-model based on Thiébaud et al. [3] was expanded to consider more phenomenological features. The base model is a 3D quasi-stationary state (QSS) thermal model of the steel plate that takes into account the movement of it. Part of the expansion is that while the base model heat source was tuned to fit experimental data from a single experiment with a chosen cutting speed, the presented model heat source changes with the cutting speed of the process making the model valid for a range of cutting speeds. Another important difference is that solid-solid changes and solid-liquid (melting) in steel are added by novel QSS phase equations. These equations allow, for example, to estimate the kerf (gap created) instead of predefining it like in the base model. Also, it is possible to consider the austenitization of steel happening in the heat affected zone (HAZ) which is the area where cold cracks are more likely to occur. All in all, it is fair to conclude that the model derived covers all essential features of the flame cutting process of steel. For more reliable quantitative predictions a more precise adjustment of phenomenological model parameters based on refined measurements will be necessary.

Secondly, a electromagnetic 3D eddy currents model suitable for a induction preheating setting was examined. It is coupled with a QSS thermal model. The model and setting were put to test by carrying simulations under different cutting parameters while adjusting the electrical current to achieve a maximum temperature. Moreover, experimental testing was done to corroborate the selection of the model. Although the validation was partial, it showed good trend signs and was considered good enough.

The expensive computer simulations for induction heating lead to an alternative to solving the electromagnetic model: the definition of an optimal control problem where the preheating power is the control variable. This was supported by the understanding that many parameters

influence if the preheating objective of uniform temperature just before flame cutting is achieved.

We have investigated the optimal control problem for local preheating of steel plates for flame cutting. The system of PDEs consists of the flame cutting model considered previously with an extra heat source. The system was analysed to prove the existence, uniqueness and regularity of solutions. The goal of the optimal control problem is to find a preheating source resembling the heat generated by an induction heating coil.

The tool developed is able to identify the optimal preheating source that can fulfil the industrial requirement of uniform temperature in thickness of the area that is going to be affected immediately after by flame cutting. The tool is versatile as it can consider a wide range of different settings: type of steel, cutting speed, thickness and desired working temperature.

Furthermore, the projection factor γ defined in (4.40) ensures that the optimal preheating profile can be related to a predefined coil shape. This way, it is easier to study the design of an induction heating device for a particular setting or for a number of them. Although, further research is required to correlate the current intensity and frequency with the optimal control that is obtained with the algorithm. This task seems plausible acknowledging the experience from solving electromagnetic models involving induction at WIAS [41, 5, 52].

All computer simulation were performed with *pdelib2* [10]. It is a FEM package maintained and developed at WIAS whose main data structures are implemented in C++. Mesh refinements were carried out during the simulations with the adaptive mesh module of the mesh generator TetGen [53]. This module is based on a residual-based a posteriori error estimator determining regions with steep gradients for the variables.

The nonlinearities from material properties together with the coupling of equations required a strong computational effort. Thanks to the use of the parallel direct linear solver PARDISO [54–56], the simulations required hours while the optimal control algorithm several days. The optimal control problem was solved numerically applying the projected gradient method [45]. A steepest descent algorithm was implemented in *pdelib2* that allows finding an optimal preheating source that can be identified with an specific induction coil design.

Moreover, the work provides information about the difficulties and stabilization method required to successfully use the QSS phase equations with FEM.

This work covered a preview of the information that can be extracted from simulation and optimal control algorithm results. More in depth, the temperature field allows for further studies, for example, regarding residual stresses or tempering.

The present study has opened questions regarding more control parameters that could be useful in a real industrial case such as distance from coil to flame, coil length or cutting speed. Additionally, further constraints could be included on the maximum temperature that can be reached by preheating, for example, to avoid tempering or even melting.

Open questions remain, as the possible buckling (see Subsection 2.1.1) caused by local preheating instead of uniform, or further restrictions based on industrial guidelines on maximum temperature reached by preheating at some distance from the cutting line.

Following the work done, future research in terms of practical applications leads to the search of an induction coil to provide the optimal preheating found. This could be done by

defining an optimal shape design problem for the induction coil only subject to the Maxwell equations. Work in this direction can be found in [57–59].

From the analytical side, first order optimality necessary conditions were derived for the optimal control problem. In this direction, it could be interesting to derive second order optimality conditions. Second order conditions are often called second order sufficient conditions (SSC). In contrast to the first order necessary conditions, which do not imply that a minimizer has been reached, if additionally the second order conditions are fulfilled, it is certain that the candidate to optimal solution is at least locally optimal.

Moreover, from a more practical point of view, the SSC allow for the implementation of the so-called sequential quadratic programming (SQP) methods (or Newton methods), which have better convergence properties than a simple gradient step algorithm. The gradient step algorithm tends to be rather slow near the optimum.

An introduction to second order optimality conditions for optimal control problems with nonlinear PDEs can be found in [60].

Inductive post-heating was not studied as the time was limited and preheating is thought to be more important. Nevertheless, it could be added as an extra heat source some time after the torch to reduce the cooling of the cutting edge in the remaining plate. This would reduce the cooling rate and diminish the formation of martensite which increases the hardness of the cutting edge. The current optimal control could be extended to design the optimal pre- and post-heating once the cost functional has been updated. Similarly, the optimal control problem for preheating could be modified so the focus is solely on the flame cutting with post-heating. In both cases the model should include the solid-solid phase changes in steel during a cooling process. This way, for example, the martensite fraction can be included in the cost functional to be minimized.

The collaboration with the industrial partner, SSAB, was crucial to achieve a realistic model that they could benefit from. SSAB provided temperature values from experimental data that were used to calibrate the model. Additionally, working together with SSAB helped making the flame cutting model valid for different cutting speeds, which is a feature not found in previous literature. Expanding the knowledge around modelling for flame cutting provides SSAB with more information to improve the ongoing process of thermal cutting. Furthermore, the induction preheating simulation tool may lead to the introduction of an induction heating device to be used in the flame cutting shop in SSAB. It could reduce cost and production time dramatically as it will heat the plates locally just before the cutting instead of the current practice of preheating the plates fully during several minutes.

A

Induction heating coil CELES MP 25/400 data

Table A.1: Technical characteristics of the induction heating coil CELES MP 25/400. (Courtesy of Fives Celes.)

Technical characteristics:	
Type	CELES MP 25/400
Rated output power Pn	25 kW
Minimal output power	1.6 kW
Maximal HF frequency	400 kHz
Minimal HF frequency	100 kHz
Connected power	40 kV A
Supply voltage	3×400 / 480 V (+6/−10 %)
Supply frequency	50 Hz
Phases current	43 A
Power Factor	0.92
Cooling	
Minimum water flow rate	20 L/min
Maximal inlet pressure	7.5 bar
Pressure difference	3.5 bar
Water inlet temperature	25 to 35 °C
Dimensions	
• Width	550 mm
• Depth	600 mm
• Height	804 mm
Weight	∼130 kg
Colour of paintwork	Grey RAL 7035

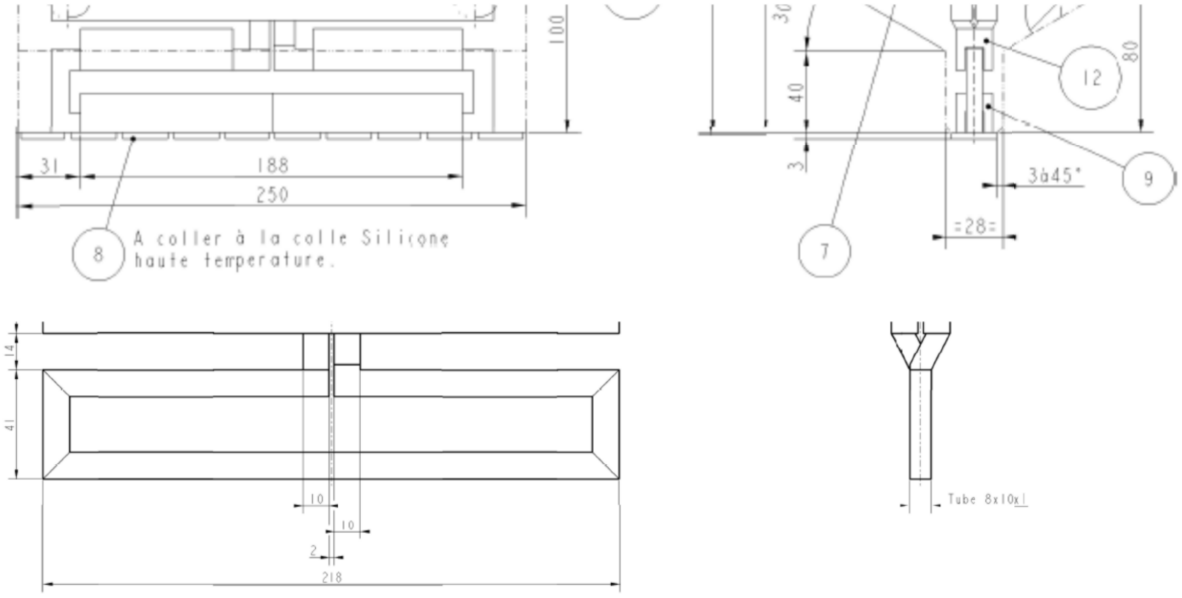

Figure A.1: Technical drawing of the induction heating coil CELES MP 25/400. (Courtesy of Fives Celes.)

Abbreviations

Notation	Description
ABAQUS	Software collection for finite element analysis and computer-aided engineering. 14
B	Boron. 23
C	Carbon. 11
C_{eq}	Carbon equivalent. 11
CO_2	Carbon dioxide. 13
Cr	Chromium. 11
Cu	Copper. 11
DIN	Deutsches Institut für Normung e.V. (German Institute for Standardization). 6
FEM	Finite element method. 23
Fives Celes	Company designing and manufacturing induction heating industrial devices. 46
Fluxtrol, Inc.	Company researching, developing and manufacturing magnetic flux controllers in magnetic flux control for induction heating systems. 40
HAZ	Heat affected zone. 10
ISO	International Organization for Standardization. 6
JMatPro®	Simulation software which calculates material properties for alloys. 23
MATLAB®	Programming language and numerical computing environment developed by MathWorks. 3
Mn	Manganese. 11
Mo	Molybdenum. 11
Ni	Nickel. 11
NorFaST-HT	Nordic community for fast steel heat treatments. 46
ODE	Ordinary differential equation. 20
OFC	Oxy-fuel cutting. 7
P	Phosphorus. 23

Notation	Description
ParaView	Open-source, multi-platform data analysis and visualization application. 3
PARDISO	Parallel sparse direct linear solver. 80
PDE	Partial differential equation. 58
QSS	Quasi-stationary state. 15
Raex®	Abrasion-resistant steels manufactured by SSAB. 12
Ruukki	Rautaruukki Oyj was a Finnish steel company acquired by SSAB in 2014. 11
S	Sulfur. 23
Si	Silicon. 11
SQP	Sequential quadratic programming method. 81
SSAB	Nordic and US-based steel company. 12
SSC	Second order sufficient condition. 81
SUPG	Streamline-Upwind Petrov-Galerkin stabilization method. 24
TC	Thermocouple: electrical device used to measure temperature. 47
V	Vanadium. 11
WIAS	Weierstrass Institute for Applied Analysis and Stochastics. 23

Symbols

Notation	Description
$\mathbf{A}$	Magnetic vector potential [Wb/m].
$\boldsymbol{\mathcal{A}}$	Phasor (or complex amplitude) of $\mathbf{A}$.
a	Volume fraction of austenite phase.
A_s	Austenitization start temperature.
A_f	Austenitization finish temperature.
α_i	Weight in the cost functional.
$\mathbf{B}$	Magnetic flux density [Wb/m^2].
$\boldsymbol{\mathcal{B}}$	Phasor (or complex amplitude) of $\mathbf{B}$.
$\mathcal{C}^{0,1}$	Space of all bounded Lipschitz continuous functions.
$\mathcal{C}^1$	Space of continuous functions whose first derivative is continuous.
$\mathcal{C}^2$	Space of continuous functions whose first and second derivatives are continuous.
C_p	Heat capacity [J/K].
c_i	Parameter for the projection term γ.
$C(v)$	Change of Λ according to speed.
χ_A	Characteristic function of the set A.
$\mathbf{D}$	Electric displacement [C/m^2].
$\boldsymbol{\mathcal{D}}$	Phasor (or complex amplitude) of $\mathbf{D}$.
$\mathrm{d}\,S$	Notation within surface integral.
$\mathrm{d}\,\boldsymbol{x}$	Notation within volume integral.
δ	Parameter in the mixture ansatz for the thermal conductivity κ.
$\mathbf{E}$	Electric field [V/m].
$\boldsymbol{\mathcal{E}}$	Phasor (or complex amplitude) of $\mathbf{E}$.
ϵ	Electrical permittivity [F/m].
ε	Coefficient of artificial diffusivity [m/s^2].
$\boldsymbol{\mathcal{F}}$	Nonlinear function relating the magnetic field intensity and the magnetic flux density.
f	Frequency of the current [Hz].
$\boldsymbol{f}$	Growth function vector of the steel phases.
f_ζ	Growth function of the phase ζ.
γ	Projection factor used on u so it resembles a joule heat distribution from a coil.
Γ_D	Surfaces where Dirichlet boundary conditions are imposed.
Γ_N	Surfaces where Neumann boundary conditions are imposed.

Notation	Description
h	Thickness of steel plate. Usually given in [mm] but used in [m]. Also heat transfer coefficient [W/(m^{2}K)].
$\mathbf{H}$	Magnetic field intensity [A/m].
$\boldsymbol{\mathcal{H}}$	Phasor (or complex amplitude) of $\mathbf{H}$.
H^1	Sobolev space of functions whose weak first derivatives up to order 2 are in L^2, equal to $W^{1,2}$.
$H^1_{\Gamma_D}$	H^1 functions which fulfil a Dirichlet boundary condition in the surface Γ_D.
$H^{-1}_{\Gamma_D}$	Dual space of $H^1_{\Gamma_D}$.
h_i	Heat transfer coefficient [W/(m^{2}K)].
H	Heaviside step function.
I	Current intensity [A].
$\mathbf{J}$	Current density [A/m^2].
$\boldsymbol{\mathcal{J}}$	Phasor (or complex amplitude) of $\mathbf{J}$.
J	Cost functional.
κ	Thermal conductivity [W/(mK)].
L_ζ	Latent heat released/absorbed with the transformation of phase ζ [kJ/kg].
l	Volume fraction of liquid phase/molten steel.
L^2	Lebesgue space of square-integrable functions.
L^p	Lebesgue space of measurable functions whose p-norm is finite.
L^∞	Lebesgue space of essentially bounded measurable functions.
Λ	Subdomain where main heat from flame cutting is located.
meas	Measure function.
m	Gradient step size in the projected gradient method.
μ	Magnetic permeability [H/m].
μ_0	Magnetic permeability of vacuum ($4\pi \cdot 10^{-7}$ H/m).
μ_c	Relative magnetic permeability of concentrator.
$\boldsymbol{n}$	Outward normal unit vector to the corresponding surface.
ν	Auxiliary variable for temperature.
ω	Angular frequency of the current [Hz]. Equal to $2\pi f$.
Ω	Steel plate domain.
Ω_1	Subdomain of Ω where the preheating uniform temperature is desired.
Ω_{air}	Subdomain of Ω_T designating the air.
Ω_{c1}	Subdomain of Ω_T designating the inductor/coil.
Ω_{c2}	Subdomain of Ω_T designating the concentrator.
Ω_c	Subdomain of Ω_T designating the coil-concentrator set.
Ω_T	Domain of the electromagnetic problem including air, steel, inductor and concentrator.
P	Flame cutting heat source power [W].
p	Adjoint variable of the temperature θ in the optimal control problem.

Notation	Description
Q	Flame cutting heat source power density [W/m^3].
q	Sum of all heat sources [W/m^3]. Also, adjoint variable of the phase ζ in the optimal control problem.
$\boldsymbol{q}$	Adjoint variable of the phases $\boldsymbol{\zeta}$ in the optimal control problem.
$\mathbb{R}$	Set of real numbers.
r_i	Radial parameters for the definition of Λ.
$\mathbb{R}^m$	Set of real numbers dimension m.
$R(z, v)$	Radial change of Λ according to height and speed.
$\bar{R}(z)$	Change of Λ according to height.
ρ	Density [kg/m^3].
ρ_V	Charge density [C/m^3].
σ	Electrical conductivity [A/(Vm)].
t	Time [s].
τ_ζ	Time constant for the transformation kinetics of the phase ζ [s].
θ	Temperature [°C].
θ_0	Initial temperature of steel plate.
θ_a	Ambient temperature.
θ_d	Desired temperature for preheating in the optimal control problem.
θ^k	Temperature θ obtained with the k-th value of the control variable in the algorithm to solve the optimal control problem.
u	Control variable in the optimal control problem.
u^k	k-th value of the control variable in the algorithm to solve the optimal control problem.
U_{ad}	Set of all admissible controls.
$\boldsymbol{v}$	Velocity vector for movement of a plate.
v	Moving speed of a plate [m/s].
V	Electric scalar potential [V].
$W^{k,p}$	Sobolev space of functions whose weak derivatives up to order k are in L^p.
$W^{1,p}$	Sobolev space of functions whose weak first derivatives are in L^p.
$W^{1,p}_{\Gamma_D}$	$W^{1,p}$ functions which fulfil a Dirichlet boundary condition in the surface Γ_D.
$W^{-1,p}_{\Gamma_D}$	Dual space of $W^{1,p}_{\Gamma_D}$.
$W^{1,\infty}$	Space of all bounded Lipschitz continuous functions.
x_{max}	Maximum value of the x-coordinate in a domain.
(x_Λ, y_Λ)	Coordinates of the symmetry axis of Λ.
$\boldsymbol{x}$	Cartesian coordinates vector.
(x, y, z)	Cartesian coordinates.
$\boldsymbol{\xi}$	Auxiliary coordinate vector.
y_{max}	Maximum value of the y-coordinate in a domain.
z_i	Height parameters for the definition of Λ.
$\boldsymbol{\zeta}$	Steel phases vector.
ζ_i	A steel solid phase or molten steel fraction.

Notation	Description
ζ_{eq}	Equilibrium volume fraction of phase ζ.
$\partial\Omega$	Boundary of the domain Ω.
$\lvert A\rvert$	Measure of the set A.
$\lvert\mathbf{A}\rvert$	Norm of the vector $\mathbf{A}$.
$[\cdot]_+$	Positive part function.

References

[1] L. E. Lindgren, A. Carlestam, and M. Jonsson, "Computational model of flame-cutting," *Journal of Engineering Materials and Technology*, vol. 115, no. 4, pp. 440–445, Oct. 1993.

[2] T. Jokiaho, A. Laitinen, S. Santa-aho, M. Isakov, P. Peura, T. Saarinen, A. Lehtovaara, and M. Vippola, "Characterization of flame cut heavy steel: Modeling of temperature history and residual stress formation," *Metallurgical and Materials Transactions B*, vol. 48, no. 6, pp. 2891–2901, Sep. 2017.

[3] R. Thiébaud, J.-M. Drezet, and J.-P. Lebet, "Experimental and numerical characterisation of heat flow during flame cutting of thick steel plates," *Journal of Materials Processing Technology*, vol. 214, no. 2, pp. 304–310, Feb. 2014.

[4] M. J. Arenas, D. Hömberg, R. Lasarzik, P. Mikkonen, and T. Petzold, "Modelling and simulation of flame cutting for steel plates with solid phases and melting," *Journal of Mathematics in Industry*, vol. 10, no. 18, Jun. 2020.

[5] D. Hömberg, Q. Liu, J. Montalvo-Urquizo, D. Nadolski, T. Petzold, A. Schmidt, and A. Schulz, "Simulation of multi-frequency-induction-hardening including phase transitions and mechanical effects," *Finite Elements in Analysis and Design*, vol. 121, pp. 86–100, Nov. 2016.

[6] E. Casas and F. Tröltzsch, "First- and second-order optimality conditions for a class of optimal control problems with quasilinear elliptic equations," *SIAM Journal on Control and Optimization*, vol. 48, no. 2, pp. 688–718, 2009.

[7] P. Druet, O. Klein, J. Sprekels, F. Tröltzsch, and I. Yousept, "Optimal control of three-dimensional state-constrained induction heating problems with nonlocal radiation effects," *SIAM Journal on Control and Optimization*, vol. 49, no. 4, pp. 1707–1736, 2011.

[8] E. Casas, "Boundary control problems for quasi-linear elliptic equations: A pontryagin's principle," *Applied Mathematics and Optimization*, vol. 33, no. 3, pp. 265–291, 1996.

[9] M. Křížek and L. Liu, "On the maximum and comparison principles for a steady-state nonlinear heat conduction problem," *ZAMM - Journal of Applied Mathematics and Mechanics / Zeitschrift für Angewandte Mathematik und Mechanik*, vol. 83, no. 8, pp. 559–563, 2003.

[10] Weierstrass Institute (WIAS), "pdelib2." Available: https://www.wias-berlin.de/software/pdelib/." [Accessed on: 2020-09-18]

[11] ISF - Welding and Joining Institute, "Thermal cutting," 2002.

[12] N. R. Mandal, *Ship Construction and Welding*. Springer Singapore, 2017, ch. 11.

[13] E. Oberg, H. Ryffel, F. Jones, and H. Horton, *Machinery's Handbook: A Reference Book for the Mechanical Engineer, Designer, Manufacturing Engineer, Draftsman Toolmaker and Machinist*, ser. Machinery's handbook. Industrial Press, 2004, pp. 1418–1420.

[14] Bug-O Systems, "Flame cutting handbook," 2008. Available: https://bugo.com/wp-content/uploads/bsk-pdf-manager/2019/09/Flame_Ctg_Hndbk_6_08.pdf. [Accessed on: 2020-09-18]

[15] D. L. Olson, T. A. Siewert, S. Liu, and G. R. Edwards, *Welding, Brazing and Soldering.* ASM International, Jan. 1993.

[16] ESAB, "Flame cutting handbook," 2008. Available: https://www.esabna.com/euweb/oxy_handbook/589oxy21_1.htm. [Accessed on: 2020-09-18]

[17] TWI Ltd (The Welding Institute), "Oxyfuel cutting - process and fuel gases," 2000. Available: https://www.twi-global.com/technical-knowledge/job-knowledge/oxyfuel-cutting-process-and-fuel-gases-049. [Accessed on: 2020-09-18]

[18] Ruukki Metals Oy, "Hot-rolled steel plates, sheets and coils thermal cutting and flame straightening," 2011.

[19] TWI Ltd (The Welding Institute), "Carbon equivalent formulae in relation to hydrogen cracking." 2016. Available: https://www.twi-global.com/technical-knowledge/faqs/faq-what-is-the-difference-between-the-various-carbon-equivalent-formulae-used-in-relation-to-hydrogen-cracking. [Accessed on: 2020-09-18]

[20] Ş. Talaş, "The assessment of carbon equivalent formulas in predicting the properties of steel weld metals," *Materials & Design (1980-2015)*, vol. 31, no. 5, pp. 2649–2653, May 2010.

[21] SSAB AB, "RAEX Welding and Thermal Cutting," 2020. Available: https://ssabwebsitecdn.azureedge.net/-/media/files/en/raex/3003-raex-welding-and-thermal-cutting-2020.pdf. [Accessed on: 2020-09-18]

[22] B. R. Hendricks, "Simulation of plasma arc cutting," Master's thesis, Peninsula Technikon, 1999.

[23] K.-Y. Bae, Y.-S. Yang, M.-S. Yi, and C.-W. Park, "Numerical analysis of heat flow in oxy-ethylene flame cutting of steel plate," *Proceedings of the Institution of Mechanical Engineers, Part B: Journal of Engineering Manufacture*, vol. 232, no. 4, pp. 742–751, Jun. 2016.

[24] M. S. Gross, "On gas dynamic effects in the modelling of laser cutting processes," *Applied Mathematical Modelling*, vol. 30, no. 4, pp. 307–318, Apr. 2006.

[25] V. I. Bolobov, "Conditions for ignition of iron and carbon steel in oxygen," *Combustion, Explosion and Shock Waves*, vol. 37, no. 3, pp. 292–296, 2001.

[26] T. Jokiaho, S. Santa-aho, H. Järvinen, M. Honkanen, P. Peura, and M. Vippola, "Effect of microstructural characteristics of thick steel plates on residual stress formation and cracking during flame cutting," *Materials Performance and Characterization*, vol. 7, no. 4, pp. 655–674, Jun. 2018.

[27] J. Duan, H. C. Man, and T. M. Yue, "Modelling the laser fusion cutting process: I. mathematical modelling of the cut kerf geometry for laser fusion cutting of thick metal," *Journal of Physics D: Applied Physics*, vol. 34, no. 14, pp. 2127–2134, Jul. 2001.

[28] W. D. Callister and D. G. Rethwisch, *Fundamentals of materials science and engineering : an integrated approach*, 5th ed. John Wiley & Sons, 2016, pp. 455–473.

[29] D. Hömberg and W. Weiss, "PID control of laser surface hardening of steel," *IEEE Transactions on Control Systems Technology*, vol. 14, no. 5, pp. 896–904, Sep. 2006.

[30] D. Rosenthal, "Mathematical theory of heat distribution during welding and cutting," *Welding journal*, vol. 20, pp. 220–234, 1941.

[31] N. Saunders, U. K. Z. Guo, X. Li, A. P. Miodownik, and J. P. Schillé, "Using JMatPro to model materials properties and behavior," *JOM*, vol. 55, no. 12, pp. 60–65, Dec. 2003.

[32] M. Augustin, A. Caiazzo, A. Fiebach, J. Fuhrmann, V. John, A. Linke, and R. Umla, "An assessment of discretizations for convection-dominated convection–diffusion equations," *Computer Methods in Applied Mechanics and Engineering*, vol. 200, no. 47-48, pp. 3395–3409, Nov. 2011.

[33] T. Petzold, "Modelling, analysis and simulation of multifrequency induction hardening," Doctoral Thesis, Technische Universität Berlin, Fakultät II - Mathematik und Naturwissenschaften, Berlin, 2014.

[34] V. Rudnev, D. Loveless, and R. L. Cook, *Handbook of induction heating*, 2nd ed. Boca Raton, Florida: CRC press, Aug. 2017, ch. 3.1.

[35] A. Bermúdez, D. Gómez, and P. Salgado, *Mathematical Models and Numerical Simulation in Electromagnetism*. Springer International Publishing, 2014.

[36] G. Paoli, O. Biro, and G. Buchgraber, "Complex representation in nonlinear time harmonic eddy current problems," *IEEE Transactions on Magnetics*, vol. 34, no. 5, pp. 2625–2628, 1998.

[37] L. Egan and E. Furlani, "A computer simulation of an induction heating system," *IEEE Transactions on Magnetics*, vol. 27, no. 5, pp. 4343–4354, Sep. 1991.

[38] D. Hömberg, "A mathematical model for induction hardening including mechanical effects," *Nonlinear Analysis: Real World Applications*, vol. 5, no. 1, pp. 55–90, Feb. 2004.

[39] A. Bermúdez, D. Gómez, M. Muñiz, P. Salgado, and R. Vázquez, "Numerical modelling of industrial induction," in *Advances in Induction and Microwave Heating of Mineral and Organic Materials*. IntechOpen, Feb. 2011.

[40] J.-C. Nédélec, "Mixed finite elements in $\mathbb{R}^3$," *Numerische Mathematik*, vol. 35, no. 3, pp. 315–341, Sep 1980.

[41] D. Hömberg, T. Petzold, and E. Rocca, "Analysis and simulations of multifrequency induction hardening," *Nonlinear Analysis: Real World Applications*, vol. 22, pp. 84–97, Apr. 2015.

[42] Fluxtrol, Inc., "Fluxtrol 50 Data Sheet," 2016. Available: https://fluxtrol.com/inc/pdf/Fluxtrol-50-Specs.pdf. [Accessed on: 2020-09-18]

[43] A. Bermúdez, D. Gómez, M. Muñiz, P. Salgado, and R. Vázquez, "Numerical simulation of a thermo-electromagneto-hydrodynamic problem in an induction heating furnace," *Applied Numerical Mathematics*, vol. 59, no. 9, pp. 2082–2104, Sep. 2009.

[44] S. Zurek - Encyclopedia-Magnetica.com, "Effective magnetic permeability." 2020. Available: http://www.encyclopedia-magnetica.com/doku.php/effective_magnetic_permeability. [Accessed on: 2020-09-18]

[45] F. Tröltzsch, *Optimal control of partial differential equations: theory, methods, and applications*. American Mathematical Soc., 2010, vol. 112.

[46] H. Bhadeshia and R. Honeycombe, "Heat treatment of steels: Hardenability," in *Steels: Microstructure and Properties*. Elsevier, 2017, ch. 8, pp. 217–236.

[47] T. Jokiaho, S. Santa-aho, P. Peura, and M. Vippola, "Cracking and failure characteristics of flame cut thick steel plates," *Metallurgical and Materials Transactions A*, vol. 51, no. 4, pp. 1744–1754, Jan. 2020.

[48] J. Nečas, *Les Méthodes Directes En Théorie Des Équations Elliptiques*. Masson, Paris., 1967.

[49] F. Demengel and G. Demengel, *Functional Spaces for the Theory of Elliptic Partial Differential Equations*. London: Springer, 2012.

[50] T. Roubíček, *Nonlinear partial differential equations with applications*. Birkhäuser, Basel, 2005.

[51] R. Haller-Dintelmann, C. Meyer, J. Rehberg, and A. Schiela, "Hölder continuity and optimal control for nonsmooth elliptic problems," *Appl. Math. Optim.*, vol. 60, no. 3, pp. 397–428, Dec 2009.

[52] P. Das, J. I. Asperheim, B. Grande, T. Petzold, and D. Hömberg, "Three-dimensional numerical study of heat-affected zone in induction welding of tubes," *COMPEL - The international journal for computation and mathematics in electrical and electronic engineering*, vol. 39, no. 1, pp. 213–219, Jan. 2020.

[53] H. Si, "TetGen, a delaunay-based quality tetrahedral mesh generator," *ACM Transactions on Mathematical Software*, vol. 41, no. 2, pp. 1–36, Feb. 2015.

[54] A. D. Coninck, B. D. Baets, D. Kourounis, F. Verbosio, O. Schenk, S. Maenhout, and J. Fostier, "Needles: Toward large-scale genomic prediction with marker-by-environment interaction," *Genetics*, vol. 203, no. 1, pp. 543–555, Mar. 2016.

[55] F. Verbosio, A. D. Coninck, D. Kourounis, and O. Schenk, "Enhancing the scalability of selected inversion factorization algorithms in genomic prediction," *Journal of Computational Science*, vol. 22, pp. 99–108, Sep. 2017.

[56] D. Kourounis, A. Fuchs, and O. Schenk, "Toward the next generation of multiperiod optimal power flow solvers," *IEEE Transactions on Power Systems*, vol. 33, no. 4, pp. 4005–4014, Jul. 2018.

[57] D. Hömberg and J. Sokołowski, "Optimal shape design of inductor coils for surface hardening," *SIAM Journal on Control and Optimization*, vol. 42, no. 3, pp. 1087–1117, Jan. 2003.

[58] L. Capone, D. Ivanov, T. Petzold, and D. Hömberg, "A novel integrated tool for parametric geometry generation and simulation for induction hardening of gears," in *Proceedings of Heat Treat 2017*, 2017.

[59] S. Rhein and K. Graichen, "Constrained trajectory planning and actuator design for electromagnetic heating systems," *Control Engineering Practice*, vol. 74, pp. 191–203, May 2018.

[60] E. Casas and F. Tröltzsch, "Second order optimality conditions and their role in PDE control," *Jahresbericht der Deutschen Mathematiker-Vereinigung*, vol. 117, no. 1, pp. 3–44, Dec. 2014.